

**PARALLEL MANIPULATION OF INDIVIDUAL MAGNETIC
MICROBEADS FOR LAB-ON-A-CHIP APPLICATIONS**

A Dissertation
Presented to
The Academic Faculty

by

Zhengchun Peng

In Partial Fulfillment
of the Requirements for the Degree
Doctorate of Philosophy in the
School of Mechanical Engineering

Georgia Institute of Technology
May, 2011

**PARALLEL MANIPULATION OF INDIVIDUAL MAGNETIC
MICROBEADS FOR LAB-ON-A-CHIP APPLICATIONS**

Approved by:

Dr. Peter Hesketh, Advisor
School of Mechanical Engineering
Georgia Institute of Technology

Dr. Mark Allen
School of Electrical Engineering
Georgia Institute of Technology

Dr. Levent Degertekin
School of Mechanical Engineering
Georgia Institute of Technology

Dr. Hang Lu
School of Chemical and Biomolecular
Engineering
Georgia Institute of Technology

Dr. Minami Yoda
School of Mechanical Engineering
Georgia Institute of Technology

Date Approved: Dec. 14, 2010

I dedicate this dissertation to my wife Xiaojing Zu (祖晓静) and my parents Shubi Zhang (张淑碧) and Shuguo Peng (彭书国), who gave me all I needed to complete this work.

ACKNOWLEDGEMENTS

I wish to thank Prof. Peter Hesketh, my Ph.D. thesis advisor, for his guidance and support throughout the course of this dissertation work. I am grateful that he shined his learning to extend my wit and showed his encouragement in my weakness. He inspired my interest in biochemical sensors and magnetic lab-on-a-chip systems. He also gave me the freedom to explore new functionalities and applications of magnetic and electric manipulations of microbeads, which led to a few pieces of creative work in this dissertation.

I give my gratitude to my dissertation committee members, Profs. Levent Degertekin, Minami Yoda, Hang Lu, and Mark Allen, for their scientific input and insightful suggestions on my research and spending time in evaluating this dissertation. I am also grateful to Prof. William Heineman from Chemistry Department at University of Cincinnati for his advice on part of my research.

I thank all my colleagues in Hesketh research group, who friendly helped many aspects of my research. In particular, Surajit Kumar showed me both analytical and experimental skills relevant to my research; Heunjoo Shin, Arnab Choudhury, and Rajesh Luharuka shared with me their microfabrication experiences without reservation. Wei Guo, a very talented undergraduate student from Tsinghua University, China, constructed one of the first prototype devices as a visiting student in our group. His passion and initiatives in experimental research has made a very important piece of contribution to this work.

The staff members including Gary Spinner, Devin Brown, Tran-Vinh Nguyen, and Charlie Suh at the Georgia Tech Nanotechnology Research Center have been very generous in helping me learn how to run all kinds of cleanroom equipment and implement a variety of microfabrication processes for several generations of my devices. Carl Laniak from the machine shop at the School of Mechanical Engineering helped make the magnet fixture for high-speed rotating magnetic field with x-y-z travel control. Vladimir Bortkevich from the ME electronic lab helped construct the multi-waveform modulator capable of alternating high frequency AC signal and DC signal.

I am fortunate to have friends and collaborators like Jack Wei Chen, Wenbin Mao, Lizhi Cao, and Profs. Todd Sulchek, Alex Alexeev, and Tom Barker across the campus of Georgia Tech. My discussions with them on my research generated several new ideas, expanded its original realm, and broadened the possible impact of this work.

Mostly, I wish to thank my dear wife, Xiaojing Zu, without whose love and support this dissertation would never have been accomplished. During the course of this work, I am indebted to her as well as my parents Shubi Zhang and Shuguo Peng a great deal of care, for which I hope to gradually pay back from now on.

Lastly, a portion of the work was funded by CDC/Georgia Tech Bioengineering Seed Program.

TABLE OF CONTENTS

ACKNOWLEDGEMENTS.....	iv
LIST OF TABLES.....	x
LIST OF FIGURES.....	xi
SUMMARY.....	xv
CHAPTER 1	
Research Background and Objectives.....	1
1.1 Research Background.....	1
1.1.1 Introduction to Microfluidic Lab-on-a-Chip.....	1
1.1.2 Introduction to Microbead-based Bioanalysis	6
1.1.3 Introduction to On-chip Manipulation of Microbeads.....	10
1.2 Research Objectives.....	23
1.3 Dissertation Layout.....	26
CHAPTER 2	
Fundamentals of Magnetophoresis and Dielectrophoresis.....	27
2.1 Introduction to Magnetism.....	27
2.2 Materials and Properties of Magnetic Beads.....	29
2.3 Theory on Magnetophoresis.....	34
2.3.1 Magnetic Force	34
2.3.2 Force Balance in Magnetophoresis.....	39
2.3.3 Scaling Law in Magnetophoresis.....	43
2.4 Theory on Dielectrophoresis.....	46
2.4.1 Dielectrophoretic Force	46
2.4.2 Scaling Law in Dielectrophoresis	51

CHAPTER 3

Microfabrication of Soft Magnets and Microfluidic Channels.....	53
3.1 Introduction.....	53
3.2 Microfabrication of Soft Magnets.....	53
3.2.1 Selection of Soft Ferromagnetic Materials	53
3.2.2 Microfabrication of NiFe Patterns Using eBeam Evaporation.....	54
3.2.3 Microfabrication of NiFe Patterns Using Electroplating	57
3.3 Fabrication of Microfluidic Systems.....	61

CHAPTER 4

An Immunoassay Platform Based on Magnetic Assembly of Microbeads between Microelectrode Arrays.....	64
4.1 Introduction.....	64
4.1.1 Immunoassay	64
4.1.2 Interdigitated Array (IDA) Electrodes	66
4.1.3 Magnetic Bead-based Immunoassay with IDA Detection.....	69
4.2 Theoretical Study of Magnetic Assembly of Individual Microbeads	70
4.2.1 Magnetic Field of Rectangular Soft Magnets	70
4.2.2 Magnetic Force for Separating Individual Microbeads from Flow	72
4.3 Fabrication of Integrated MAP-IDA Devices.....	76
4.4 Experimental Results and Discussion.....	82
4.4.1 Magnetic Assembly of MyOne Beads between IDA Electrodes.....	82
4.4.2 Electrochemical Detection of Enzymes Immobilized on Bead Surface	86

CHAPTER 5

A Microfluidic Mixer Based on Parallel, High-speed Circular Motion of Individual Microbeads in a Rotating Magnetic Field.....	93
5.1 Introduction.....	93

5.2	Methods and Materials.....	94
5.3	Theoretical Analysis.....	99
5.3.1	Magnetic Field and Magnetic Force of Cylindrical Soft Magnets	101
5.3.2	Drag Force on a Microbead Moving Close to Substrate.....	106
5.3.3	Maximum Angular Velocity of Microbeads.....	107
5.4	Experimental Setup and Device Preparation.....	110
5.5	Experimental Results.....	113
5.5.1	High-speed Orbital Motion of Individual Microbeads on a Magnetic Chip	113
5.5.2	Mixing of Two Streams of Fluid in a Microchannel	116
5.5.3	Controlling the Number Density of Orbiting Beads on a Magnetic Chip	117
5.6	Discussion.....	118
 CHAPTER 6		
	Transport and Sorting of Magnetic Beads on a Chip in a Rotating Magnetic Field with Time-varying Strength.....	121
6.1	Introduction.....	121
6.2	Working Principles.....	121
6.3	Experimental Setup and Device Fabrication.....	128
6.4	Experimental Results.....	130
6.4.1	Controlled Transport of Microbeads on a Magnetic Chip	131
6.4.2	Size-dependent Sorting of Magnetic Beads on a Chip	135
6.5	Discussion.....	138
 CHAPTER 7		
	Out-of-plane Motion of Microbeads Using Combined Magnetic and Dielectrophoretic Manipulations	141
7.1	Motivations.....	141

7.2	Theoretical Analysis and Device Design.....	143
7.2.1	DEP Force.....	143
7.2.2	MAP Force from Conducting Wires.....	144
7.2.3	Design of Integrated MAP-DEP Devices	145
7.3	Experimental.....	149
7.3.1	Out-of-Plane Oscillation of Microbeads.....	149
7.3.2	High-resolution Tweezing of Microbeads	154
7.4	Discussion.....	158
 CHAPTER 8		
	Conclusions and Recommendations for Future Work.....	161
8.1	Conclusions.....	161
8.2	Recommendations for Future Work.....	167
8.2.1	On-Chip Sorting of Magnetic Beads in Continuous Flow.....	167
8.2.2	Combining Sample Preparation and Detection on the Same Chip	168
8.2.3	Development of Massively Parallel Biomolecular Tweezers.....	169
 APPENDIX A		
	Protocol for Preparing PEGylated Surface.....	172
 APPENDIX B		
	Block Diagram of Multi-Waveform Modulator.....	174
	REFERENCES.....	174

LIST OF TABLES

Table 2.1: Material properties of Dynabeads.....	32
Table 2.2: Magnetophoretic mobility and required field properties under linear magnetization.....	42
Table 2.3: Magnetophoretic mobility and required field properties under magnetic saturation.....	42
Table 3.1: Magnetic properties of common NiFe alloys	54
Table 3.2: Chemical composition of NiFe electroplating bath.....	58

LIST OF FIGURES

Figure 1.1: Microbeads functionalized with a wide variety of biomolecules on surface ..	7
Figure 1.2: Demonstration of moving a group of magnetic particles over a microelectromagnet matrix consisting of two layers of wires	16
Figure 1.3: Illustration of the physical principles of magnetic transport on a magnetic chip with periodic cobalt discs	16
Figure 1.4: Using rotating magnetic field to generate circular motion of magnetic beads inside a microchannel	17
Figure 2.1: The schematic composition of a Dynabead [®] MyOne [™]	31
Figure 2.2: The magnetization curves of Dynabeads a) M280 and b) MyOne measured on highly concentrated suspensions.....	33
Figure 2.3: Forces on a particle in fluid subjected to a non-uniform magnetic field.....	39
Figure 2.4: Illustration of the dielectrophoretic motion of a microparticle	47
Figure 2.5: Real (solid line) and imaginary (dotted line) parts of the Clausius-Mossotti factor as a function of frequency of electric field	50
Figure 3.1: Fabrication procedure for NiFe soft magnets based on eBeam evaporation.	55
Figure 3.2: SEM image of evaporated NiFe magnets (thickness = 0.2 μ m).....	56
Figure 3.3: EDX analysis of the NiFe magnets fabricated by evaporation	57
Figure 3.4: Fabrication procedure for NiFe soft magnets based on electroplating.....	58
Figure 3.5: SEM image of electroplated cylindrical NiFe magnets on Cu seed layer (thickness = 1.2 μ m)	60
Figure 3.6: EDX analysis of the NiFe magnets fabricated by electroplating	60
Figure 3.7: Fabrication procedures for SU-8 masters	61
Figure 3.8: Molding of PDMS microfluidic systems using SU-8 masters	62
Figure 3.9: A ready-to-use magnetic chip assembled with a PDMS channel and coated with PEG on the surface	63
Figure 4.1: An example of electrochemical detection of enzyme labels	66
Figure 4.2: Sketch of interdigitated array electrodes with redox cycling indicated	67

Figure 4.3: Schematic of magnetic bead-based immunoassay using IDAs for enzyme-label detection	70
Figure 4.4: Sketch of a rectangular soft magnet	71
Figure 4.5: Magnetic force (F_z) on a MyOne bead as a function of the distance away from the surface of the soft magnets.....	74
Figure 4.6: Magnetic force (F_z) as a function of the aspect ratio of the soft magnets	75
Figure 4.7: Magnetic force (F_z) as a function of the array density of the soft magnets...	75
Figure 4.8: The fabrication procedure for integrating NiFe magnets with IDAs	76
Figure 4.9: Fabricated devices with integrated NiFe magnets (grey rectangles) among Pt IDA electrodes (shiny bands).....	78
Figure 4.10: Fabrication result of a solid-state Ag/AgCl electrode	80
Figure 4.11: An integrated device on completion of the wafer processes	81
Figure 4.12: Final device in experimental setup.....	82
Figure 4.13: A typical result of magnetic assembly of MyOne beads between the IDA electrodes	83
Figure 4.14: Uniform distribution of microbeads with equal separation distance ($\sim 2.4\mu\text{m}$) along and across the electrodes.....	85
Figure 4.15: Schematic for direct immobilization of enzyme onto the magnetic beads..	87
Figure 4.16: The amperometric responses of a 40-pair IDAs to the injection of the PAPG to 3,000 β -galactosidase modified MyOne beads.....	89
Figure 4.17: The amperometric responses of identical IDAs with different number of beads in presence	91
Figure 5.1: Top-down view of two streams of flow passing through an array of cylinders ($3\mu\text{m}$ diameter) inside a microfluidic channel.....	96
Figure 5.2: Working principle of our magnetic micromixer.....	98
Figure 5.3: Conceptual design of our magnetic micromixer	99
Figure 5.4: Forces on a bead orbiting around a NiFe disc due to a rotating magnetic field	100
Figure 5.5: Sketch of a cylindrical soft magnet	102

Figure 5.6: Magnetic force on a M-280 bead as a function ϕ ($r = 3\mu\text{m}$ and $h = 70\text{nm}$)	104
Figure 5.7: Magnetic force on a M-280 bead as a function r and ϕ ($h=70\text{nm}$)	106
Figure 5.8: Theoretical maximum angular velocity of Dynabeads M-280 as a function of the separation h between the bead and the surface of the magnetic chip	109
Figure 5.9: A magnetic chip designed and fabricated for microfluidic mixing	111
Figure 5.10: Experiment setup for our magnetic micromixer	112
Figure 5.11: Snapshots from a movie, recorded by a CCD camera operated 2000 frames-per-second, of magnetic beads M-280 (black) orbiting around NiFe discs (white) counter clockwise while the external magnet rotated CCW at 9000 rpm	115
Figure 5.12: Top-down view of two streams of fluid in the microchannel	117
Figure 5.13: Snapshots of single M-280 beads (black) circulating around individual NiFe discs (white) in an external rotating magnetic field	118
Figure 6.1: a) Side view of a rare-earth magnet sits above a magnetic chip; b) The bias field of the external magnet across the magnet chip	124
Figure 6.2: A sequence of top-down views of an external magnet (red-blue rectangle) rotating above a NiFe disc (green circle) with an offset between the rotation center of the magnet and the normal of the disc	125
Figure 6.3: Tangential magnetic force on a M-280 bead as a function of ϕ at different bias fields ($r = 2.5\mu\text{m}$, $h = 70\text{nm}$)	128
Figure 6.4: Radial magnetic force on a M-280 bead as a function of r at different bias fields ($\phi = 15^\circ$, $h = 70\text{nm}$)	128
Figure 6.5: Design of a fixture for simultaneous control of the rotation and translation of a permanent magnet	130
Figure 6.6: Simultaneous transport of individual Dynabeads M-280 on a magnetic chip	132
Figure 6.7: Snapshots of two M-280 beads be transported back and forth across the microfluidic channel	133
Figure 6.8: On-chip separation of Dynabeads M-280 from Dynabeads MyOne	137
Figure 7.1: A prototype nDEP-MAP device	145
Figure 7.2: Theoretical magnitude of nDEP and MAP forces on a M-280 bead	147

Figure 7.3: Theoretical prediction of the equilibrium positions of a M-280 bead under different control signals	148
Figure 7.4: Experiment setup for nDEP-MAP manipulations	150
Figure 7.5: a) A picture of the multi-waveform modulator; b) Demonstration of the function of the multi-waveform modulator.....	151
Figure 7.6: Dynabeads M-280 attracted to the conductor by MAP (left).....	153
Figure 7.7: Bead tweezing with a large step, i.e., $\sim 3\mu\text{m}$ levitation from a) to b)	155
Figure 7.8: Image map of a M-280 bead at different height above a surface	156
Figure 7.9: Bead tweezing with a small step, i.e., $\sim 0.6\mu\text{m}$ levitation from a) to b)	157
Figure 7.10: MAP-DEP tweezers for parallel tweezing of antigen-antibody bonds	158

SUMMARY

Many scientists and engineers are turning to lab-on-a-chip systems for faster and cheaper analysis of chemical reactions and biomolecular interactions. A common approach that facilitates the handling of reagents and biomolecules in these systems utilizes micro/nano beads as the solid carrier. Physical manipulation, such as assembly, transport, sorting, and tweezing, of beads on a chip represents an essential step for fully utilizing their potentials in a wide spectrum of bead-based analysis. Previous work demonstrated manipulation of either an ensemble of beads without individual control, or single beads but lacks the capability for parallel operation. Parallel manipulation of individual beads is required to meet the demand for high-throughput and location-specific analysis. In this work, we introduced two methods for parallel manipulation of individual magnetic microbeads, which can serve as effective lab-on-a-chip platforms and/or efficient analytic tools. The first method employs arrays of soft ferromagnetic patterns fabricated inside a microfluidic channel and subjected to an external magnetic field. We demonstrated that the system can be used to assemble individual beads (1-3 μm) from a flow of suspended beads into a regular array on the chip, hence improving the integrated electrochemical detection of biomolecules bound to the bead surface. By rotating the external field, the assembled microbeads can be remotely controlled with synchronized, high-speed circular motion around individual soft magnets on the chip. We employed this manipulation mode for efficient sample mixing in continuous microflow. Furthermore, we discovered a simple but effective way of transporting the microbeads on the chip by varying the strength of the local bias field within a revolution of the external field. In

addition, selective transport of microbeads with different size was realized, providing a platform for effective on-chip sample separation and offering the potential for multiplexing capability.

The second method integrates magnetic and dielectrophoretic manipulations of the same microbeads. The device combines tapered conducting wires and fingered electrodes to generate desirable magnetic and electric fields, respectively. By externally programming the magnetic attraction and dielectrophoretic repulsion forces, out-of-plane oscillation of the microbeads across the channel height was realized. This manipulation mode can facilitate the interaction between the beads with multiple layers of sample fluid inside the channel. We further demonstrated the tweezing of microbeads in liquid with high spatial resolutions, i.e., from submicrometer to nanometer range, by fine-tuning the net force from magnetic attraction and dielectrophoretic repulsion of the beads. The high-resolution control of the out-of-plane motion of the microbeads led to the invention of massively parallel biomolecular tweezers. We believe the maturation of bead-based microtweezers will revolutionize the state-of-art tools currently used for single cell and single molecule studies.

CHAPTER 1

Research Background and Objectives

1.1 Research Background

1.1.1 Introduction to Microfluidic Lab-on-a-Chip

In the field of medical diagnostics, many automated systems have been introduced to enable rapid data collection and efficient analysis from a large number of patient samples that hospitals deal with daily. However, such automated equipment is unsuitable for use in decentralized point-of-care diagnostics and small research laboratories, as they are often too expensive, not portable, and require highly qualified personnel. To improve the global public health, particularly in the developing countries, there is an increasing demand for cheap, fast, accurate, and portable tools that can bring medical diagnostics closer to the patient. There is no doubt that the recent progress in microfluidics technologies will advance the development of such diagnostic tools [1].

Microfluidics is the science and technology of systems that process or manipulate small (10^{-9} to 10^{-18} liters) amounts of fluids, using channels with dimensions of a few micrometers to hundreds of micrometers. Microfluidic systems present the advantage of a small consumption of sample with less waste [2]. For example, a typical microflow of 1mm/sec in a microchannel of 100 μ m wide and 10 μ m tall consumes only 1nL sample per second and 86.4 μ L per day. With continuous flow in such a system for a year, the maximum waste to be produced is only 31mL. In addition to taking advantage of the most obvious characteristic, i.e., small volume, microfluidics also exploits the less obvious characteristics of fluids in microchannels such as short diffusion distances, new

transport mechanisms, and pronounced fluid-structure interactions [1]. Because the time a molecule needs to diffuse from one point to another in fluid is proportional to the square of the distance between the two points, it only takes tens of seconds to overcome 100 μm but several hours to overcome 1 cm for a typical biomolecule with a diffusion constant in the order of $10^{-10} \text{ m}^2/\text{s}$. Therefore, significantly faster analysis can be achieved with microfluidic systems.

Meanwhile, the transport of fluid and reagents inside microchannels poses different challenges than those in macro flows [3]. As the dimensions of fluidic channel decrease, the importance of surface phenomena increases due to large surface-to-volume ratio. Often, interfacial surface effects such as capillary effect, viscous force, and electrostatic force, which are often neglected in macroscale, play more important roles than volumetric effects such as inertial and gravity forces. Therefore, design principles for driving fluid and transporting analyte in microfluidic devices are usually different than those at the macroscale. Although conventional designs for pressure driven flow using micromechanical pumps are still being utilized, many new mechanisms of transporting and handling samples in microfluidic systems have been reported. These new mechanisms include the use of 1) surface tension due to thermal and chemical gradients, and electro-capillarity, 2) electric field for electro-osmosis, electrowetting, and dielectrophoresis, 3) magnetic field for ferrofluid pumping, 4) acoustic streaming, and 5) droplet-based microflow.

More than 30 years ago, the first microfluidic transporting device, an array of ink jet printing nozzles, were developed by IBM researchers in the form of truncated pyramidal holes anisotropically etched in a silicon substrate [4]. At about same time, the

first miniaturized analytical device, a gas chromatographic (GC) analyzer, was fabricated on a silicon wafer [5]. This device integrated an injection valve, a separation column of 1.5 m in length, and a thermal conductivity detector, which was able to separate a simple mixture of gas compounds in a few seconds. Despite its rapid separation capabilities, the interest of the scientific community in this device was low, presumably due to the lack of technological experience to deal with the device of that minute size. It was not until 1990 when Manz et al. first fabricated the high-pressure liquid chromatography (HPLC) column device using silicon–Pyrex technology [6] and introduced the concept of micro total analysis system or μ TAS [7] that the interest in microfluidic systems started to boost. A μ TAS incorporates all analytical procedures including sample pretreatment and molecular analysis into a microfluidic system with integrated sensors. Several μ TAS prototype devices [8][9] at the time demonstrated that integration of pre-treatment steps, usually done at lab-scale, could extend the simple sensor functionality towards a complete laboratory analysis including sample separation and cleaning steps. Commercial interest also surfaced in the mid 1990's, when μ TAS technologies turned out to offer capable tools for genomics applications such as micro capillary electrophoresis [10] and DNA microarrays [11]. An important effort in research support also came from the military during that period of time, especially from Defense Advanced Research Projects Agency (DARPA) of the U.S. Department of Defence (DOD), for their interest in portable bio/chemical warfare agent detection systems. Hence the added value of μ TAS not only was coming from integration of lab processes for analysis, but also included the characterization of individual bio/chemical components and the application to other, non-analysis, lab processes. Hence the term "lab-on-a-chip" was introduced.

The concept of lab-on-a-chip was first proposed in 1995 by Ramsey et al. [12], who borrowed the same technologies used in the microelectronics industry to build miniature biological and chemical processing and analysis systems. Just as the field of microelectromechanical systems (MEMS) uses microelectronics manufacturing technologies to create microscale functional mechanical devices such as motors, gears, and accelerometers on a chip, scientists are now using the same technologies to make the equivalent of pipettes, incubators, reaction chambers, and analytical instruments on a chip for biochemical and clinical analysis. There is ample justification for such a vision. For example, mixing biochemical samples such as chemicals and proteins in hundreds or thousands of conventional tubes for drug discovery can take months. Even with robots in the process, the reaction between a large numbers of molecules can take very long time to complete. Replacing the tubes with microfluidic channels on a chip with integrated pipetting or valving, mixing, and reaction monitoring functions can process biochemical samples much faster, due to much smaller volume of sample (e.g., thousands of times smaller than a dewdrop) to be mixed for specific reaction [13].

Lab-on-a-chip is a vision that predicts microfluidics will do for biotechnology what the transistor did for microelectronics. In the same way that the computer chip has automated and accelerated mathematics, lab-on-a-chip aims to automate and accelerate biology and chemistry. Researchers envisioned that the key to its success is through large scale integration of microfluidics, similar to the success of integrated circuits (IC) industry in microelectronics [14]. Therefore, just like ICs provide validated elements and processes to make electronic circuitries, a set of validated microfluidic units are necessary in a microfluidic platform. The basic units should be able to operate

functions such as transport, valving, metering, mixing, and separation or concentration of molecules or particles in fluid. These fluidic units have to be able to perform the application-specific operations, because the collection of fluidic units needed for diagnostic applications may have only little overlap with the collection needed for pharmaceutical applications. In some cases detection methods will also belong to the basic set of micro-fluidic operations, and in other cases not [15]. Nevertheless, in all cases the user has to be able to readily combine any unit within a given microfluidic platform in order to operate an assay for diagnostics [16] or to screen for new compounds in drug development [17].

Other than miniaturization and integration, lab-on-a-chip has the advantage in parallel operation for high-throughput analysis. High-throughput bioanalysis can be obtained either by the parallel screening of multiple samples for one target, or by the screening of one sample for multiple targets simultaneously, or by a combination of both multiplexing techniques (see review by Situma et al. [18]). In microfluidic lab-on-a-chip, both parallel screening of a number of samples in a number of channels in one device [19] and simultaneous detection of multiple targets in a sample present in one channel [20] have been demonstrated. Two different strategies, referred to as “planar arrays” (also called microarrays [11]) and “suspension arrays” (also called particle-based arrays [21]), have been developed for multiplexing purposes. Multiplexing employs a variety of encoding schemes for molecular identification that can be classified as optical, electric, and magnetic. The code allows specific analyte that reacts with the capture probe bound at a particular location in the array to be identified. Whereas planar microarrays strictly rely on positional encoding, particle-based arrays offer a more flexible choice of probes,

i.e., the detection of additional targets only requires adding particles bearing new probes to the sample, while a new microarray has to be made in the case of planar arrays. Furthermore, by controlling the concentration of microparticles it is also straightforward to change the total number of probe molecules in the assay, while the total active surface in a flat microarray is constant. In the discussion to follow, we focus on the microparticle-based analysis.

1.1.2 Introduction to Microbead-based Bioanalysis

Surface-based assays, also referred to as heterogeneous assays, such as performed in chromatography and cytometry, offer the advantage of easy separation of chemical complexes from reactants because the reactions occur both in solution and in a solid substrate. Due to the reduced diffusion distance of analyte and large surface-to-volume ratio, microfluidic devices have been used for surface-based biochemical assays, in which the microchannel walls were chemically activated and covalently linked with biospecific molecules [22][23]. However, examples of microchannel surface-based platform for heterogeneous analysis are still rare. This is mainly because of the challenges involved in reproducibly and effectively modifying the microchannel surfaces due to the delicate and lengthy chip preparation prior to the assay [24]. Alternatively, micro/nano particle-based platforms are a viable approach to surface-based assay. Microbeads and nanoparticles can easily be pre-grafted with biospecific molecules and can be introduced inside a microfluidic channel to offer biochemically active surface in a bioassay. In addition, this surface can be made mobile in liquid by external manipulation using the properties of the bead material, which leads to acceleration of the interaction between bound functional groups with surrounding fluids beyond the diffusion limited interaction.

Among all types of existing micro and nanoparticles, polymer and silica beads have been the most popular for surface-based bioanalysis. This is because biochemical molecules can be easily grafted onto the surface of these materials. An excellent review by Kawaguchi describes the methods for manufacturing the polymer microbeads, and discusses some important applications in which the bead surfaces have been adopted as biomolecular analysis platforms [25]. Many companies offer polymer and silica microbeads with the desired biomolecules already immobilized for a wide variety of applications such as immunoassay, DNA hybridization, even biochemical synthesis (figure 1.1). These specifically functionalized beads, ranging from tens of nanometers to tens of micrometers, may be used either in dilute suspension, colloidal solution, or packed beds depending on the application.

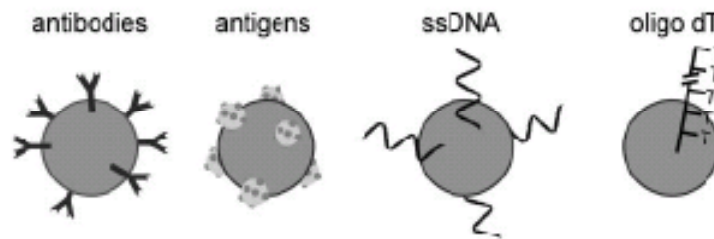


Figure 1.1: Microbeads functionalized with a wide variety of biomolecules on surface
This figure is adapted from [26].

Because of the wide range of beads available as the biomolecular carriers and analysis platforms, and the advantages that microfluidics have to offer, the combination of the two technologies for lab-on-a-chip applications have seen increased activity in the last decade. The particularly attractive and powerful traits of microbead-based assays in microfluidic devices are summarized below:

First, the use of colloidal or packed beads as molecular carriers increases the biochemical binding capacity per unit volume. For example, 1 gram of beads having a

diameter of $1\mu\text{m}$ has a total surface area of about 0.6 m^2 . Therefore, using the surface of the beads as the platform for biochemical reactions makes it possible to carry out the reactions in extremely small volumes, leading to further miniaturization of necessary microfluidic system. In addition, the high-density specific reagents immobilized on bead surfaces can lead to faster and stronger reaction than for the same amount of reagents on flat surface of microtiterplates [27] or in a large volume solution [28].

Second, when bead suspensions rather than packed beds are used as the mobile carrier of reagent inside the microfluidic channels, the transport capability of the devices is improved, because the transport of the reagent to the reaction site can be realized and controlled using the properties of the beads other than the properties of the reagent. For example, they can be moved through solution using gravity, acoustic wave, and electric fields. Hence bead-based assay can reduce the analysis time further on top of the already reduced time for mass transport in microfluidic systems [3]. It also gives location specificity for the reagent and biochemical reaction inside a microfluidic channel. In addition, the mobility of microbeads inside a microchannel can be used for sample mixing purposes. The Reynolds number of fluid flows in microfluidic devices is small (usually much less than 1), hence the flow profile is laminar and that molecular transport only occurs by diffusion, which is relatively time-consuming despite the rather small dimensions involved in the assay. This challenge can be overcome by continuously move microbeads around to cause local secondary flow in the sample [29]. Even in the absence of those field effects, micro/nano beads are not completely stationary due to Brownian motion. Hence, solution is continually being refreshed at the bead surface, leading improved binding kinetics and thermodynamics compared to stationary channel wall-

based assays. With the “near-solution” kinetics, the interaction between a molecule bound to the surface of a bead and a free molecule better simulates those between two free molecules.

Third, encoded microbeads allow for multiplexing in a “suspension array” inside a microfluidic channel [30]. Multiplexing is extremely important in situations where the amount of sample is very limited, such as in the analysis of blood from newborns, tumor tissue from biopsies, etc. The combination of microfluidic technology with encoding technology of microcarriers offers a powerful lab-on-a-chip platform due to the remarkable characteristics of both technologies, which complete each other [31]. For example, the integration of magnetic microbead arrays inside microchannel has demonstrated sample separation with selective detection in extremely small volumes [32][33]. In addition, because the different targets are screened simultaneously, they experience equal conditions at each step of the assay procedure, leading to good quality control in batch synthesis [30]. Advancement in “suspension array” has been demonstrated with isolation, sorting, and manipulation of differently encoded beads [34][35], and with the implementation of optical and electronic detection instruments in close proximity to the microchannels carrying the multiplexed microbead arrays. Promising examples in this research area are the micro flow cytometers [36], microscope reading systems [37], integrated light-emitting diodes and detectors [38], and so on.

Because of the aforementioned synergism, bead-based microfluidic systems offers fundamentally new capabilities in the control of molecules in space and time [1], which is expected to significantly benefit the medical diagnostics, high throughput screening, and combinatorial chemistry fields [24].

1.1.3 Introduction to On-chip Manipulation of Microbeads

A microbead-based lab-on-a-chip device often requires some forms of bead manipulation within the device. This requirement is dictated by the ultimate goal of any lab-on-a-chip platform, i.e., carrying out sample preparation (such as mixing, separation, and concentration), reaction, detection, etc., on the chip. Hence, basic manipulation modes such as retaining the beads inside the microchannel, localizing them in a designated point, transporting them across the channel, as well as sorting and counting them on-chip are necessary. A number of methods to fulfill these manipulation modes have been reported in literature. Some use physical barriers, or surface adsorption means, others rely on the use of optical, electrical, acoustical, or magnetic fields, which have the advantage of remote control through the use of lasers, electrodes, sonic waves, or external magnets, respectively.

Each method has its advantages and disadvantages. Optical manipulation technique uses a laser beam to impose scattering force upon microparticles that counterbalances the gravitational force and effectively pins the particles into an optical trap [39]. This technique present an effective method for three dimensional control of particles [40], but it can only exert tens of picoNewtons of force on particles [41], which bars this technique from many force measurement platforms. In addition, for many materials lasers often induce charging or heating, which adversely affect system performance. Electrical manipulation techniques represent one alternative for manipulating suspended particles, which have the advantage of providing larger forces in the range of nanoNewtons on microparticles that allows access to many interesting measurement and assembly techniques [42]. Additionally, electrical techniques work for large range of materials from dielectrics to conductor. However, electric platforms can

have deleterious effects such as charging and heating, much like the optical manipulation techniques [43]. Magnetic manipulation techniques satisfy the requirements to high forces and reduced charging and heating of samples. Furthermore, magnetism has the inherent advantage of being chemically and biologically invisible [44]. However, the primary drawback, sometimes overlooked for its blatancy, is the requirement for magnetic materials within the system. Though many applications require the manipulation of magnetic materials, there are significantly more applications requiring manipulation of nonmagnetic particles.

Using acoustic waves to localize particles to different regions on a surface is a relatively new development in particle manipulation. This technique takes advantage of difference in density and stiffness between the particle and the surrounding fluid [45]. Acoustical systems allow for the generation of multiple pressure nodes in a system without the need for local structures to create distortions to the field, a requirement in common optical, electrical, and magnetic systems. These localized pressure nodes can be created using ultrasound sources and signals. Although this technique has developed into bulk fluid applications of spatial patterning of aggregates [46], cells [47], and sized-based separation schemes [48], the pressure nodes tend to be broad, weak, and exhibit higher order frequencies, hence do not provide for precise, deterministic control of many useful microparticle sizes.

In the sections to follow, the manipulation techniques using electric and magnetic fields for lab-on-a-chip applications are summarized. Detailed discussion on other manipulation methods are omitted due to the relevance to the scope of this dissertation.

1.1.3.1 Overview of magnetic manipulation of microbeads

The magnetic response of magnetic colloidal suspensions has been studied for decades. These magnetic particles interact with the field in a variety of ways including attraction, alignment, and chaining. In these systems, there are many control parameters affecting the magnetic response, from particle size to volume fraction, which has allowed for a variety of applications from mechanical bearings and dampers [49] to human prosthetics [50], and audio speakers [51]. In this overview, we focus on the manipulation and applications of magnetic particles that are in the micrometer range, excluding the manipulation of magnetic nanoparticles or ferrofluid and their applications.

In the biomedical industry, the most common use of magnetic microbeads is in the field of separation, where magnetic manipulations are applied to capture and separate various biological and chemical targets of interest including cells [52], biomolecules [53][54], and drug molecules [55]. For magnetic separation applications, magnetic bead surfaces are typically functionalized with proteins and receptors that can recognize and associate with the target materials by affinity binding. Once attached, they can be magnetically separated from the solution, flexibly manipulated in various reagents, and easily transported to a desired location. The manipulation is often remotely controlled by magnetic fields produced from a permanent magnet or electromagnet. Compared with many other separation techniques such as centrifugal separation [56] and electrophoresis-based manipulation [57], magnetic means has the important attributes of being highly selective and independent of normal chemical and biological processes, because the vast majority of biochemical materials do not respond to magnetic fields.

When functionalizing the surface for bead-based separation and analysis, polymer beads are preferred and are, however, non-magnetic. In 1976, the Norwegian professor John Ugelstad first succeeded in making spherical polystyrene beads of exactly the same size in a few micrometers – only previously achieved by NASA in the weightless conditions of outer space. Later the uniform microbeads were made magnetizable through doping nanometer-size hematite (Fe_2O_3) or magnetite (Fe_3O_4). This amazing achievement led to the invention of magnetic bead-based bioseparation, or biomagnetic separation technology, in which the polymer surface of the beads is utilized for biological interaction site, while the magnetic components inside the beads are used for magnetic manipulation. Biomagnetic separation technology has since then evolved into commercial separation tools such as separation of proteins and peptides with Dynabeads® in liquid chromatography columns offered by Invitrogen Corp. (<http://www.invitrogen.com/site/us/en/home/brands/Dynal/.html>) and cell separation with magnetically activated cell sorting (MACS®) columns available from Miltenyi Biotec GmbH (<http://www.miltenyibiotec.com>).

Because of the successful development and commercialization of biomagnetic separation using permanent magnets in conventional analytical tools, it is not surprising that external magnets have also been used to manipulate magnetic beads within microchannels. Nearly all important functions in a bioassay have been realized using magnetic beads on-chip, which include sample separation/ purification, transport, mixing, labeling, and detection, we will discuss some of these functions in the sections to follow.

Several reports demonstrated that an external magnet could retain magnetic beads in a microfluidic channel and facilitated the separation of target molecules such as

antigens and DNA onto the bead surface and dramatically enhanced the interaction between free reagents and those immobilized on the bead surface [58][59][60]. Magnetic field flow fractionation (FFF), in which the separated beads and bound molecules are continuously moving and inducted into designated downstream channels or outlets, was also demonstrated [61][62][63]. FFF, invented by J. Calvin Giddings [64], is a separation technique where a field is applied to a mixture perpendicular to the mixture's flow in order to cause separation due to differing mobilities of the various components in the field. The major advantage of the FFF technique lies in its high throughput without any discrete flushing procedures and complications in automation.

Localization of magnetic beads to specific points and manipulating them with high spatial resolutions on-chip require the integration or coupling of a transducer for magnetic field generation inside the microchannel. Both microfabricated electromagnets [65][66] and soft magnetic features subjected to an external magnet [67][68] have been used to generate magnetic fields inside microchannels for this purpose. Recent advances in microfabrication have allowed for production of magnetic elements that can produce field gradients exceeding 10^5 Tesla per meter. Through the use of arrays of conductors with external control, magnetic field and field gradient on the chip can be externally controlled by current configuration to form application-specific patterns. As a result, these magnetic elements are useful not only for magnetic confinement, but also in moving the beads around on a surface. For example, controlled transport of an ensemble of magnetic beads using conductor coils [69][70] and current-carrying wire networks [71] were demonstrated (figure 1.2).

Rotating magnetic field is extremely useful for magnetic transport on a chip. By combining an external rotating magnet with appropriate design of the soft magnetic patterns on a chip, several research groups have demonstrated controlled transport of individual magnetic beads across the soft magnetic features in an array [72][73][74]. An example of this research field is shown in figure 1.3. Furthermore, circular motion of magnetic beads on a chip were also demonstrated with a clever design of rotating electromagnetic field [75][76]. As shown in figure 1.4, this type of magnetic systems can be used to facilitate sample mixing inside a microchannel.

Transport of single magnetic beads on a surface was also realized by using specially arranged tapered conductors [77]. In addition, domain wall tips [78] and magnetic force microscopy tips in combination with soft magnetic patterns on a membrane [79] were utilized to handle single magnetic beads on a chip. One important application for single bead manipulation is biomolecular tweezing. Many biomolecular tweezers have been developed, among which optical tweezers [80] and AFM [81] are dominantly used in research labs. The biggest problem associated with the current tweezing tools is they are very inefficient in generating experiment data with statistical significance and high reliability. In contrast, the microbead-based tweezing of biomolecules can be easily configured for parallel operation, leading to large data generation in a single experiment for high throughput analysis. Due to the advantage of the magnetic force in biocompatibility and specificity, the application of lateral and torsional forces to biomolecules by tethered magnetic beads has been an essential method for revealing information about molecular motors, protein-DNA interactions, and the forces associated with folding and unfolding dynamics of proteins and DNA [82][83].

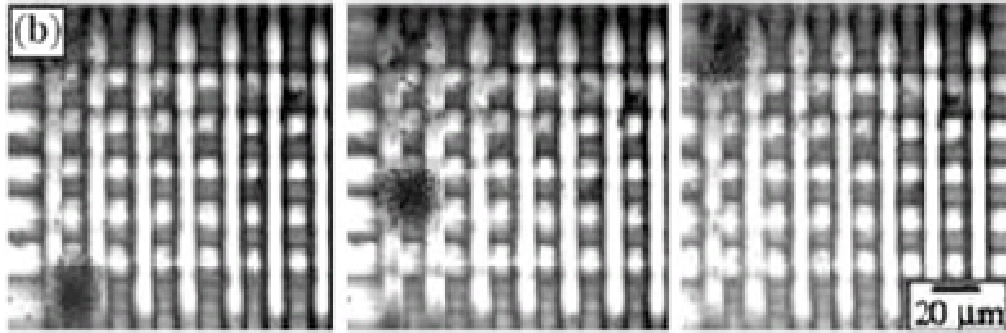


Figure 1.2: Demonstration of moving a group of magnetic particles over a microelectromagnet matrix consisting of two layers of wires
The wire currents were adjusted so they continuously move a group of particles over a range of five wire spacing in the matrix. This figure is adapted from [71].

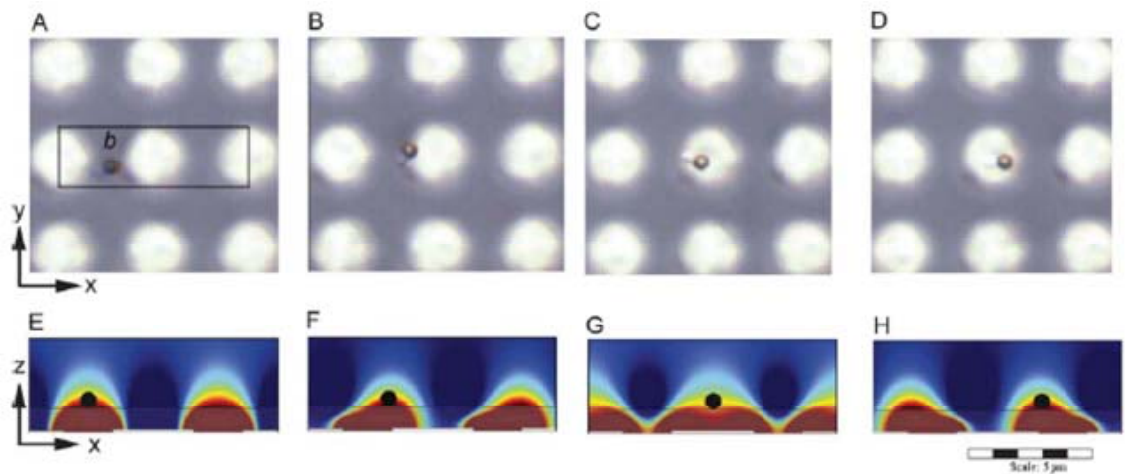


Figure 1.3: Illustration of the physical principles of magnetic transport on a magnetic chip with periodic cobalt discs

Top row: top-down view (x - y plane) of the magnetic chip in which a $1\mu\text{m}$ superparamagnetic bead (dark) is transported above the $5\mu\text{m}$ cobalt disks (white). The bead moves from left to right across the center of the soft magnet as a rotating 60 Oe external magnetic field is generated with electromagnets with orientation of A) $\theta = 180^\circ$, B) 270° , C) 0° , and D) 90° in the x - z plane.

Bottom row: side view (x - z plane) profile of the magnetic field generated at the surface of the three cobalt magnets delineated with the rectangle in A), as the external field is rotated. The position of the field maximum is indicated with a block dot. This figure is adapted from [72].

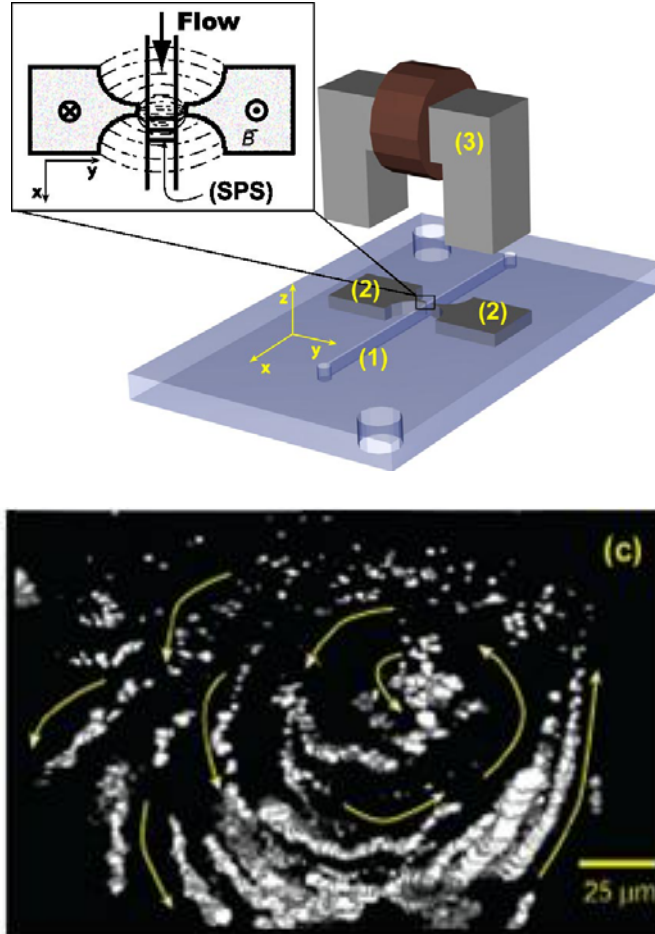


Figure 1.4: Using rotating magnetic field to generate circular motion of magnetic beads inside a microchannel

(Top) Schematic view of the experimental setup: (1) microfluidic channel realized by glass micromachining and bonding of PMMA sheets; (2) embedded soft magnetic parts for magnetic field focusing; (3) electromagnet, consisting of a soft magnetic U-core and a coil. The insert shows a schematic view of the magnetic field distribution between the soft magnetic parts. This figure is adapted from [75].

(Bottom) Fluorescent microscopy of a $2.1\mu\text{m}$ superparamagnetic bead solution at the mixing region, showing the superposition of 30 video frames taken at 60ms time intervals. The trajectories of the fluorescent beads form a vortex rotating along the sense indicated by the arrows. This figure is adapted from [76].

As the development of a large pool of on-chip magnetic handling techniques continues, magnetic beads are finding unprecedented opportunities for lab-on-a-chip applications [84][85]. However, previous work on magnetic manipulation was

demonstrated with either an ensemble of microbeads, or on single beads but without parallel manipulation. The first scenario is due to the relatively large size of the magnetic manipulation elements compared to that of beads. The second scenario is mainly due to the physical limitations of the tools currently available, e.g., magnetic force microscope, which do not provide parallel operations. In many cases, parallel manipulation of individual beads is required to meet the demand for high throughput analysis and identify location specificity and other information that are obscured in ensemble manipulation and statistical distribution. The most conspicuous need for parallel analysis lies in domains such as genetic sequencing [86], drug screening [87], diagnostics and monitoring of public health [88]. These areas require massive numbers of manipulations of the sample, and higher sensitivity and resolution than had previously been contemplated in biology. For instance, there is widespread agreement in the genome community that the complexity and diversity in mammalian genomes call for a processing capability that are hundreds and thousands times the power of current technological tools [89][87]. In drug development, new approaches of combinatorial chemistry are capable of producing millions of new compounds in a short time. However, analyzing each compound with respect to multiple biochemical parameters is slow [17][90]. In clinical settings, the strategy of multiplexing many analytes at the point of care is a key component to disease diagnostics and control. Yet the diagnostic and monitoring products to date have been limited to a few analytes [91][92].

1.1.3.2 Overview of dielectrophoretic manipulation of microparticles

Dielectric particles, such as the polymer and silica microbeads discussed before, can be manipulated by non-uniform electric fields. Because of electric polarization,

electric charge separation occurs within the dielectric particle as well as in the liquid side of the solid–liquid interface, resulting in an electric dipole moment. The interaction between the dipole and the non-uniform field gives rise to a net force on the dipole. The induced motion of a dielectric particle in a non-uniform electric field is referred to as dielectrophoresis (DEP) [93]. To minimize Joule heating and possible electrolysis of the medium under relatively high electrical potentials, AC fields are often used for DEP.

The DEP force can be attractive or repulsive depending on the permittivity and conductivity of both the particle and the fluid medium, and the frequency of the applied field [94]. The attractive and repulsive DEP forces are known as positive DEP (pDEP) and negative DEP (nDEP), both of which can be used for particle manipulation purposes. Another major advantage of DEP compared to other manipulation schemes is the variability in the frequency response, which gives rise to an important control parameter for particle manipulation. This additional degree of control may be selective enough for DEP microsystems to differentiate between similar particle types [95]. In addition, DEP manipulation does not require special material properties of the target particles such as the needed magnetic properties for magnetic manipulation.

Dielectrophoretic trapping and separation of dielectric particles and even biological cells using their intrinsic dielectric affinity have been made possible by the integration of microelectrodes into microfluidic devices as early as 1960s. Among many demonstrations of this technology in literature, a notable example is that of Beker et al. [96], who reported a DEP separation system with interdigitated, castellated micro-electrode arrays for non-uniform electric field generation. Using appropriate driving frequencies, positive and negative DEP forces are acted on different groups of cells. Cells

experiencing pDEP are collected and held in deep and steep-sided potential energy wells at the electrode edges, whereas cells experiencing nDEP are repelled and collected as aggregations in shallow potential energy wells in the void space between adjacent electrodes. There are a great variety of means of constructing DEP electrode layout for trapping and separating particles on a chip for subsequent manipulation and analysis. Other than the classical constellated electrodes, slim interdigitated electrodes, quadruple electrodes, 3D post electrode arrays, and other interesting designs were demonstrated. Alternative approaches were reported to generate DEP force by combining active and electrically floating electrodes [97][98]. Meanwhile, insulating materials, such as glass and polymers, instead of using metallic electrodes were used to construct DEP traps [99][100][101]. This insulator-based DEP technique is less prone to fouling, thus the devices generally retain their function despite surface changes, and avoids gas evolution due to the lack of metallic electrodes, which usually cause electrochemical reactions.

DEP-based field flow fractionation (FFF) has been realized on a chip with several variations. In addition to 2D layout of electrode arrays such as global electrodes with different shapes fabricated on the bottom of the microchannel [102][103], 3D layout of electrode arrays on both top and bottom sides, or the sidewalls, of the channel have been used as deflector structures to continuously separate microparticles in vertical and transverse directions[104][105][106]. Worthy of mention is the work by Li et al. [107], who employed electrode array structures biased by a resistive ladder network to control individual electrodes in creating non-uniform ‘isomotive’ fields, with which positive and negative DEP particles were pushed into different region and separated continuously. DEP-FFF of submicron particles and viruses were also realized [108]. Unlike the larger

microparticles such as cells, sub-micrometer particles are strongly influenced by thermal effects such as Brownian motion. However, DEP force of sufficient magnitude can overcome the diffusion barrier and realize the on-chip FFF of even DNA macromolecules [109].

On-chip transport of dielectric microparticles and cells was realized with travelling wave DEP (twDEP). A dipole moment is induced across the particle in the presence of a traveling field. In normal situation, the induced dipole in the particle aligns with the peak of the travelling field. However, if the field moves sufficiently fast, the time taken for the dipole to form (relaxation time of the dipole) becomes significant and therefore the dipole may lag behind the peak of the field. The separation between the dipole and the field peak will induce net force acting on the particle, resulting in a translational motion of the particle. From late 1980s, several groups from Europe have conducted both theoretical and experimental investigations on twDEP. Subsequent works by more researchers in recent years have been focused on developing more complex twDEP systems and applications. For example, a hybrid method combining conventional AC-DEP and twDEP to transport and separate microparticles across a microchannel was demonstrated [110]. This technique forms a dynamic electric field by sequentially energizing an array of electrodes. The transportation is controlled by the electrode activation time and separation achieved by controlling the applied electric frequency. At appropriate frequency, particles experiencing negative DEP travel in front of the moving electric field, while particles experiencing positive DEP lag behind the moving field, which results in separation of a mixture of particles with different dielectrophoretic affinity.

Other than the batch manipulations described previously, trapping single microparticles or cells and positioning them to specific locations on a chip has also been demonstrated. Various designs of DEP electrodes can be easily scaled down to confine a single microparticle or cell in a specific DEP cage. For example, grid electrode system [111][112], electrode rings [113], scattered square electrodes [114], and quadruple electrodes [115][116] have been reported. Single particle or cell manipulation has the advantage in managing the position and microenvironment with parallel manipulations of the individual particles or cells. Because DEP forces are sensitive to the change of the intracellular properties and extracellular interaction, DEP manipulation provides an excellent platform for the single-cell assay and may reveal complex cellular processes which cannot be achieved by manipulating mass cell population [117].

DEP manipulation can be easily employed in combination with other manipulation methods that may concurrently exist in the DEP microsystem to produce many sophisticated manipulations of microparticles. For example, on-chip sample mixing has been demonstrated by using DEP along with electrohydrodynamic phenomena [87], electrorotation [118], as well as induced charge electrokinetic and electroosmotic flows [119]. Scientists have been using multiphysics modeling to develop advanced models for combined electrokinetic motion of microparticles in microfluidic systems. This trend has been the driving force in optimizing the device development and discovering new functionalities for lab-on-a-chip applications.

As discussed previously, most commercially available magnetic microbeads, e.g., Dynabeads[®], are composed of mostly polystyrene that is electrically polarizable. Therefore, dielectrophoretic manipulation can be employed in addition to magnetic

manipulation. Combining these two manipulation methods on the same bead can produce more sophisticated manipulations. In this research, we are motivated to take advantage of both magnetic and polymetric properties of a popular magnetic bead and combine magnetic and dielectrophoretic manipulations on them. We believe combined magnetic and DEP manipulations can offer promising analytical tools for lab-on-a-chip applications and biomolecular interaction studies.

1.2 Research Objectives

Previous literature review suggests that parallel manipulation of individual microbeads is dictated by faster and cheaper analysis of chemical reactions and biomolecular interactions in lab-on-a-chip systems. As pointed out by Johansson et al. [120] in a recent paper that appeared in *Lab-on-a-Chip*, “without any doubt, the controlled [parallel] manipulation of single magnetic beads functionalized with specific molecules in a lab-on-a-chip environment has the potential of generating novel analytical tools and bioassay applications.” In this research, we were motivated to develop new analytical tools and to advance lab-on-a-chip system for bioassay applications through controlled parallel manipulation of individual magnetic microbeads. Specifically, the objectives of this research include developing new on-chip manipulation modes including translational, circular, and out-of-plane motions of individual magnetic beads in parallel. My goal is to apply these bead manipulation techniques for effective sample preparation, sensitive in-situ detection, and high-throughput biomolecular analysis on microchips. To realize these research objectives and goals, three specific aims were set forth.

Specific Aim I: Uniform assembly of individual magnetic microbeads on a chip for improved detection of biomolecules bound to bead surface

In microbead-based biosensing, assembling a group of microbeads in the sensing region with individual bead control can lead to easy identification of the number of beads with maximum contribution of each bead to sensing signal, hence increasing the sensitivity and limit of detection of bead-based assays. Because the spatial resolution of the magnetic energy landscape is determined by the size of the magnetic elements, for manipulating individual magnetic beads we consider magnets in size comparable to the size of the beads, i.e., in the range of sub-micrometer to micrometers. In this task, I will explore the use of arrays of soft magnets subjected to an external magnetic field for magnetic assembly of microbeads on a chip. Theoretical analysis will first be carried out to predict the feasibility and efficiency of individually trapping magnetic microbeads inside a microfluidic channel and uniformly assemble them on a surface with designated number density. I will then employ the state-of-art IC technology to fabricate soft magnets down to sub-micrometer scale. Once the assembly capability is experimentally proved, integration of the submicron magnets with sensing electrodes will be implemented for a bead-based electrochemical assay. The test of the integrated devices for assay sensitivity to target biomolecules bound on the bead surface will be shown.

Specific Aim II: High-speed circular motion and selective translation of individual magnetic microbeads on a chip for sample mixing and separation

Mixing of fluid flowing through microchannels is important in a variety of applications, however, it is difficult to mix solutions in microfluidic channels because micro flows are laminar in nature. Both passive and active micromixers have been developed to stretch and fold the flow inside microchannels [121][122]. In this specific aim, a new type of active micromixer will be developed to locally stir a continuous flow inside a microchannel with high-speed orbiting of individual magnetic beads around soft

magnets in an array. The motion of the beads will be induced by an external rotating magnet that applies a rotating magnetic field to the soft magnet array. The effectiveness of the rotating magnetophoresis system for mixing two streams of fluids in a microchannel will be explored. In addition, with specially designed magnetic chips and by adding controls for translating the external rotating magnet, I will investigate a new mechanism for transporting magnetic beads inside a microfluidic channel. I will also employ this transport mechanism for on-chip sorting of microbeads of different size. The realization of selective transport of microbeads can accomplish sample separation for subsequent *in-situ* analysis with multiplexing capability.

Specific Aim III: Combining dielectrophoretic and magnetic manipulations for out-of-plane motion of Dynabeads[®]

Because Dynabeads[®] are not only magnetic, but also polymetric, dielectrophoretic manipulation can be employed in addition to magnetic manipulation. In this task, we aim to combine the two manipulations to achieve the out-of-plane motion of the beads. Two modes of out-of-plane motions will be investigated: oscillation of the beads across the channel height by switching between magnetic attraction and DEP repulsion and high-resolution tweezing of the beads in liquid through fine-tuning the opposing magnetic and DEP forces. The oscillation of the beads across the channel height can be employed for bead interaction with multiple layers of sample fluid arranged from top to bottom of a microchannel, while high resolution tweezing of microbeads in liquid can find important application in biomolecular studies. I will investigate a new design of DEP electrodes capable of generating sufficiently large DEP force for levitating microbeads in typical biological buffer solutions across the channel height. Specially designed conductors that can be integrated with the DEP electrodes to produce sufficient magnetic force to localize

the beads and balance the DEP force will be employed. The fabrication and test of the integrated device for both out-of-plane oscillation and high-resolution tweezing of the microbeads will be discussed.

1.3 Dissertation Layout

The layout of the rest of this dissertation is as follows. In chapter 2, we will present the theoretical background and fundamental principles in magnetic and dielectrophoretic manipulations. In chapter 3, we will discuss the microfabrication techniques for making NiFe soft magnets and microfluidic channels on a chip, and the surface treatment of the magnetic chip for reducing non-specific adhesion of the microbeads on the chip surface. Chapter 4 will introduce a new platform for microbead-based immunoassay based on the magnetic assembly of the magnetic beads between interdigitated array electrodes. Chapter 5 will describe a magnetic micromixer for continuous flow in microchannels based on externally induced circular motion of magnetic beads on a magnetic chip. Chapter 6 will cover a magnetic transport and sorting device. In chapter 7, we will discuss the combined magnetic and dielectrophoretic manipulations of microbeads for out-of-plane motion. Finally, chapter 8 summarizes the contribution of this work and concludes the dissertation with recommendations for future work.

CHAPTER 2

Fundamentals of Magnetophoresis and Dielectrophoresis

2.1 Introduction to Magnetism

Magnetism is a property of materials that respond to an applied magnetic field at an atomic or subatomic level. All materials are influenced to greater or lesser degree by the presence of a magnetic field. Some are attracted to a magnetic field, others are repulsed by a magnetic field. Substances that are negligibly affected by magnetic fields include copper, aluminum, gases, and plastics. The magnetic state of a material strongly depends on temperature, so a material may exhibit more than one form of magnetism depending on its temperature.

The sources of magnetism include the electrons' orbital angular motion around the nucleus and the electrons' intrinsic, i.e., spin, magnetic moment. Ordinarily, electrons in a material are arranged such that their magnetic moments (both orbital and intrinsic) cancel out. This is due to electrons forming pairs with opposite intrinsic magnetic moments as a result of the Pauli Exclusion Principle, or combining into filled subshells with zero net orbital motion. In both cases, the electron arrangement is so as to exactly cancel the magnetic moments from each electron.

Depending on the magnetic behavior, magnetic materials can be categorized into three major groups: diamagnetic, ferromagnetic, and paramagnetic. Diamagnetism appears in all materials, and is the tendency of a material to oppose an applied magnetic field. However, in a material with paramagnetic properties (that is, with a tendency to enhance an external magnetic field), the paramagnetic behavior dominates. Thus, despite its universal occurrence, diamagnetic behavior is observed only in a purely

diamagnetic material such as bismuth and mercury. Paramagnetism is due to unpaired electrons, i.e. atomic or molecular orbital with exactly one electron in them. While paired electrons are required by the Pauli Exclusion Principle to have their spin magnetic moments pointing in opposite directions, causing their magnetic fields to cancel out, an unpaired electron is free to align its magnetic moment in any direction. When an external magnetic field is applied, these magnetic moments will tend to align themselves in the same direction as the applied field, enforcing the applied field. Once the external field is removed, the magnetic moments of paramagnetic materials are free to move and randomly oriented. In other words, paramagnetic materials can magnetize in an external field, but they promptly lose their magnetization when the field is removed.

The most well known form of magnetism is ferromagnetism that exhibits its own persistent magnetic field after the external field is removed. A ferromagnet, like a paramagnet, has unpaired electrons. However, in addition to the electrons' spin magnetic moment with a tendency to be parallel to an applied field, there is also in these materials a tendency for the magnetic moments to orient parallel to each other to maintain a lowered energy state. Depending on how strong the persistent remnant field is, ferromagnetic materials can be categorized into soft and hard ferromagnetic groups. The hard ferromagnetic materials such as the rare earth metal neodymium and gadolinium are used to make the permanent magnets. The soft ferromagnetic materials include nickel, iron, cobalt and their alloys.

When the size of a ferromagnet is sufficiently small, e.g., $< 15\text{nm}$, it acts like a single magnetic spin that is subject to Brownian motion. This behavior originates from

the competition between the nanoparticle's magnetic crystalline anisotropy energy and the thermal fluctuation energy. Since the crystalline anisotropy energy is proportional to the volume of the nanoparticle, there exists a critical size below which the particles cannot retain its preferred magnetization orientation inside the crystalline structure of the material. As a result, its response to a magnetic field is qualitatively similar to the response of a paramagnet, but much larger. Hence the term "superparamagnetism" was coined. The bulk property of such a system resembles that of a paramagnet, but on a microscopic level they are ordered to give remarkably strong magnetization in an external field.

2.2 Materials and Properties of Magnetic Beads

Magnetic particles are typically composed of iron, nickel, or cobalt, and their various oxidized derivatives. Depending on the types of magnetic ordering of spins within these materials, different nomenclature is used. Iron, nickel, and cobalt in pure metal form are referred to as ferromagnets, whereas their oxidized forms are referred to as ferrimagnets. Regardless of these differences, both types of material classes display common magnetic properties, including remanence, i.e., the ability to store magnetization in the absence of external field, and hysteresis, i.e., a history dependent magnetization. When ferro/ferrimagnetic materials are heated above the Curie temperature, the spin-spin coupling within the material is no longer sufficient to overcome thermal fluctuation energy. As a result, these materials begin to display different behavior characterized by a lack of remanence and hysteresis, which is referred to as paramagnetism. As discussed before, the term "superparamagnetism" was recently given to a class of very small metal or metal-oxide nanoparticles, usually

smaller than 15nm, that display extraordinarily large paramagnetic response to an external field even at temperatures below the Curie point.

With the increasing demand for polymer bead surface-based bioanalysis in the last few decades, there have been significant advances in synthesizing spherical polymer matrix that incorporates a dispersion of superparamagnetic nanoparticle grains. If the superparamagnetic grains are spaced sufficiently far apart inside the polymer matrix, then the composite microparticle will behave superparamagnetically and it will have a large dipole moment due to the collective effect of a large number of magnetic grains inside the bead. Popular suppliers of these polymer-based magnetic beads include Invitrogen Corp. (www.invitrogen.com/dynabeads), Bangs Laboratories (www.bangslabs.com), Polysciences (www.polysciences.com), Micromod (www.micromod.de), Seradyn (www.seradyn.com), and Estapor (www.estapor.com). In most cases, the magnetic materials comprise only a small fraction of the bead volume. The magnetic susceptibility of commercially available polymer-based magnetic beads is typically in the range of 0.1 - 1.5.

Dynabeads[®] from Invitrogen (Carlsbad, CA) is chosen in this study because of their superior quality and reproducibility. The uniformity of size, spherical shape, and surface area has a coefficient of variation (CV) less than 3%, and the level of reproducibility within and between batches is less than 5% (www.invitrogen.com/dynabeads). CV is the standard deviation given as percentage of the mean. The tightly controlled bead variability is extremely important to our study, which aims for parallel manipulation with individual bead control. Also, the same surface

area offered for each experiment will ensure the best efficacy and reliability for our individual bead-based analysis.

Dynabeads[®] are made by incorporation of evenly dispersed γ -Fe₂O₃ and Fe₃O₄ nanoparticles in the range of 8-15nm in highly cross-linked porous polystyrene beads. To encapsulate the magnetic material and provide a defined surface the beads are further coated with a thin polymer shell without charge [123]. The biological derivatization of surface takes place on the outer polymer shell, which can be hydrophilic or hydrophobic for different applications. A schematic of such a bead is shown in figure 2.2.

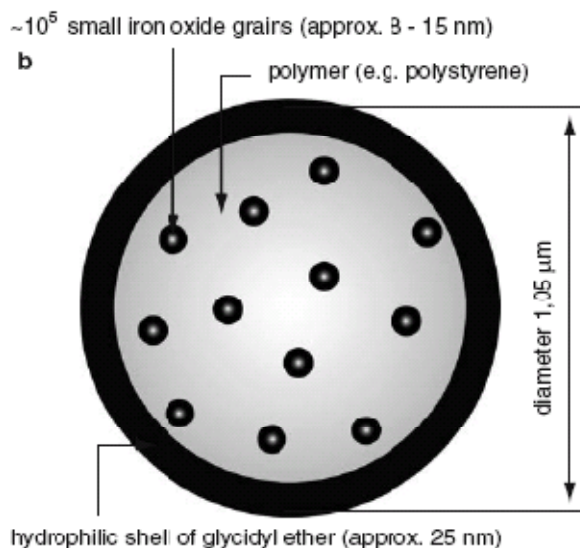


Figure 2.1: The schematic composition of a Dynabead[®] MyOne[™]
This figure is adapted from [124].

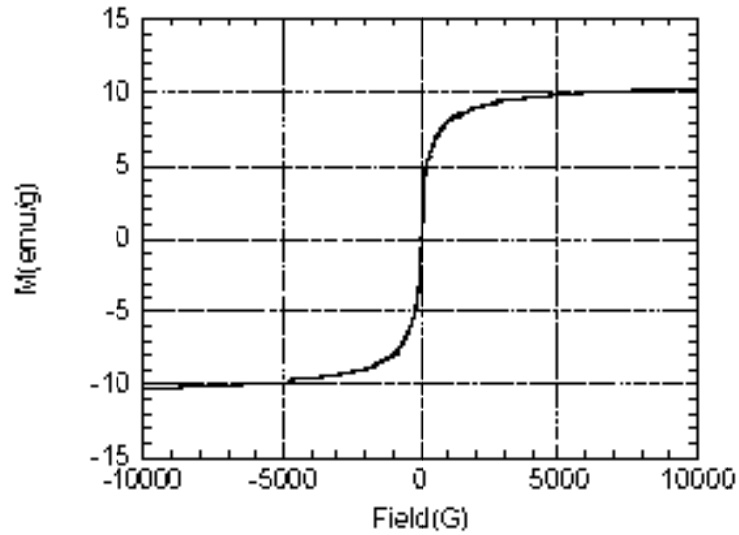
Two different sizes of Dynabeads[®], MyOne[™] (1μm) and M280[™] (2.8μm), were chosen in this studies. The advantages of using smaller beads include higher binding capacity and lower sedimentation rates. For example, the binding capacity for biotinylated immunoglobulin on MyOne tosyl-coated with streptavidin increases to 11–12μg/mg from 3.5–4.0μg/mg for M280 [125]. However, with smaller beads, the

magnetophoretic mobility is less (see equation 2.17), making them harder to be manipulated in a magnetic field. One of the remedies is to incorporating a higher fraction of magnetic material in the polystyrene matrix to increase the effective susceptibility. The characterization of the two different beads is given in Table 2.1.

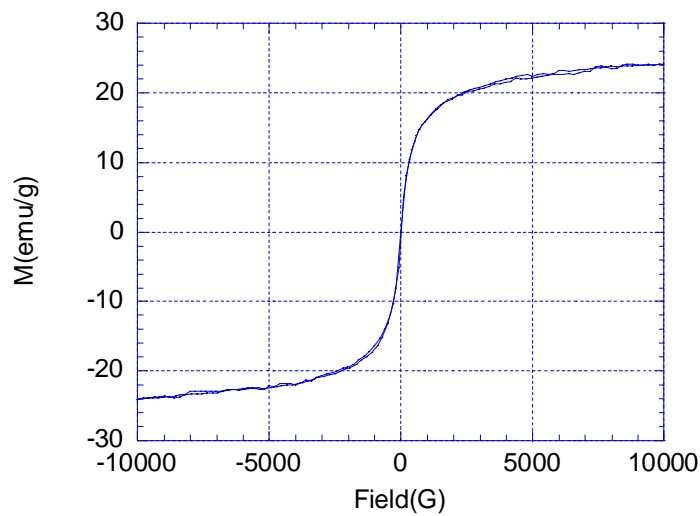
Table 2.1: Material properties of Dynabeads
(Source: manufacturer's MSDS)

	<i>R</i> (μm)	<i>ρ</i> (g/cm^3)	<i>Iron</i> (mg/g)	<i>χ_{eff}</i>	<i>M_s</i> (kA/m)
M280	1.4	1.4	118	0.76	15
MyOne	0.5	1.7	255	1.38	40

The hysteresis curves of these beads measured by a vibrating sample magnetometer (VSM) and provided by the manufacturer is shown in figure 2.3. Due to the small size (less than 15nm) of the iron domains and the controlled dispersion within the polystyrene matrix, these beads are superparamagnetic. The superparamagnetic behavior of these beads indicates that the inter-particle interactions among the maghemite nanoparticles inside the beads are insufficient to lead to blocking of the nanoparticle magnetization during the time of measurement [125].



a)



b)

Figure 2.2: The magnetization curves of Dynabeads a) M280 and b) MyOne measured on highly concentrated suspensions (Source: Manufacturer's data)

Magnetic beads with superparamagnetic property are desirable in magnetic manipulation of individual beads, since the clustering of beads may be avoided during use. We note the linear magnetization region for both MyOne and M280 beads is within

± 1000 Gauss, i.e., ± 100 mT, although the saturation moment of MyOne is much higher than that of M280 due to high composition of iron.

2.3 Theory on Magnetophoresis

2.3.1 Magnetic Force

When a magnetic dipole is placed in a non-uniform magnetic field, the net force on the dipole due to the applied field is given by:

$$\vec{F}_M = \nabla(\vec{m} \cdot \vec{B}) \quad (2.1)$$

where \vec{m} is the magnetic dipole moment and \vec{B} is the magnetic field at the center of the dipole. In the case of a magnetic microbead in a non-uniform magnetic field, an integral form of equation (2.1) is necessary.

$$\vec{F}_M = \int_V \nabla(\vec{m} \cdot \vec{B}) dV \quad (2.1a)$$

With certain assumptions, e.g., a magnetically homogeneous bead with radius R small enough compared to the variation of applied field so that $R|\nabla\vec{B}| \ll |\vec{B}|$ hold true in any direction, then the magnitude (but not the gradient) of the field within the interior extent of the microbead, \vec{B}_{in} , can be taken as constant. In this case, a simple vector identity can be used to rewrite equation (2.1) as follows:

$$\nabla(\vec{m} \cdot \vec{B}) = \vec{m} \times (\nabla \times \vec{B}) + \vec{B} \times (\nabla \times \vec{m}) + (\vec{m} \cdot \nabla)\vec{B} + (\vec{B} \cdot \nabla)\vec{m} \quad (2.2)$$

The first term on the right-hand-side (RHS) of equation (2.2) involves the curl of the magnetic flux density, which could be expanded as

$$\vec{m} \times (\nabla \times \vec{B}) = \vec{B} \times (\nabla \times \vec{H}) + \vec{m} \times (\nabla \times \vec{m}) \quad (2.3)$$

The curl of the magnetic field is 0 everywhere within the microbead, since the polymer-based magnetic beads are insulating and do not support electrical currents. Hence, the

first term on the RHS of equation (2.3) vanishes. The curl of the magnetization is 0 inside the microbead, but across its surface, the effective magnetization changes. Therefore, surface contributions to the force should, in general, be considered. However, since the magnetization of the microbead is assumed to be constant, when integrated around the bead the second term of equation (2.3) also vanishes due to symmetry. The same reasoning could be applied to the 2nd term in equation (2.2). With a constant magnetization of the microbead, the 4th term in (2.2) is 0 inside the microbead and will integrate to 0 around it. We are then left with the only term that involves the non-zero gradient of the field vector, and equation (2.1a) can be approximated by

$$\vec{F}_M = \int_V (\vec{m} \cdot \nabla) \vec{B} dV \quad (2.4)$$

The interpretation of the expression $(\vec{m} \cdot \nabla)$ is the differentiation with respect to the direction of vector \vec{m} multiplied by the magnitude of vector \vec{m} . The components of the magnetic force, \vec{F}_M , arise as the result of the differentiation (gradient) along vector \vec{m} of respective components of vector, \vec{B} . In general, the resulting expression for magnetic force is a function of spatial coordinates, which bears no obvious relationship to the direction of the magnetic field vector or the field lines [126].

The effective dipole moment \vec{m}_{eff} of a magnetically homogeneous bead is given by

$$\vec{m}_{eff} = V\vec{M} \quad (2.5)$$

where V is volume of the bead and \vec{M} the volume magnetization. In general, the volume magnetization of the bead is a nonlinear function of applied magnetic field due to saturation phenomenon. For simplicity, we approximate the nonlinear function with a linear region and a saturation region. With a linear magnetization relationship,

$$\vec{M} = \chi \vec{H}_{in} \quad (2.6)$$

where χ is intrinsic magnetic susceptibility of the magnetic bead material. Determining the magnetic field inside the bead requires consideration of the demagnetization field within the bead, i.e. $\vec{H}_{in} = \vec{H} - \vec{H}_{demag}$. For a spherical geometry, $\vec{H}_{demag} = \vec{M}/3$. Hence,

$$\vec{M} = \frac{3\chi}{3 + \chi} \vec{H} \equiv \chi_{eff} \vec{H} \quad (2.7)$$

χ_{eff} is defined as the effective magnetic susceptibility that takes into consideration the demagnetization effect of the particles. For dilute bead suspension with a diamagnetic medium such as water, magnetic fields \vec{H} and \vec{B} are simply related by the magnetic permeability of vacuum $\mu_0 = 4\pi \times 10^{-7} \text{ H/m}$. Hence, combining Equation (2.4) and (2.7) gives the effective average magnetic force

$$\vec{F}_M = \frac{\chi_{eff} V}{\mu_0} (\vec{B} \cdot \nabla) \vec{B} \quad (2.8)$$

For time-independent field (magnetostatics) with no electric current, the following vector identity $\nabla(\vec{B} \cdot \vec{B}) = 2(\vec{B} \cdot \nabla) \vec{B} + 2\vec{B} \times (\nabla \times \vec{B})$ can be used to reduce $(\vec{B} \cdot \nabla) \vec{B} = \frac{1}{2} \nabla(\vec{B} \cdot \vec{B}) = \frac{1}{2} \nabla |\vec{B}|^2$, because the curl of magnetic field vector vanishes (no source of magnetic field within the medium). Thus, Equation 2.8 can be expressed as

$$\vec{F}_M = \frac{\chi_{eff} V}{2\mu_0} \nabla |\vec{B}|^2 \quad (2.9)$$

From this expression, we note the direction of magnetic force simply follows the steepest gradient of the field strength squared. The magnetic energy of the bead inside a static magnetic field can be derived from equation (2.9) using the relation $\vec{F}_M = -\nabla U_M$ and the

result is $U_M = \frac{\chi_{eff} V}{2\mu_0} |\vec{B}|^2$. In deriving this result, we manually assigned a negative sign to

the magnetic force expression (equation 2.9) by assuming the force is always attractive.

The term $\frac{1}{2\mu_0} |\vec{B}|^2 = \frac{1}{2} \vec{B} \cdot \vec{H}$ is a measure of energy density of the static magnetic field.

Therefore, the magnetic force will drive a magnetic bead in a direction that follows the steepest ascend of the energy density of the non-uniform field.

If the applied field is beyond the saturation field for a given magnetic microbead, the magnetization is independent of the strength of the applied field and the force is given by

$$\vec{F}_M = V(\vec{M}_s \cdot \nabla)\vec{B} \quad (2.9a)$$

The component form of equation (2.9a) is given by:

$$\begin{aligned} F_{M_x} &= V \left(M_{s_x} \frac{\partial B_x}{\partial x} + M_{s_y} \frac{\partial B_x}{\partial y} + M_{s_z} \frac{\partial B_x}{\partial z} \right) \\ F_{M_y} &= V \left(M_{s_x} \frac{\partial B_y}{\partial x} + M_{s_y} \frac{\partial B_y}{\partial y} + M_{s_z} \frac{\partial B_y}{\partial z} \right) \\ F_{M_z} &= V \left(M_{s_x} \frac{\partial B_z}{\partial x} + M_{s_y} \frac{\partial B_z}{\partial y} + M_{s_z} \frac{\partial B_z}{\partial z} \right) \end{aligned} \quad (2.9b)$$

The superparamagnetic property of the microbead leads to the alignment of the saturated magnetic moment with the direction of the local field. Therefore, the components of the saturated moment \vec{M}_s can be calculated by:

$$\begin{aligned} M_{s_x} &= |\vec{M}_s| \cos(\tan^{-1}(B_y/B_x)) \\ M_{s_y} &= |\vec{M}_s| \sin(\tan^{-1}(B_y/B_x)) \\ M_{s_z} &= |\vec{M}_s| \sin\left(\tan^{-1}\left(B_z/\sqrt{B_x^2 + B_y^2}\right)\right) \end{aligned} \quad (2.10)$$

Therefore, the final direction of magnetic force for saturated bead case depends on the local field as well as the local field gradient, both of which strongly depend on the spatial coordinates for a practical magnetic system. We note that although the strength of the externally applied field, once it is beyond the saturation field strength, does not affect the magnetic moment of the beads, it does change of the direction of the magnetic moment as implied by equation (2.10). As a result, the actual strength of the external field still has an effect on the magnetic force exerted on the nearby beads.

In both linear and saturated magnetization situations, we note from equations (2.9) and (2.9a) a uniform magnetic field does not generate any magnetic force, although it will induce a magnetic moment on the bead. It is the magnetic field gradient that is responsible for the force exerted on a magnetic bead, and, for this reason magnetic separation systems are designed to maximize field gradients. Non-uniformity can be introduced to a pre-existing uniform field by the presence of a soft magnetic object, such as iron, nickel, cobalt, and their alloys. This is because an externally applied magnetic field can magnetize the soft magnetic materials by causing the alignment and growth of magnetic domains in the direction of the external field, giving a large multiplication of the applied field within the soft magnetic object. A current-carrying wire also produces a non-uniform electromagnetic field, which decreases with distance away from the wire. Note also the magnetic force scales with volumetric size of the bead, therefore, the required field and field gradient to exert a certain force on a magnetic bead increase rapidly as the bead becomes smaller.

2.3.2 Force Balance in Magnetophoresis

The induced motion of the magnetic particles in liquid due to a magnetic field is referred to as magnetophoresis (MAP). To determine the magnetophoresis of a magnetic microparticle in a viscous medium such as water, one needs to analyze all the relevant forces on the particle. A schematic of the force polygon for magnetophoresis is shown in figure 2.3.

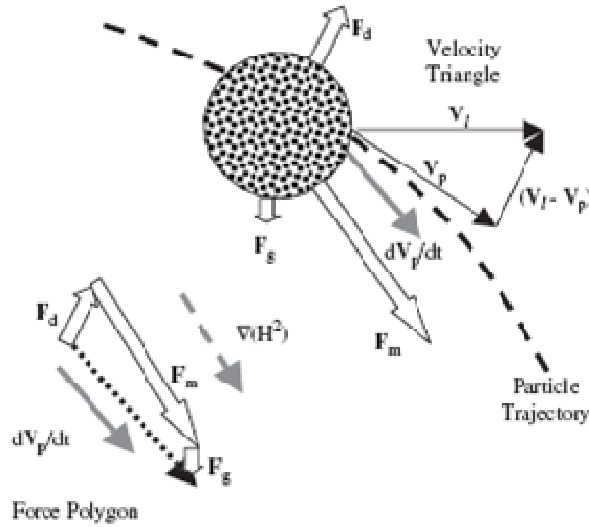


Figure 2.3: Forces on a particle in fluid subjected to a non-uniform magnetic field

The equation of motion of the particle is given by:

$$\vec{F}_D + \vec{F}_M + \vec{F}_G = m\dot{\vec{u}}_p \quad (2.11)$$

where \vec{F}_D is the drag force, \vec{F}_M the magnetic force on the particle, and \vec{F}_G is the gravity/buoyancy force on the particle.

For a $1\mu\text{m}$ bead moving in water, the Reynolds number, $Re = \rho LU / \eta$, of the flow field is ~ 1 when the speed of the bead is 1m/s. In most cases, the speed of microbeads

inside a microfluidic device is in the order of mm/s, therefore, Reynolds number associated with typical motion of microbeads in microfluidic channel is much less than 1, which permits the neglect of the inertial terms in the Navier-Stokes equations that govern the fluid motion. With further assumptions of incompressible fluid with constant density and viscosity, the Navier-Stokes equations reduce to:

$$\nabla p = \eta \nabla^2 \vec{u} \quad (2.12)$$

where p is the pressure and \vec{u} the velocity of the fluid.

The continuity equation is given by:

$$\nabla \cdot \vec{u} = 0 \quad (2.13)$$

With proper boundary conditions for the bead moving inside a bulk solution, equations (2.12) and (2.13) can be solved simultaneously to obtain the drag force exerted on the bead by the fluid. The result is the well-known Stokes' law as given by:

$$\vec{F}_D = 6\pi R \eta (\vec{u} - \vec{u}_p) \quad (2.14)$$

where η is the dynamic viscosity of the liquid that suspends the particles, R and \vec{u}_p denote the radius and velocity of the particle, respectively.

Among the three forces, only the fluid drag force is a function of the particle velocity, therefore, equation (2.11) can be integrated to solve for the particle velocity by treating the other two forces as known, i.e.,

$$\vec{u}_p = \frac{\vec{F}_M + \vec{F}_G}{6\pi\eta R} \left(1 - e^{-\frac{t}{\tau}} \right) \quad (2.15)$$

where $\tau = \frac{2\rho_p R^2}{9\eta}$ is the characteristic time constant for the particle to reach terminal

(steady-state) velocity. Due to the small size of the particle (e.g. 1-5 μ m), the time

constant of the particle is short ($\sim 0.1 - 2 \mu\text{sec}$) in a common fluid. As a result, the inertial term is small compared with other terms. Likewise, the gravity/buoyancy force $\vec{F}_G = V(\rho_p - \rho)\vec{g}$ is negligible. For example, for a $1\mu\text{m}$ bead with density of 2 g/cm^3 moving in water ($\eta = 8.9 \times 10^{-4} \text{ Pa}\cdot\text{s}$ at 25°C) with a relative velocity of 1mm/sec , the fluid drag $\vec{F}_D \approx 8.4 \text{ pN}$, while the gravity/buoyancy force $\vec{F}_G \approx 5 \times 10^{-3} \text{ pN}$, and the inertial force of the particle is less than 1 pN unless the particle acceleration exceeds an impossibly large value of 1000m/s^2 . Therefore, equation (2.11) can be simplified as:

$$\vec{F}_D + \vec{F}_M = 0 \quad (2.16)$$

Solve for terminal velocity of the particle using equation (2.9) and (2.14),

$$\vec{u}_p = \xi_l \nabla |\vec{B}|^2 + \vec{u}_m \quad (2.17)$$

with $\xi_l = \frac{\chi_{\text{eff}} R^2}{9\eta\mu_0}$, referred to as magnetophoretic mobility of the magnetic particle under

linear magnetization. In the case of the magnetically saturated beads,

$$\vec{u}_p = \xi_s \nabla \vec{B} + \vec{u}_m \quad (2.17a)$$

with $\xi_s = \frac{2R^2 M_s}{9\eta}$ as the magnetophoretic mobility of the particle under magnetic

saturation. In a highly non-uniform magnetic field, \vec{B} and the quantity $|\vec{B}|^2$ strongly vary

in space, hence a strong spatial variation of \vec{u}_p is expected in both linear and saturation

cases.

Once the velocity in space is known, the trajectory of the particle can be calculated by

$$\vec{s}(t + \delta t) = \vec{s}(t) + \int_t^{t+\delta t} \vec{u}_p dt \quad (2.18)$$

The trajectory of the particle determines whether the magnetic capture, or separation, of the particle from the fluid will occur or not. We used this mathematical model to guide us in the design of the magnetic capturing and assembly of magnetic particles inside a microfluidic channel. One notes that this model indicates a disproportional scaling of the drag force ($\sim R$) and the MAP force ($\sim R^3$).

Using the values from Table 2.1, we can calculate the magnetophoretic mobility of the Dynabeads in water and deduce the required magnetic field and field gradient for a desired magnetophoretic speed of these beads. The results are listed in Table 2.2. Based on equation (2.14) and (2.16), a magnetic force of 23.5pN and 8.4pN is needed to induce a motion of 1mm/sec relative to its suspending medium water for M280 and MyOne, respectively.

Table 2.2: Magnetophoretic mobility and required field properties under linear magnetization

Beads	ξ_l ($\text{m}^2/\text{T}^2 \cdot \text{s}$)	Required $\nabla \vec{B} ^2$ per 1mm/sec relative speed (T^2/m)
M280	1.5e-4	6.7
MyOne	3.4e-5	29.4

Table 2.3: Magnetophoretic mobility and required field properties under magnetic saturation

Beads	ξ_s ($\text{m}^2/\text{T} \cdot \text{s}$)	Required $\nabla \vec{B}$ per 1mm/sec relative speed (T/m)
M280	7.34e-6	136
MyOne	2.5e-6	400

We note the relation between magnetophoretic speed and magnetic field properties $\nabla|\vec{B}|^2$ for linear magnetization case and that between magnetophoretic speed and $\nabla\vec{B}$ for saturation case are both linear. For a given design of the magnetic manipulation system, the value of $\nabla|\vec{B}|^2$ and $\nabla\vec{B}$ can be numerically calculated using magnetostatics theory (see discussion in chapter 4).

2.3.3 Scaling Law in Magnetophoresis

As discussed previously, a magnetic bead will follow the steepest ascent line of the magnetic energy of the non-uniform magnetic field. Therefore, the spatial resolution of the non-uniformity of the field determines the distribution of the trapped beads. In most cases, due to the relatively large size of the magnetic field generating elements compared to that of beads, an ensemble of microbeads were attracted to individual energy wells [68][71]. In this work, we intend to localize individual microbeads into a two dimensional array, without agglomeration of them in a spot on the surface. According to the study of Yellen et al. [127], if the sizes of the magnetic field generating elements are comparable to that of the magnetic beads, trapping of single bead at each element is possible. Therefore, we plan to introduce an array of magnetic field generating elements with a characteristic length similar to the diameter of the magnetic beads to be manipulated, so that each magnetic element will capture one and only one bead from a flow of bead suspension inside a microchannel, leading to uniform distribution of the beads into a regular array.

The magnetic field generated by current-carrying wires is given by Biot-Savart Law:

$$\vec{B} = \frac{\mu_0 I}{4\pi} \int \frac{d\vec{l} \times \hat{r}}{r^2} \quad (2.19)$$

where I is the current, $d\vec{l}$ is a vector whose magnitude is the length of the differential element of the wire and direction follows the current flow, and \hat{r} is the displacement unit vector pointing from the wire element towards the point at which the field is computed. Equation (2.19) implies that the current, I , needs to be kept the same in order to generate the same field strength during the miniaturization. Meanwhile, the power density due to Joule heating within the footprint of the device is given by

$$P \approx \frac{I^2 R}{Ld} = \frac{I^2}{Ld} \left(\frac{\rho L}{A} \right) = \frac{\rho I^2}{Ad} \approx \frac{\rho I^2}{d^3} \quad (2.20)$$

where R is the resistance of the wire, ρ the resistivity, I the current, A the cross-sectional area of the wire, d the characteristic length of the wire cross-section, and L the length of the wire, respectively. Equation (2.20) implies that in order to keep the power from growing without bound, current needs to be proportional to the cross-sectional length scale of the wire, i.e., Joule heating in principle limits the current as $I \sim d^{3/2}$. As a result, the magnetic field scales as $\vec{B} \sim d^{3/2}$, resulting in $\vec{F}_M \sim d^{1/2}$ for saturated magnetization because $\vec{F}_M \sim \nabla |\vec{B}|$ (equations 2.9a), and $\vec{F}_M \sim d^2$ for linear magnetization due to $\vec{F}_M \sim \nabla |\vec{B}|^2$ (equations 2.9). These relationships indicate an unfavorable magnetic force scaling towards miniaturization.

On the contrary, for arrays of soft magnets inside an externally imposed magnetic field, the average field strength is the same regardless of the size of the soft magnets as

long as the magnetization of the soft magnets remains the same. Therefore, as the size of the soft magnets shrinks, both equations (2.9) and (2.9a) imply that $\vec{F}_M \sim d^{-1}$. This relation favors miniaturized systems. Furthermore, there is no heat generation in producing magnetic field and field gradient this way. Therefore, such a system is most suitable for miniaturization.

We note that, although magnetic field strength can be maintained with miniaturization for soft magnets, magnetic field gradient has a shorter reach into an extended spatial region with smaller size of soft magnets, resulting in a shorter acting distance of magnetic force inside the fluid (see detailed discussion in Chapter 4). This fact implies that the height of the microfluidic channel for magnetic particle delivery needs to be reduced for smaller magnetic elements at the bottom of the channel to achieve decent capture efficiency of the particle. In addition, magnetic force decreases rapidly with smaller beads (see equation 2.9 and 2.9a). These facts together cast a practical limitation on manipulating smaller particles using smaller magnetic elements. In the situation of thermal equilibrium (i.e. no fluid flow of any type or variation of variables with time), the probability of holding a particle by a magnetic trap against randomizing effects such as Brownian motion is small when the resulting change of magnetic energy is smaller than thermal fluctuation energy $k_B T$, where k_B is the Boltzmann constant and T is the absolute temperature [128].

Based on the foregoing discussion, we find it imperative to carry out a numerical analysis on magnetic force generated by a given design of miniaturized magnets and theoretically predict the effectiveness of the magnetic manipulation inside a given microchannel.

2.4 Theory on Dielectrophoresis

2.4.1 Dielectrophoretic Force

An electrically charged particle suspended in liquid moves in an electric field due to Coulomb force. This electrokinetic motion of particles is referred to as electrophoresis [57]. Neutral particles will not have electrokinetic motion in a uniform electric field. Nevertheless, they may be manipulated by a non-uniform electric field. In figure 2.4, we show that a dielectric neutral particle and the suspending medium become polarized when they are subjected to an electric field. Because of the polarization, electric charge separation occurs within the dielectric particle as well as in the liquid side of the solid–liquid interface, resulting in a dipole moment. The interaction between the dipole and the nonuniform field gives rise to a net force on the dipole. The induced motion of a dielectric neutral particle in a non-uniform electric field is referred to as dielectrophoresis (DEP) [93]. In the case shown in figure 2.4, the suspending medium is more polarizable than the particle, the induced dipole moment pointed to the electric field maxima. Because the repulsion force on the positive-charged end is greater than the attraction force on the negatively-charged end, the electrophoretic motion of the particle is away from the local electric field maxima, i.e., negative DEP. Similarly, for the case when the particle is more polarizable than the suspending medium, the electrophoretic motion of the particle is towards the local electric field maxima, i.e., positive DEP.

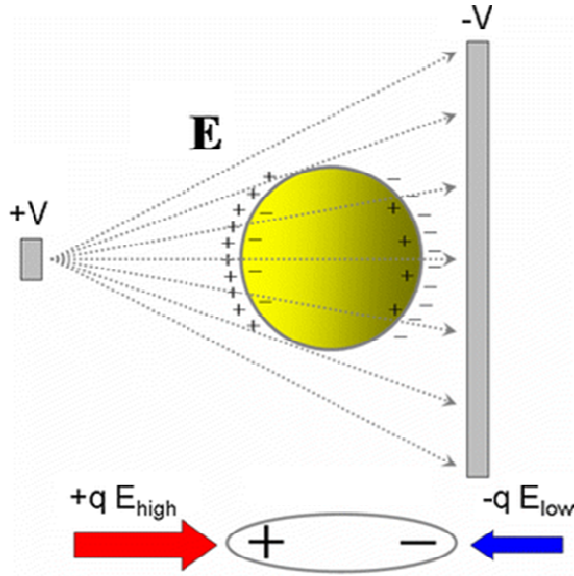


Figure 2.4: Illustration of the dielectrophoretic motion of a microparticle
This figure is adapted from Kang and Li [117].

To simplify the analysis, an electrically polarized particle can be described as an electric dipole. When an electric dipole is placed in an external electric field \vec{E} , the net force on the dipole due to the applied field is given by:

$$\vec{F}_{DEP} = (\vec{p} \cdot \nabla) \vec{E} \quad (2.21)$$

where \vec{p} is the electric dipole moment vector. In general, the resulting expression for \vec{F}_{DEP} is a function of spatial coordinates which bears no obvious relationship to the direction of \vec{p} and the field lines of the electric field \vec{E} . The situation improves significantly, however, for special cases to which simplifying assumptions apply. For a spherical microparticle (radius R) inside a magnetic field \vec{E} that slowly varies so that $R|\nabla\vec{E}| \ll |\vec{E}|$ hold true, the magnitude (but not the gradient) of the field within the interior extent of the microsphere can be approximated as constant.

The effective dipole moment \vec{p}_{eff} of a spherical, homogeneous particle embedded in a dielectric medium is given by

$$\vec{p}_{eff} = V\vec{P} = \left(\frac{4}{3}\right)\pi R^3 \vec{P} \quad (2.22)$$

where \vec{P} is the excess polarization and can be expressed as

$$\vec{P} = \varepsilon_o (K_2 - K_1) \vec{E}_{in} \quad (2.23)$$

where $\varepsilon_o = 8.854 \times 10^{-12} F/m$ is permittivity of free space, \vec{E}_{in} is internal electric field in the sphere in the direction of the external field, and K_1, K_2 are the relative dielectric constant of the medium and particle, respectively.

If the dielectric sphere is placed at the origin and subjected to a uniform z-directed electric field of magnitude E_o , the potential satisfies Laplace's equation and takes the

form as $\Phi_1(r, \theta) = -E_o r \cos \theta + \frac{A \cos \theta}{r^2}$, where $r > R$ and $\Phi_2(r, \theta) = -Br \cos \theta$, where

$r < R$. The boundary conditions at $r = R$ are $\Phi_1(r = R, \theta) = \Phi_2(r = R, \theta)$ and

$K_1 \varepsilon_o E_{r1}(r = R, \theta) = K_2 \varepsilon_o E_{r2}(r = R, \theta)$, where $E_{r1} = -\frac{\partial \Phi_1}{\partial r}$ and $E_{r2} = -\frac{\partial \Phi_2}{\partial r}$. With the

given boundary conditions, \vec{E}_{in} can be solved for and is given as: $\vec{E}_{in} = \frac{3K_1}{K_2 + 2K_1} \vec{E}$.

Accordingly, the effective dipole moment \vec{p}_{eff} is

$$\vec{p}_{eff} = 4\pi R^3 \varepsilon_o K_1 \left(\frac{K_2 - K_1}{K_2 + 2K_1}\right) \vec{E} = 4\pi R^3 \varepsilon_1 \left(\frac{\varepsilon_2 - \varepsilon_1}{\varepsilon_2 + 2\varepsilon_1}\right) \vec{E} \quad (2.24)$$

and combining Equation 2.21 and 2.24 gives the effective translational force

$$\vec{F}_{DEP} = 4\pi R^3 \varepsilon_1 \left(\frac{\varepsilon_2 - \varepsilon_1}{\varepsilon_2 + 2\varepsilon_1}\right) (\vec{E} \cdot \nabla) \vec{E} \quad (2.25)$$

where $\varepsilon_1 = K_1 \varepsilon_0$, $\varepsilon_2 = K_2 \varepsilon_0$. Since the electric field is a non-rotational or a conservative

field, $(\vec{E} \cdot \nabla) \vec{E} = \frac{1}{2} \nabla (\vec{E} \cdot \vec{E}) = \frac{1}{2} \nabla |\vec{E}|^2$ by the vector transformation

$(\vec{A} \cdot \nabla) \vec{B} = \nabla (\vec{A} \cdot \vec{B}) - (\vec{B} \cdot \nabla) \vec{A} - \vec{A} \times (\nabla \times \vec{B}) - \vec{B} \times (\nabla \times \vec{A})$ because the curl terms vanish.

Thus, Equation 7.5 can be expressed as

$$\vec{F}_{DEP} = 2\pi R^3 \varepsilon_1 \left(\frac{\varepsilon_2 - \varepsilon_1}{\varepsilon_2 + 2\varepsilon_1} \right) \nabla |\vec{E}|^2 \quad (2.26)$$

From equation (2.26), the strength of the DEP force depends strongly on the dielectric properties of the medium and the particle, particle's shape and size, as well as the amplitude and the non-uniformity of the electric field.

Equation (2.26) is based on the assumption of ideal dielectrics having zero conductivity. However, in the case of actual dielectrophoresis in which AC fields, rather than DC, are typically used (see discussion below), both the medium and the neutral particle are conductive. Thus, the simple permittivity ε needs to be replaced by the complex permittivity $\varepsilon^*(\omega) = \varepsilon - j \frac{\sigma}{\omega}$, where σ is electrical conductivity and ω is the angular frequency of the AC field. Under a time dependent external electric field, the time-averaged dielectrophoretic force is:

$$\langle \vec{F}_{DEP} \rangle = 2\pi R^3 \varepsilon_1 \operatorname{Re}\{f_{CM}(\omega)\} \nabla E_{rms}^2 \quad (2.27)$$

where $f_{CM}(\omega) = \frac{\varepsilon_2^*(\omega) - \varepsilon_1^*(\omega)}{\varepsilon_2^*(\omega) + 2\varepsilon_1^*(\omega)}$ is the Clausius-Mossotti factor and E_{rms} is the root

mean square value of the external electric field. From this force expression, one can note that the dependence of the dielectrophoretic force is determined by the real part of the Clausius-Mossotti factor. It determines both the magnitude and the sign of the

dielectrophoretic force. The value of the $\text{Re}[\tilde{f}_{CM}]$ factor ranges from -0.5 to $+1.0$, and can be calculated from the properties of the medium and the particle. The surface conductivity of the particle can be included in ε_1^* . If the value of $\text{Re}[\tilde{f}_{CM}]$ is positive, the particle moves toward higher electric field regions, and is termed positive dielectrophoresis, or pDEP. If the value of $\text{Re}[\tilde{f}_{CM}]$ is negative, the particle moves toward lower electric field regions, and is termed negative dielectrophoresis, or nDEP. For a solid homogeneous particle undergoing a single interfacial relaxation process, the characteristic frequency at which the direction of the dielectrophoretic force changes is known as the crossover frequency or Maxwell-Wagner relaxation frequency. This frequency depends on the conductivity and permittivity of the particle and the suspending medium.

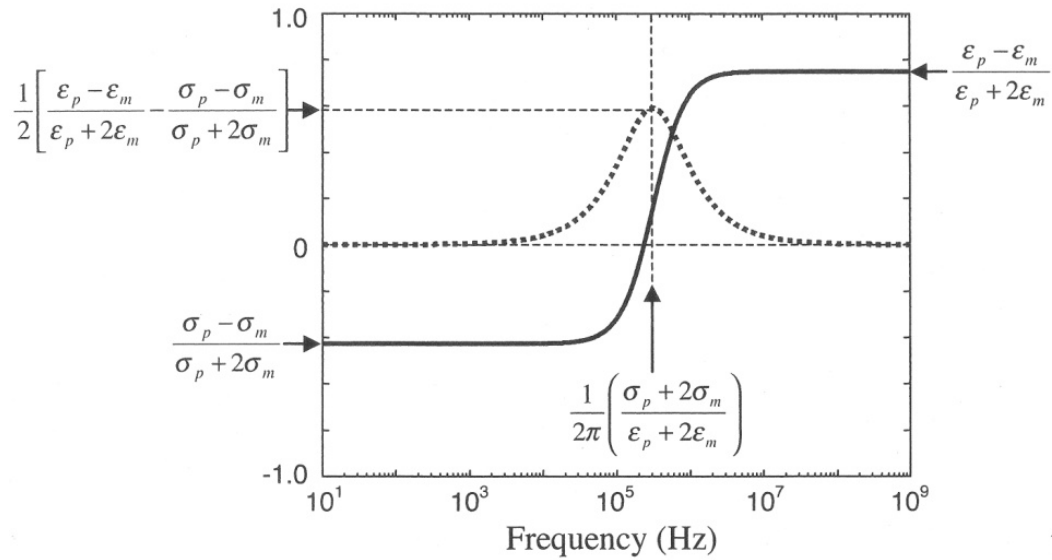


Figure 2.5: Real (solid line) and imaginary (dotted line) parts of the Clausius-Mossotti factor as a function of frequency of electric field

Figure 2.5 shows a representative plot of the real and imaginary parts of the Clausius-Mossotti factor. Indicted in the figure are the limiting values at high and low

frequencies of the real part and the value of the imaginary part at the Maxwell-Wagner relaxation frequency, at which the imaginary part of the Clausius-Mossotti factor reaches a maximum value. $\text{Im}[\tilde{f}_{CM}]$ values range from -0.75 to 0.75. It is clear that the low frequency limiting value of $\text{Re}[\tilde{f}_{CM}]$ depends only on the conductivity, while the high frequency limiting value of $\text{Re}[\tilde{f}_{CM}]$ depends only on the permittivity of the particle and the suspending liquid. $\text{Re}[\tilde{f}_{CM}]$ values range from -0.5 to 1.

The use of AC fields helps damp out the electrophoresis of particles in case they are charged, and the possible electro-osmosis of the medium. It also minimizes Joule heating and possible electrochemical reactions of the medium under electrical potentials. Electrochemical effects are typically avoided by operating at greater than tens of kHz in saline and lower frequencies can be tolerated in liquids of lower ionic strength [42].

Because the major component of Dynabeads[®] is polystyrene (see figure 2.1), which is polarizable in electric field, dielectrophoresis can be used to manipulate them in a liquid medium. The analysis on the motion of equation and numerical calculations on dielectrophoretic mobility of the Dynabeads[®] in a given medium are similar to the analysis on magnetic manipulation discussed in section 2.3.2.

2.4.2 Scaling Law in Dielectrophoresis

The electric field generated by electrical potentials on a pair of electrodes is given by $\vec{E} = \frac{V}{d}$, where V is the voltage on the electrodes, d is the characteristic length scale of the electrodes. The relation implies that the field strength increases with miniaturization. Meanwhile, Joule heating scales as $\Delta T = |\vec{E}|^2 d^2$ [129]. Therefore, maintaining the same

electrical potential on miniaturized electrodes does not necessarily increase the local temperature, i.e., Joule heating does not put a limit on the applied voltage with respect to miniaturization. As a result, the electrical field can practically scale as $\vec{E} \sim d^{-1}$, leading to $\vec{F}_{DEP} \sim d^{-3}$ because $\vec{F}_{DEP} \sim \nabla |\vec{E}|^2$ (equations 2.26 and 2.27). This relationship indicates an extremely favorable DEP force scaling towards miniaturization. Recall that the magnetic force from current-carrying conductors scales unfavorably with miniaturization, as discussed in section 2.3.

CHAPTER 3

Microfabrication of Soft Magnets and Microfluidic Channels

3.1 Introduction

As discussed in chapter 2, using arrays of soft magnets inside an externally imposed magnetic field for magnetic manipulation has advantages over conducting wires in miniaturized systems. The scaling law of magnetic force indicates smaller soft magnets actually produce a larger holding force for the same magnetic microbead. At the same time, the force generated by smaller magnets is confined in a smaller space due to the shorter extent of magnetic field gradient, limiting the acting distance for bead manipulation. The study of the magnitude and the acting distance of the magnetic force from small soft magnets will be presented in chapter 4. In this chapter, we study the ways of fabricating small soft magnets.

3.2 Microfabrication of Soft Magnets

3.2.1 Selection of Soft Ferromagnetic Materials

Although several soft magnetic materials are available, NiFe alloys were chosen in this work because of their excellent magnetic properties such as high permeability, low coercivity, and near zero magnetostriction, i.e., stresses in the material will not impact its magnetic performance. The most attractive properties of NiFe alloy for our work is that it easily saturates at a relatively high flux density ($\sim 1.5\text{T}$) in an externally applied field as small as 1mT [130], making the field gradient independent on the variability in the strength of external field in typical experimental arrangement. A summary of the magnetic properties of the common NiFe alloys is listed in Table 3.1.

Table 3.1: Magnetic properties of common NiFe alloys
 (Source: "*Electrical Engineering Handbook*", edited by Richard C. Dorf, IEEE Press,
 ©1993, ISBN 0-8493-0185-8)

Material	Approx % Composition				Permeability at B=20G	Maximum permeability	Saturation flux density (kA/m)
	Fe	Ni	Mo	Other			
45 Permalloy	55	45	--	--	2,500	25,000	1273
Hipernik	50	50	--	--	4,500	70,000	1273
80 Permalloy	20	80	--	--	8,000	100,000	851
Mu metal	15	75	--	10	20,000	100,000	517
Supermalloy	16	79	5	--	100,000	800,000	637

Furthermore, NiFe alloy is compatible with precision micromachining and it has become one of the most well characterized thin film magnetic materials, due to its wide use in magnetic recording heads by that large industry [131]. With current microfabrication technologies, patterning NiFe magnets with physical dimensions close to the size of microparticles is straightforward.

3.2.2 Microfabrication of NiFe Patterns Using eBeam Evaporation

Figure 3.1 sketches a common fabrication procedure based on evaporation of a NiFe alloy. Note the last step in figure 3.1 for SiO₂ deposition is necessary for two reasons. For one, NiFe material may be subject to slow corrosion on exposure to an aqueous environment. In addition, surface modification is required to prevent non-specific adhesion of microbeads to the surface and SiO₂ is very well studied for this purpose. The successful deposition of this SiO₂ layer requires using a low temperature process in order to prevent NiFe from being oxidized, which will cause it to lose magnetic properties. Regular PECVD process operates at a temperature greater than

200°C and cannot be used. We chose to use Electron Cyclotron Resonance (ECR) PECVD, a technology that produces higher density plasmas and better ion separation than a parallel-plate reactor, and the film deposition occurs at room temperature.

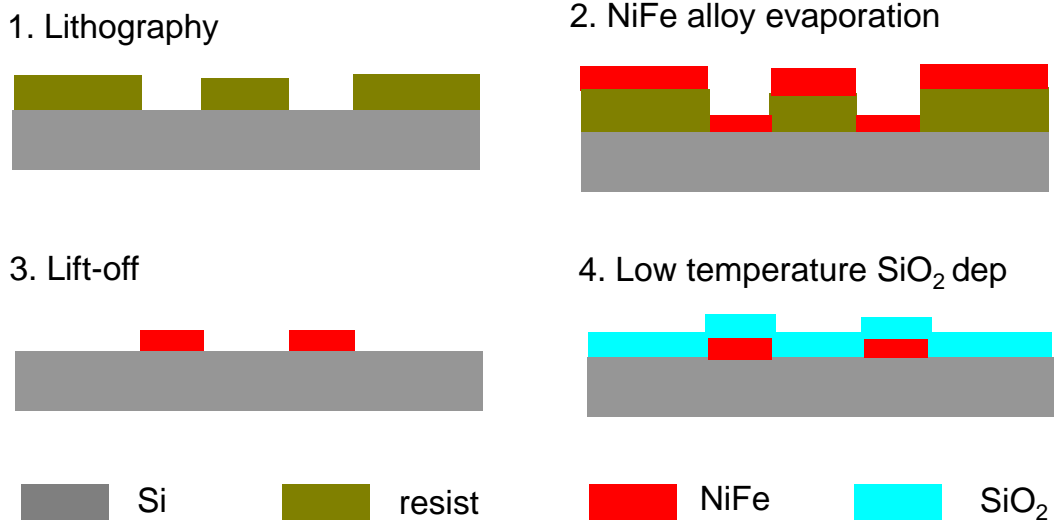


Figure 3.1: Fabrication procedure for NiFe soft magnets based on eBeam evaporation

The fabrication procedure based on the evaporation of NiFe alloy is relatively simple. However, it cannot produce relatively thick magnets because the stress in an evaporated NiFe film increases significantly with the thickness of the deposit. The thickest NiFe magnets we successfully fabricated in this way were about 200nm with a 20nm Ti adhesion layer. Cooling the sample during the deposition and/or increasing the thickness of Ti adhesion layer can help make relatively thicker magnets, but the stress issue does prevail in this fabrication method.

A typical fabrication result for square and rectangular NiFe soft magnets is shown in figure 3.2a) and b), respectively. For submicron feature of the magnets, electron beam lithography was used to pattern a special eBeam lithography resist, ZEON's ZEP-520, in step 1 of figure 3.1. Otherwise, regular UV lithography can be used with common

photoresist such as Shipley's S-1813. The energy-dispersive x-ray spectroscopy (EDX) inspection on these NiFe magnets (figure 3.3) indicates a nickel-to-iron ratio about 84:16. This composition is close to that of 80-permalloy ($\text{Ni}_{80}\text{Fe}_{20}$), the properties of which are well characterized and listed in Table 3.1, hence we expect similar magnetic properties.

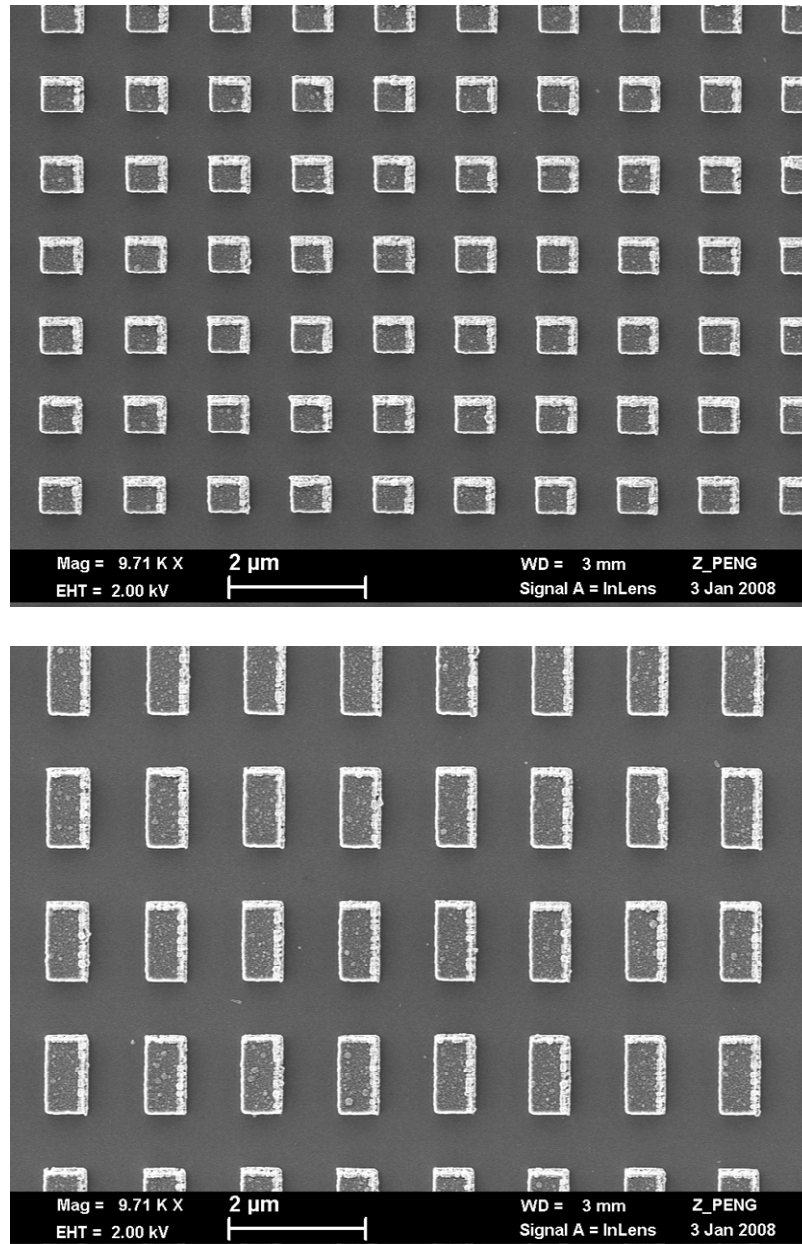
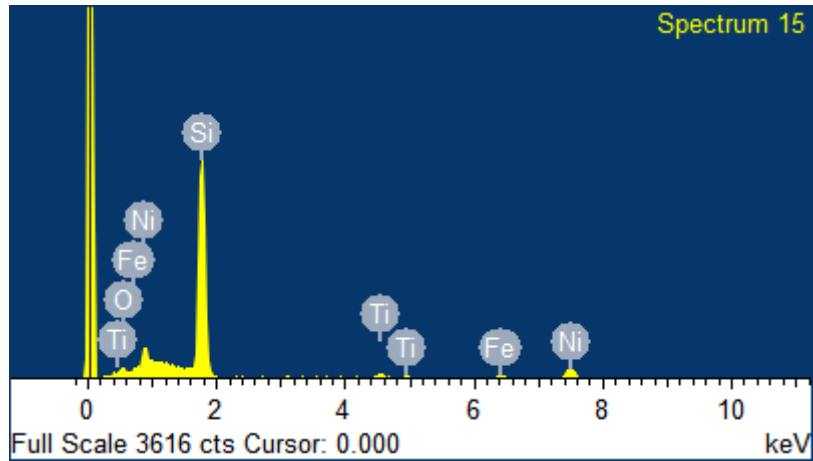


Figure 3.2: SEM image of evaporated NiFe magnets (thickness = 0.2 μm)



Element	App Conc.	Intensity Corr.	Weight%	Weight% Sigma	Atomic%
O K	2.94	0.6335	14.20	1.52	24.65
Si K	20.97	0.9581	66.90	1.34	66.15
Ti K	0.49	0.8200	1.84	0.27	1.07
Fe K	0.76	0.8913	2.59	0.37	1.29
Ni K	4.12	0.8718	14.46	0.69	6.84
Totals			100.00		

Figure 3.3: EDX analysis of the NiFe magnets fabricated by evaporation (Note because of the thin layer of the NiFe magnets, the materials beneath including the adhesion metal Ti and the Si substrate were also detected by EDX.)

3.2.3 Microfabrication of NiFe Patterns Using Electroplating

An alternative fabrication technique is through electroplating as depicted in figure 3.4. The electrodeposition of NiFe alloys can be carried out in three different plating baths: nickel chloride based Watts bath, sulphate bath, or sulphamate bath. Nickel sulphate bath is most commonly used to electrodeposit NiFe films with low stress and good uniformity [132]. Therefore, a sulphate bath was prepared according to Table 3.2 for this work.

1. Grow SiO₂ on Si



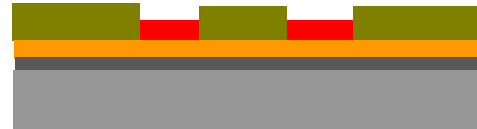
2. Deposit seed layer on SiO₂



3. Resist coating and patterning



4. Electroplating NiFe



5. Remove resist



6. Low temperature SiO₂ dep

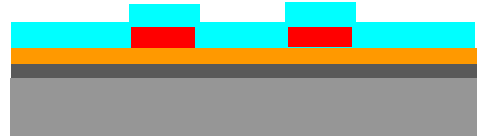


Figure 3.4: Fabrication procedure for NiFe soft magnets based on electroplating

Table 3.2: Chemical composition of NiFe electroplating bath

Chemical Name	Compound	mg/L
Nickel Sulfate Hexahydrate	NiSO ₄ · 6H ₂ O	200
Ferrous Sulfate Heptahydrate	FeSO ₄ · 7H ₂ O	8
Nickel Chloride Hexahydrate	NiCl ₂ · 6H ₂ O	5
Boric Acid	H ₃ BO ₃	25
Saccharin		3
Ascorbic Acid		1
Coumarin		0.3

The bath composition as well as plating conditions determines the properties of electrodeposited film. For fabricating micron size NiFe magnets, we require a nano-crystalline film. In addition, low surface roughness during the electroplating process is essential for uniform plating into small openings in resist mold. We used Solartron SI-1287 electrochemical interface to supply constant and precise current in the electroplating system. A continuous magnetic stirrer was provided to ensure a uniform bath composition during the plating process. The plating condition is optimized by conducting a series of identical experiments with different current density. As a result, $15\text{mA}/\text{cm}^2$ was determined to produce the best nano-crystalline film with low surface roughness. The deposition rate is about $0.2\mu\text{m}/\text{min}$. With these plating conditions, the stress of NiFe structures was significantly reduced and thickness of the soft magnets could be increased dramatically. According to the numerical simulation (see chapter 4), thicker soft magnets can increase the magnetic capturing force and act on beads at a farther distance from the device surface.

A typical fabrication result for cylindrical soft magnets is shown in figure 3.5. The energy-dispersive X-ray spectroscopy inspection on these NiFe magnets (figure 3.6) indicates a nickel-to-iron ratio about 56:44. This composition is close to that of Hipernik ($\text{Ni}_{50}\text{Fe}_{50}$), the properties of which are well characterized and listed in Table 3.1. Hence we expect similar magnetic properties of our electroplated NiFe magnets.

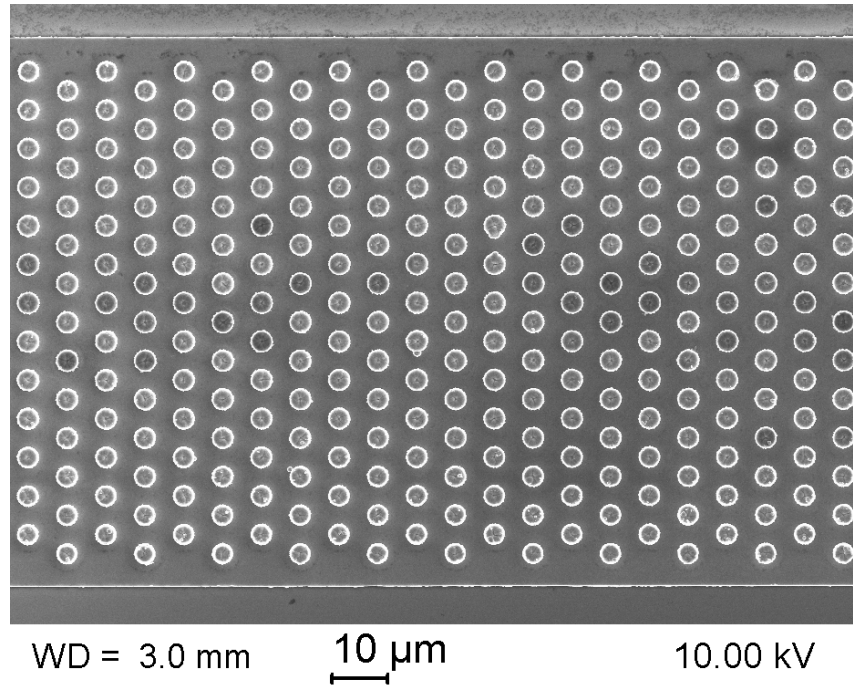
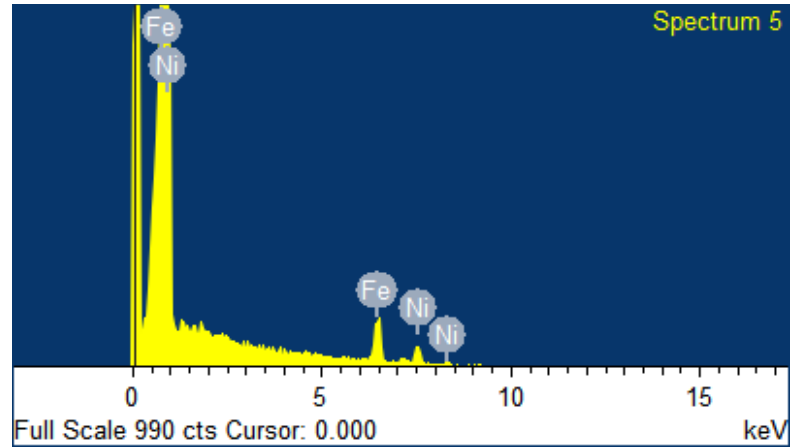


Figure 3.5: SEM image of electroplated cylindrical NiFe magnets on Cu seed layer (thickness = 1.2 μ m)



Element	Weight%	Atomic%
Fe L	42.59	43.81
Ni L	57.41	56.19
Totals	100.00	

Figure 3.6: EDX analysis of the NiFe magnets fabricated by electroplating

3.3 Fabrication of Microfluidic Systems

The microchannel and fluidic connectors were fabricated using soft lithography [133], by molding poly(dimethylsiloxane) (PDMS) resin (Sylgard 184, Dow Corning) onto a photoresist (SU-8, Microchem) template. For convenient access to the microchannel by a microscope, we preferred to connect the microchannel to the macro world from the sides other than from top or bottom of the PDMS pieces. In order to achieve this arrangement, an on-chip fluidic connector was fabricated using a second layer SU-8 process as shown in figure 3.7.

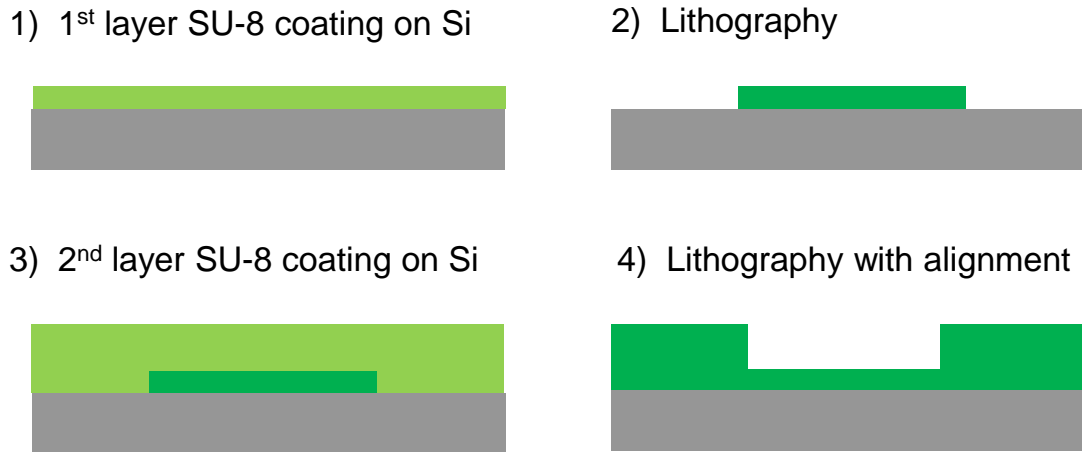


Figure 3.7: Fabrication procedures for SU-8 masters

Note the structure in step 4 of figure 3.7 can be considered as the side view of the microchannels and fluidic connectors on the wafer. It is obvious that the microchannels can be laterally accessed by capillary tubes with an outer diameter less than the height and width of the fluidic connectors. A given height of the working microchannel (blue structure in step 4 of figure 3.7) was realized by controlling the thickness of the first layer SU8 during the resist spincoat process. A wafer full of SU-8 masters fabricated this way is

shown in figure 3.8. Both single and multiple channels with single as well as multiple inlets and outlets of fluidic connectors were incorporated in the design.

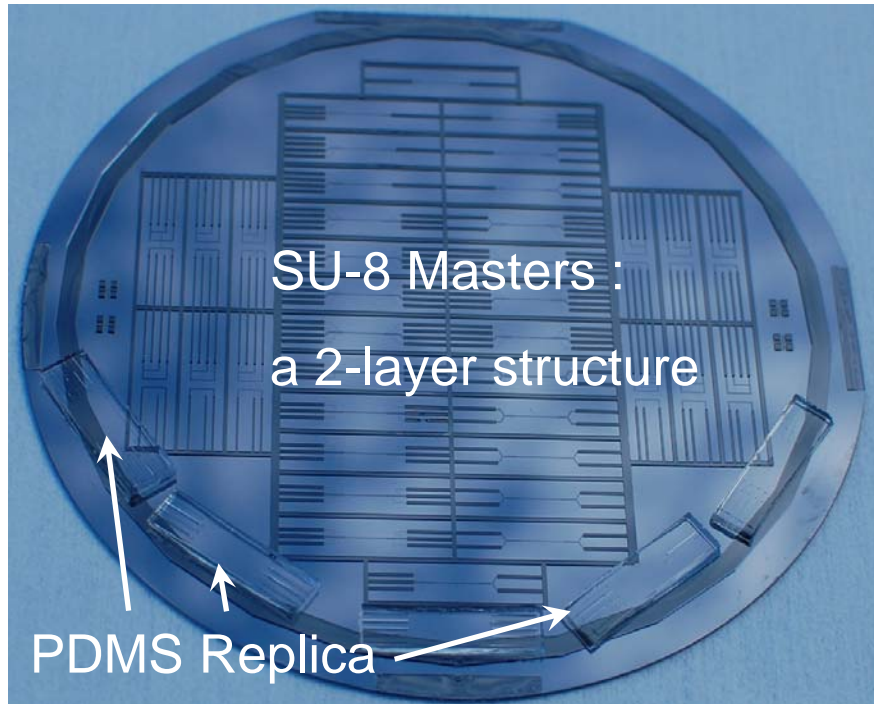


Figure 3.8: Molding of PDMS microfluidic systems using SU-8 masters

On completion of the molding process, PDMS was manually peeled off from the template and cut into individual microfluidic systems, as shown in figure 3.8. In the same time, the Si wafer with fabricated NiFe soft magnets was diced to separate the individual magnetic chips. Before assembling a PDMS microfluidic system with a magnetic chip, the chip was treated with a silanization solution containing 3-aminopropyltriethoxysilane (APTES). The silanization treatment followed a standard cleaning and reaction protocols (see details in Appendix A). This treatment prepares the magnetic chip for PEGylation, a process of covalent attachment of polyethylene glycol (PEG) polymer chains to the surface in order to minimize non-specific adhesion of the microbeads to the chip surface.

Before the actual PEGylation takes place, a PDMS microfluidic system is brought into contact with the APTES-treated chip, during which the alignment of the NiFe soft magnets on the chip with the microchannel in the PDMS piece was carried out under a microscope. With moderate pressure and heating at 80°C for 30min, a reversible but strong seal between the PDMS and the chip was achieved. Capillary tubes were inserted at both the inlets and outlets of the PDMS microchannels and sealed with epoxy to complete the device fabrication. PEGylation of the magnetic chip followed by introducing a PEG-NHS (MW: 5000) solution at pH8.0 into the microchannel and let the NHS-amine reaction proceed for 1 hr (the detailed protocol are described in Appendix A). Then the excessive PEG-NHS solution was flushed away by DI water. A typical ready-to-use device is shown in figure 3.9.

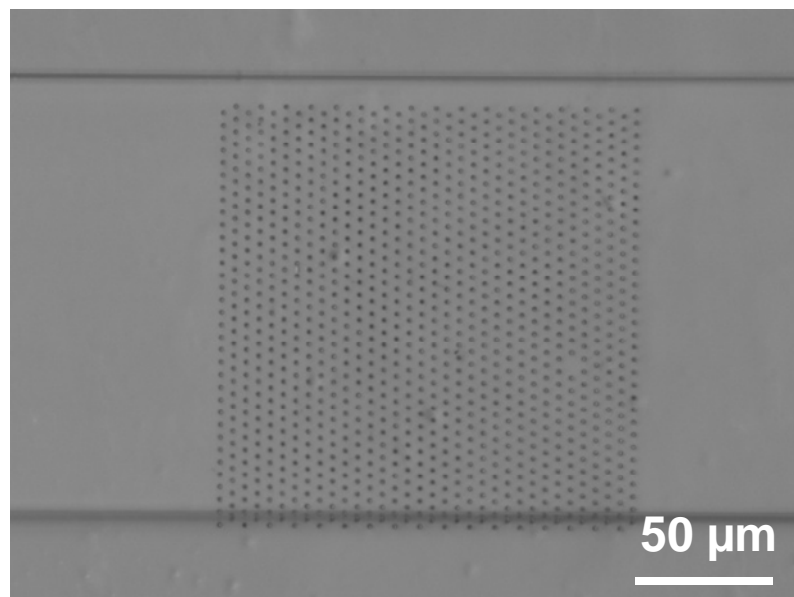


Figure 3.9: A ready-to-use magnetic chip assembled with a PDMS channel and coated with PEG on the surface

CHAPTER 4

An Immunoassay Platform Based on Magnetic Assembly of Microbeads between Microelectrode Arrays

4.1 Introduction

4.1.1 Immunoassay

An immunoassay is a biochemical test that measures the presence or concentration of a substance in solutions. It is a very specific technique based on the exceptional specificity that an antibody has for its target antigen. Such assays can be carried out for either member of an antigen/antibody pair. For antigen analytes, an antibody that specifically binds to that antigen can be prepared for use as an analytical reagent. When the analyte is a specific antibody its cognate antigen can be used as the analytical reagent.

In addition to binding specificity, the other key feature of immunoassays is the means to produce a measurable signal in response to a specific binding. Historically this was accomplished by measuring a change in some physical characteristic such as light scattering or changes in refractive index. With modern instrumentation, most immunoassays today depend on the use of detectable labels. A large variety of labels have been demonstrated including radioactive elements, enzymes, fluorescent dyes, chemiluminescent dyes, oligonucleotides, quantum dots, magnetic particles. Such labels serve for detection and quantification of binding events either after separating free and bound labeled reagents or by designing the system in such a way that a binding event effects a change in the signal produced by the label. Immunoassays in which the signal is affected by binding are referred to as homogenous immunoassays. Homogeneous method

do not separate target analyte from the solution. Immunoassays requiring a separation step, often called heterogeneous immunoassays, are popular because they are easy to design, but they frequently require multiple steps including careful washing of a surface onto which the labeled reagent has bound. In a heterogeneous immunoassay, therefore, free reagents other than the bound labeled reagent are present in excess to drive the reactions to completion, resulting in substantially better limit of detection than homogeneous assay.

Sandwich immunoassay is a type of heterogeneous immunoassay. In such an assay, a primary antibody is bound to a solid support, and a blocker protects free surface from nonspecific binding. The sample solution is added and the antigen is extracted from a sample upon binding to this antibody. Then, a labeled secondary antibody completes the immunoassay sandwich by recognizing a site on the antigen different from the primary antibody-binding site. Depending on the properties of the labels on the secondary antibody, different detection methods can be used in sandwich immunoassays.

One type of the increasingly popular immunoassays is based on electrochemical detection using enzyme labels. Unlike other labels, enzymes amplify the signal as enzymatic reaction is often catalytic and that one enzyme can produce many detectable molecules. One of the enzymes that produces electrochemically active species is β -galactosidase [134]. As shown in figure 4.1, β -galactosidase converts its substrate *p*-aminophenyl β -D-galactopyranoside (PAPG) to *p*-aminophenol (PAP), which can be oxidized to *p*-quinone imine (PQI) in a two-electron reaction at 0.28V vs. Ag/AgCl [135]. This enzymatic reaction can take place at pH = 7.4.

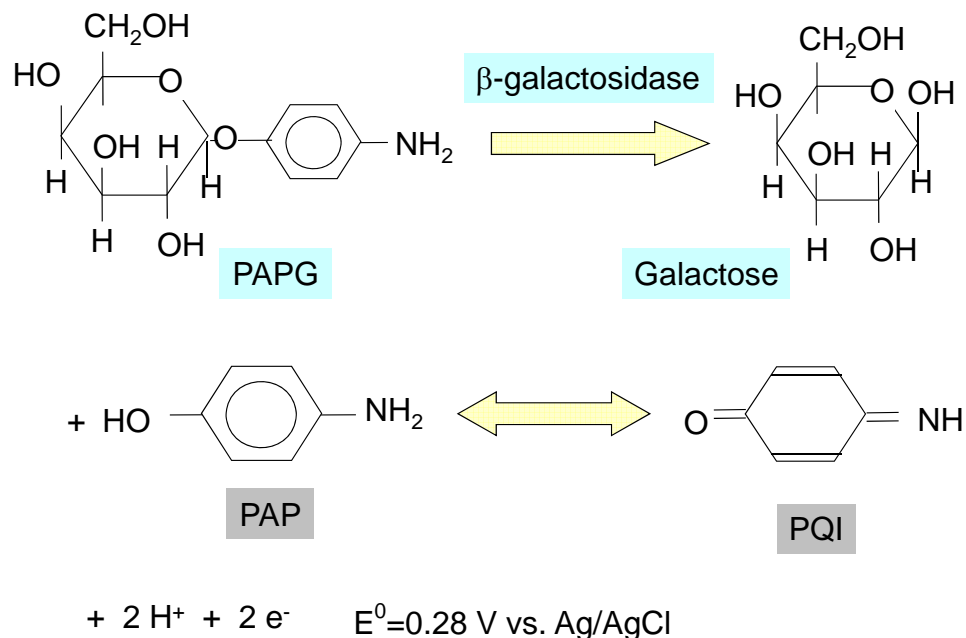


Figure 4.1: An example of electrochemical detection of enzyme labels

Immunological detection has been proved successful for infectious diseases caused by pathogenic viruses, bacteria, and aberrant proteins, as well as for bioterrorism agents including toxins and spores [136]. In the same time, improvements are needed for more sensitive and miniaturized assays. Ultrasensitive immunoassays can help the diagnosis of diseases in earlier stages than is currently possible, while miniaturization takes advantage of small volume analysis as well as portability.

4.1.2 Interdigitated Array (IDA) Electrodes

Interdigitated array electrodes have played an important role in electrochemical sensing of redox species. Due to their special geometry and the operation with two sets of working electrodes (figure 4.2), IDAs yield a much higher current for reversible redox reactions than a conventional single working electrode under the same condition.

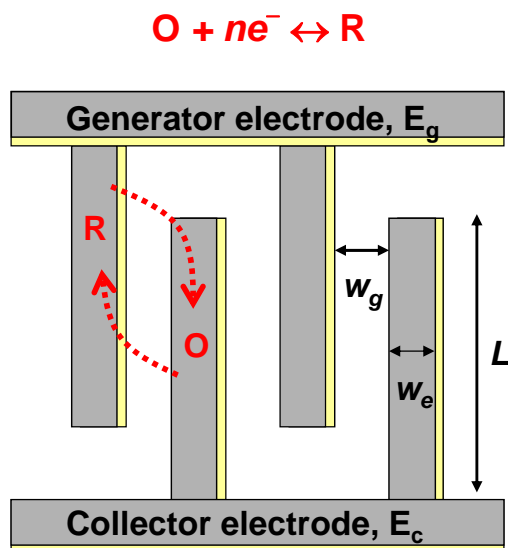


Figure 4.2: Sketch of interdigitated array electrodes with redox cycling indicated

With the IDA setup, a reduced/oxidized form of the redox couples generated at one set of electrodes (generator) diffuses to and is collected at adjacent electrodes (collector). Once the collected species is electrolyzed at the collectors, the oxidized/reduced form diffuses back to the generator, leading to more generation of the reduced/oxidized form, and the process continues on. This unique feature of IDAs is referred to as redox cycling, which amplifies the currents at both the generator and the collector [137]. The diffusion-controlled limiting current of IDAs is given by [138]:

$$I_{lim} = nmLFDC^* \left\{ 0.637 \ln \left[2.25 \left(1 + w_e/w_g \right) \right] - \frac{0.19}{\left(1 + w_e/w_g \right)^2} \right\} \quad (4.1)$$

where L , w_e and w_g are the length, the width of and spacing between the electrodes, respectively, m the number of electrode pairs, n the number of electrons, D the diffusion coefficient, F the Faraday's constant, and C^* the concentration of the redox species.

Both theoretical studies [139] and experiments [140] have shown that steady-state currents can be easily obtained and redox cycling is more efficient due to the enhanced

mass transfer via radial diffusion at smaller IDAs. However, the diffusion-limited current of IDAs depends on the ratio of the width of the electrode to the spacing between the electrodes instead of the absolute value of the electrode size and spacing (equation 4.1). Therefore, the pursuit of higher sensitivity of IDAs through further decreasing the critical dimensions of electrodes which are already less than the thickness of the diffusion layer may not justify the effort.

An alternative way of amplifying the signal from IDAs is to preconcentrate the redox species in the proximity to the electrodes instead of allowing them to disperse in the whole electrochemical cell. Many electrochemical biosensors achieve the local confinement of analyte through immobilization of biomolecules, such as enzymes, onto the electrode surface [141]. In this situation, electrochemically active species that are produced when the enzymes are exposed to their substrates are in very close proximity to the electrodes and can be effectively sensed before they diffuse into a bulk solution. One of the drawbacks in this approach is that the immobilized biomolecules block some active electrode surface and limit the electron transfer process.

Another approach to concentrating the analyte at the sensing region is to immobilize biomolecules onto micro/nano bead surfaces and then transport the beads to the sensing electrodes [24]. Many types of micro/nano beads have been developed with specific surface chemistries targeted to various biomolecule binding and are commercially available. However, the assembly of beads in the electrode sensing region with optimal sample preconcentration and maximum sensor response requires careful design and integration of bead-handling elements with the electrodes on a microfluidic chip.

4.1.3 Magnetic Bead-based Immunoassay with IDA Detection

As discussed previously, redox cycling on IDAs enhances current in electroanalysis, while enzyme reaction is a very effective signal enhancement in biological systems. Therefore, a heterogeneous immunoassay that couples these two signal amplification means would be desirable. The redox cycling and enzyme reaction can be coupled if the enzyme label on the target analyte converts electrochemically inactive substrates into reversible redox species, e.g., *p*-aminophenol converted by β -galactosidase because its oxidized form *p*-quinone imine can be reduced back to *p*-aminophenol at -0.3V vs. Ag/AgCl [135].

Meanwhile, microbead-based immunoassay offers an improved binding capacity of the target analyte due to an increased surface area per unit volume. Therefore, IDA-based electrochemical immunoassay utilizing enzyme label immobilized to the surface of microbeads can benefit from another degree of the signal amplification. In addition, bead-based format provides the flexibility of manipulating the target analyte using the properties of the microbeads. For example, if the beads are magnetic, magnetic field can be used to manipulate them for improved assay performance [142]. In this work, we study the magnetic assembly of microbeads between IDAs to enhance the sensitivity and lower the limit of detection of an enzymatic immunoassay. The schematic of our magnetic bead-based immunoassay using IDAs for the detection of enzyme labels is shown in figure 4.3. Due to the high binding capacity and low sedimentation rate, Dynabeads® MyOne (1 μ m in diameter) from Invitrogen (Carlsbad, CA) was chosen in this study.

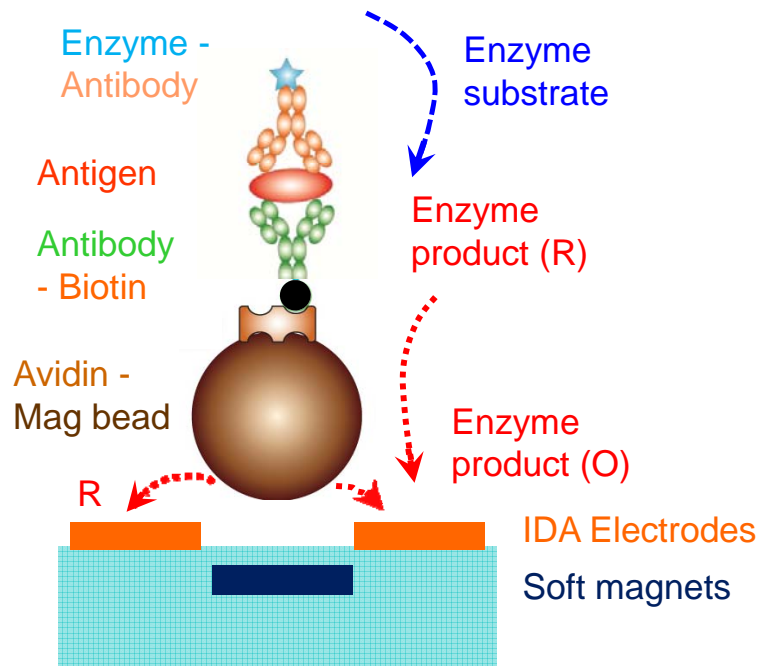


Figure 4.3: Schematic of magnetic bead-based immunoassay using IDAs for enzyme-label detection

4.2 Theoretical Study of Magnetic Assembly of Individual Microbeads

There are many ways to apply magnetic forces to nearby magnetic microbeads. The most intuitive and effective method is to fabricate small soft magnets (i.e., iron, nickel, cobalt, and their alloys) on the substrate and then subject them to an external magnetic field. The external magnetic field can cause the alignment and growth of magnetic domains in the soft magnets, giving a large multiplication of the applied field. The induced field of the soft magnets superimposed on the uniform external field results in strong field gradients around the soft magnets, generating attractive magnetic force on nearby magnetic beads.

4.2.1 Magnetic Field of Rectangular Soft Magnets

A common geometry of soft magnets is the rectangular type as sketched in figure 4.4 with reference frames.

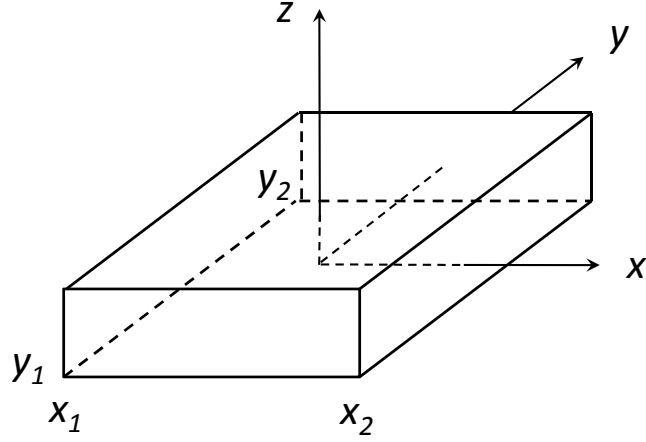


Figure 4.4: Sketch of a rectangular soft magnet

The analytical solution to the three components of the magnetic field of such a soft magnet with a saturated magnetization, M_s , in z direction are given by [143]:

$$B_x(x, y, z) = \frac{\mu_0 M_s}{4\pi} \sum_{k=1}^2 \sum_{m=1}^2 (-1)^{(k+m)} \ln[F(x, y, z, x_m, y_1, y_2, z_k)] \quad (4.2)$$

$$B_y(x, y, z) = \frac{\mu_0 M_s}{4\pi} \sum_{k=1}^2 \sum_{m=1}^2 (-1)^{(k+m)} \ln[H(x, y, z, x_1, x_2, y_m, z_k)] \quad (4.3)$$

$$B_z(x, y, z) = \frac{\mu_0 M_s}{4\pi} \sum_{k=1}^2 \sum_{n=1}^2 \sum_{m=1}^2 (-1)^{(k+n+m)} \times \tan^{-1} \left[\frac{(x-x_n)(y-y_m)}{(z-z_k)} g(x, y, z; x_n, y_m, z_k) \right] \quad (4.4)$$

where

$$F(x, y, z, x_m, y_1, y_2, z_k) = \frac{(y-y_1) + \left[(x-x_m)^2 + (y-y_1)^2 + (z-z_k)^2 \right]^{1/2}}{(y-y_2) + \left[(x-x_m)^2 + (y-y_2)^2 + (z-z_k)^2 \right]^{1/2}}$$

$$H(x, y, z, x_1, x_2, y_m, z_k) = \frac{(x-x_1) + \left[(x-x_1)^2 + (y-y_m)^2 + (z-z_k)^2 \right]^{1/2}}{(x-x_2) + \left[(x-x_2)^2 + (y-y_m)^2 + (z-z_k)^2 \right]^{1/2}}$$

$$g(x, y, z; x_n, y_m, z_k) = \frac{1}{\left[(x-x_n)^2 + (y-y_m)^2 + (z-z_k)^2 \right]^{1/2}}$$

In the case of in-plane magnetization in the x-y plane of the soft magnet, equations (4.2-4.4) can be easily modified by a simple coordinate rotation to obtain the corresponding magnetic field components.

The above equations can be used to obtain the field of a single soft magnet of given dimensions, and the field of multiple magnets in an array can be obtained by superimposing the individual fields according to the geometrical layout of them. The total field is then biased with the external bias field applied for magnetizing the soft magnets. Once the magnetic field is known, the magnetic force on a magnetic microbead at a point in space can be calculated using equation (2.9). If the external field strength is beyond the saturation field of the microbead ($\sim 0.15\text{T}$ for Dyanbeads MyOne from manufacturer's data), equation (2.9a) is used.

4.2.2 Magnetic Force for Separating Individual Microbeads from Flow

From equations 2.9 and 2.9a, one notes magnetic force on a microbead depends strongly on the magnitude and the gradient of the magnetic field. Thus, the design of magnet fields for capture of magnetic beads from a flow of bead suspension and assemble them on the surface of a microchannel includes the dimensions of the soft magnets, the spacing between them in an array, the array size, and the consideration for typical flow conditions. We intended to assemble and manipulate individual MyOne beads on a chip; therefore, soft magnets in size comparable to the size of the beads were considered. Although magnetic field gradient scales favorably with the miniaturization of the soft magnets subjected to an external field, it has a shorter reach into the spatial region with smaller soft magnets. With parametric studies using numerical simulation based on the analytical models described previously, we studied the magnitude of magnetic force on a

bead and the acting distance of the magnetic force inside the fluid. Both normal magnetization and in-plane magnetization of the soft magnets were studied. We assume the external permanent magnet can provide a uniform field sufficient to saturate both the soft magnets and the microbeads. The saturation flux density of the soft magnet based on NiFe alloy is assumed to be 660kA/m, while the saturated magnetic moment is 40kA/m for MyOne beads from the manufacturer's data. The magnetic force was calculated by treating the magnetic bead as a dipole point at its mass center. Matlab was used to write the numerical code for magnetic force calculation.

Figure 4.5 shows the magnetic capturing force (F_z) on a MyOne bead as a function of the distance away from the surface of an array of 1 μ m square NiFe magnets. The thickness of the NiFe magnet is 0.15 μ m. It illustrates that magnetic capturing force exceeding 1nN can be generated when the bead is in contact to the device surface (note $z = 0.5\mu$ m is at the mass center of the bead). However, if the bead is 4 μ m away from the surface, the capturing force dramatically decreases to less than 0.1pN, which can only generate a 10 μ m/sec downward speed of the bead suspended in water (see discussion in chapter 2 section 2.3). Figure 4.5 also compares the magnetic capturing force between normal and in-plane magnetizations of the soft magnets by the external field. It shows that normal magnetization produces a larger force, and the force extends farther into the fluid. This analysis leads us to arrange the external magnet so that it provides normal magnetization of the soft magnets for bead capturing in actual experiment. At the same time, in-plane magnetization may have the advantage over other types of bead manipulation. A detailed discussion on this subject will appear in chapter 5.

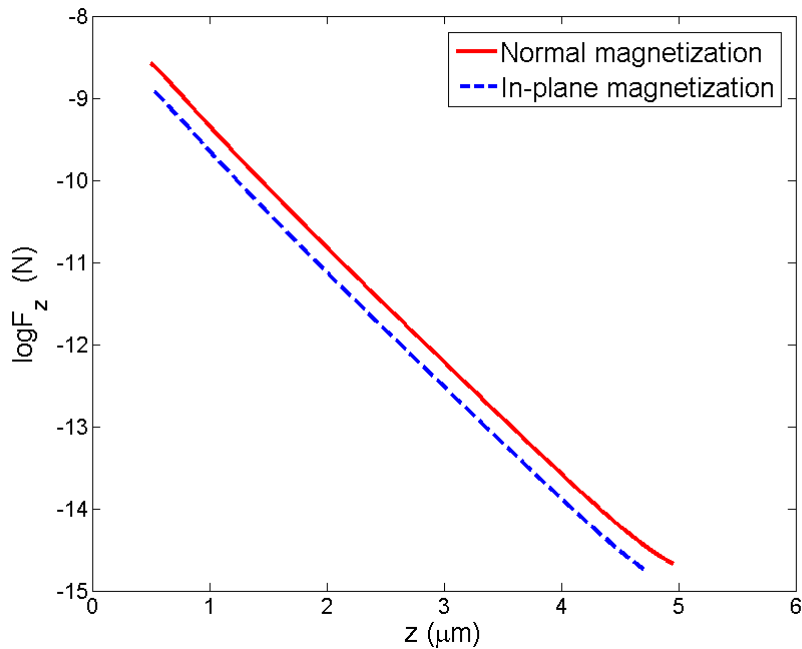


Figure 4.5: Magnetic force (F_z) on a MyOne bead as a function of the distance away from the surface of the soft magnets
(Dimensions of the soft magnets: $1\mu\text{m}$ wide, $1\mu\text{m}$ long, $0.15\mu\text{m}$ thick;
Spacing between neighboring magnets: $1\mu\text{m}$ in both directions;
Number of the soft magnets in a square array: 75×75)

The effect of the aspect ratio of the soft magnets on the capturing force under normal magnetization is illustrated in figure 4.6. The result implies that increasing the thickness of the soft magnets from $0.15\mu\text{m}$ to $0.6\mu\text{m}$ increases both the magnitude and the acting distance of the capturing force. In comparison, increasing the lateral dimension of the soft magnets from $1\times 1\mu\text{m}$ to $1\times 2\mu\text{m}$ increases the reach of the capturing force much farther, although the magnitude of the force close to the surface slightly drops. The effect of array density of the soft magnets is presented in figure 4.7. It indicates that the reach of the capturing force increase with decreasing density of the soft magnets, while the holding force for beads attracted to the surface of the soft magnets is about the same.

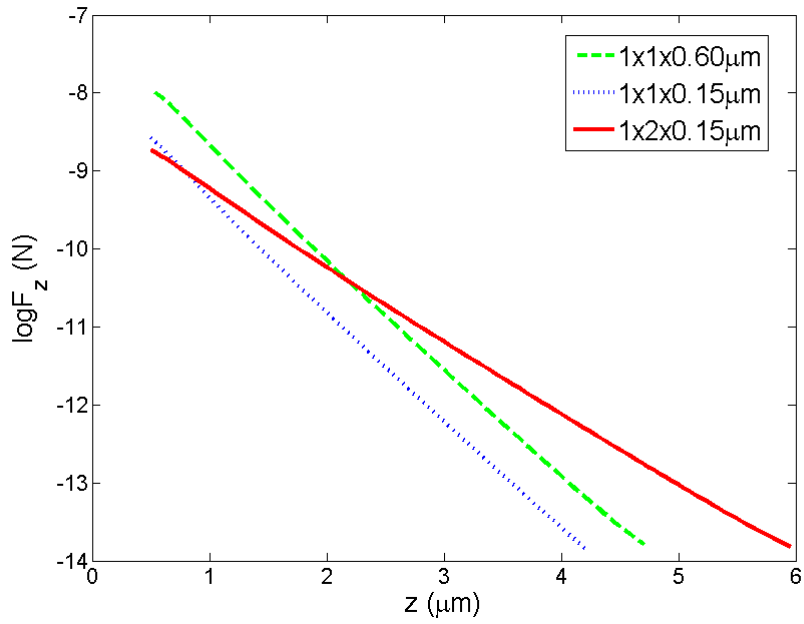


Figure 4.6: Magnetic force (F_z) as a function of the aspect ratio of the soft magnets (Spacing between neighboring magnets: $1\mu\text{m}$ in both x and y directions; Number of the soft magnets in a square array: 75×75)

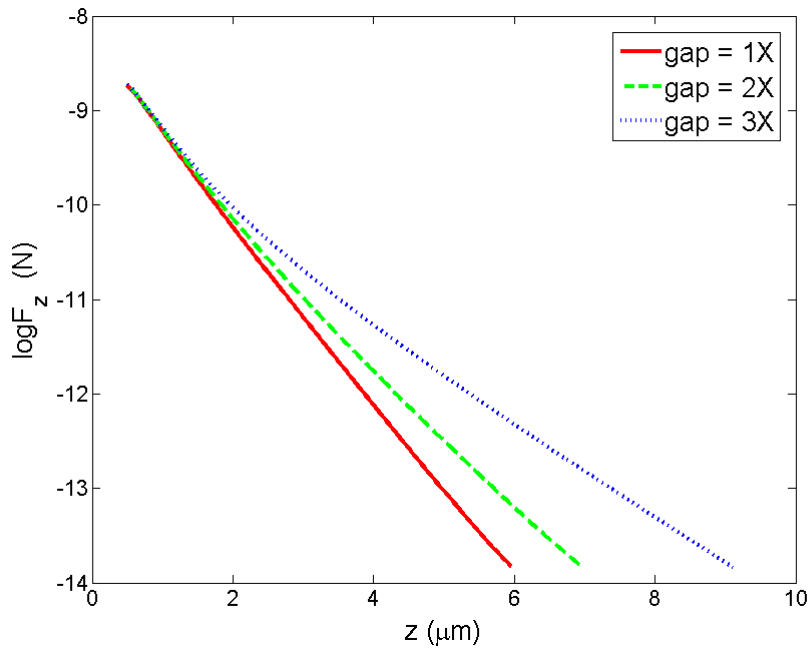


Figure 4.7: Magnetic force (F_z) as a function of the array density of the soft magnets

All the above results imply that the distance over which the magnetic force is greater than 0.1pN is less than 10 μ m when the soft magnets are comparable in size to the MyOne beads, due to the limited extent of magnetic field gradient. Therefore, the height of the microfluid system for bead delivery should be within this range for high capture efficiency.

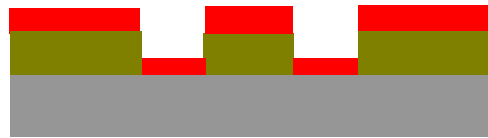
4.3 Fabrication of Integrated MAP-IDA Devices

The fabrication procedure that was used to integrate NiFe patterns with IDAs is shown in figure 4.8.

1. Lithography



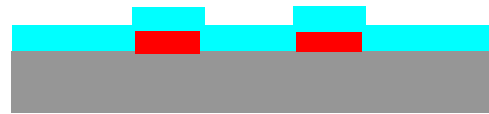
2. NiFe evaporation



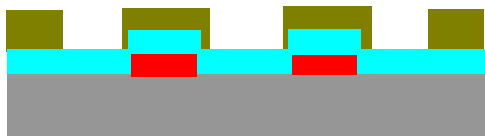
3. Lift-off



4. Low temperature SiO₂ dep



5. 2nd lithography



6. Pt evaporation and Lift-off

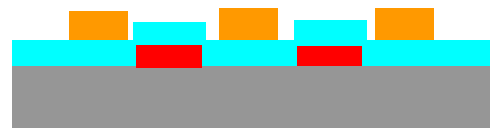


Figure 4.8: The fabrication procedure for integrating NiFe magnets with IDAs

In order to prevent exposure of NiFe to electrical potential and liquid environment during the experiment, both of which will lead to the corrosion of NiFe, an insulation layer between the electrodes and the NiFe patterns is necessary. Consequently, a

multilayered lithography process had to be performed. To fabricate the IDAs and NiFe magnets in submicron scales with high alignment accuracy, the JOEL JBX-9300FS electron-beam lithography system was employed. Although electroplating is the most common microfabrication technique for NiFe alloy, e-beam evaporation of Ni₈₀Fe₂₀ pellets was used in this work since a thin layer of NiFe magnets, i.e., 150nm, can produce sufficient magnetic force for bead capturing purposes (see figures 4.5-4.7). The SiO₂ insulation layer was deposited by an electron cyclotron resonance (ECR) tool with a low processing temperature, as conventional CVD processes would oxidize NiFe and result in loss of magnetic properties.

Figure 4.9 shows three fabricated devices with integrated NiFe soft magnets among Pt IDA electrodes. The thicknesses of the NiFe and the Pt patterns are 0.15 μ m and 0.1 μ m, respectively. The SiO₂ insulation layer between the magnets and IDAs is 0.2 μ m thick. Both the generator and collector electrodes were 0.8 μ m in width and the gap between the neighboring electrodes is 1.6 μ m. In figure 4.9a, 0.8 \times 0.8 μ m square magnets with 0.8 μ m spacing along the electrodes and 1.6 μ m spacing across the electrodes were integrated between the IDAs. In figure 4.9b, 0.8 \times 1.6 μ m rectangular magnets with the same spacing as the square magnets were integrated. The excellent alignment capability of the JBX-9300FS eBeam lithography system leads to no observable misalignment between the soft magnets and IDAs at two different layers of the devices. The same fabrication procedure allows that the NiFe magnets to be placed beneath the IDA electrodes, so that the spacing between the neighboring electrodes can be further decreased. With this design, more pairs of IDA electrodes and a denser distribution of the NiFe magnets can be laid out in the same footprint, as shown in figure 4.9c.

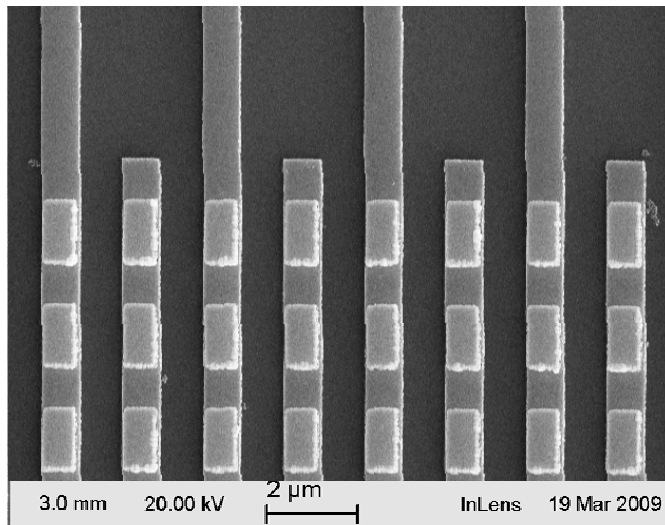
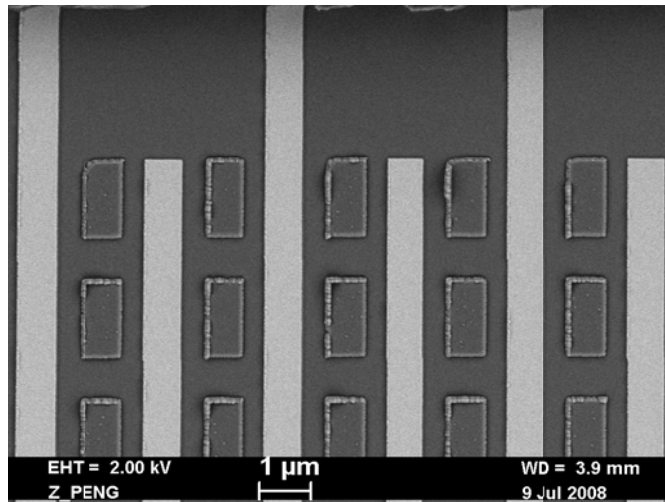
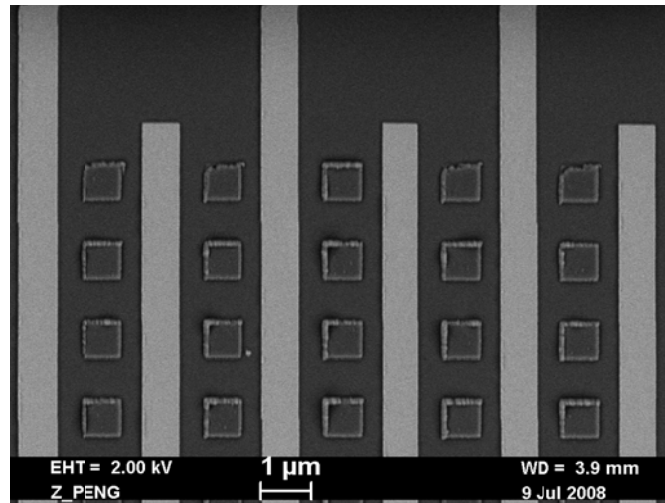
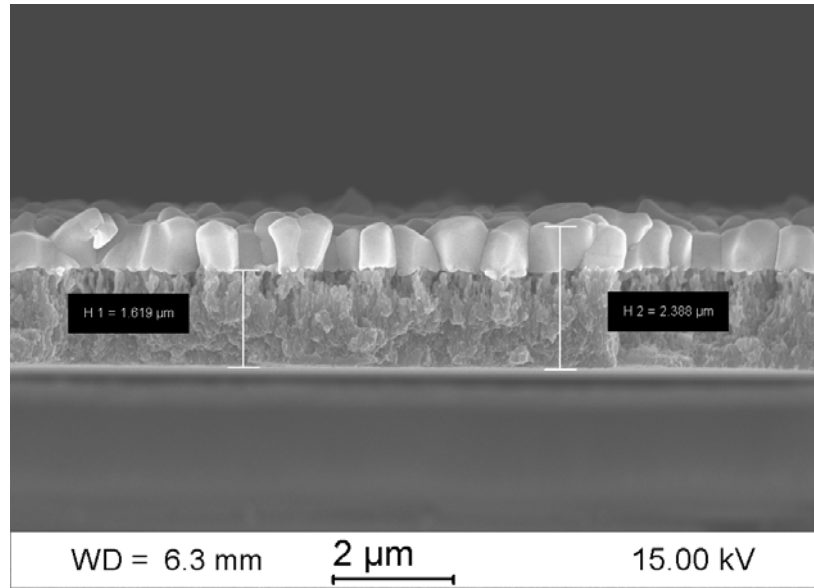
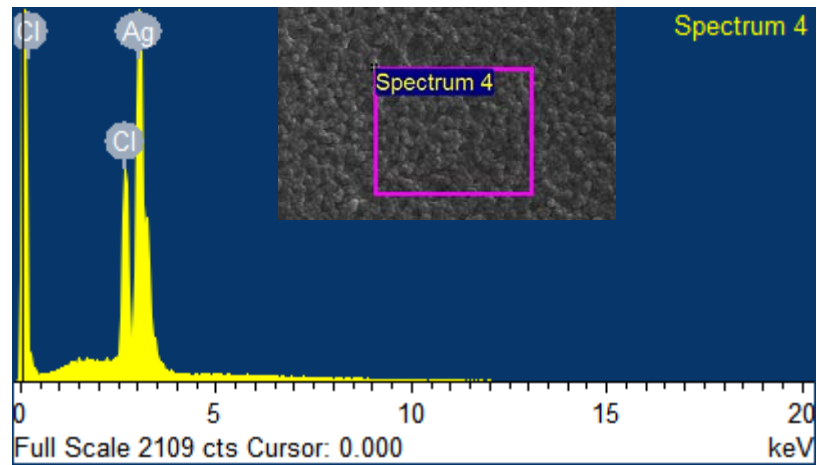


Figure 4.9: Fabricated devices with integrated NiFe magnets (grey rectangles) among Pt IDA electrodes (shiny bands)

Other components of the electrochemical sensing device such as Pt auxiliary electrodes, the seed layer for Ag/AgCl pseudo reference electrodes, and Au contact pads were patterned on the same chip by photolithography and metalized by evaporation, followed by lift-off techniques in sequence. With a photoresist mold aligned to the seed layer, Ag electrodes were electroplated using a cyanide-free solution from Technic Inc (Cranston, RI) called Silver Cycles®. It is a basic solution with pH = ~11. A constant current at $5\text{mA}/\text{cm}^2$ was used for the plating and plating rate was about $0.25\mu\text{m}/\text{min}$. After the electroplated Ag layer reached $\sim 2\mu\text{m}$, i.e., 8 min, a reverse electroplating in 1M KCl solution was performed for 2 min to partially convert the Ag to AgCl. As a result, a solid-state Ag/AgCl electrode was formed on the chip. The cross-section of the Ag/AgCl electrode fabricated in this way is shown in figure 4.10. The energy-dispersive X-ray spectroscopy (EDX) inspection of electrodes indicates that the composition ratio between Ag and Cl is about 6:4. We tested the electrochemical potential of the solid-state Ag/AgCl electrodes using Zobell's Solution. The oxidation-reduction potential (ORP) of a clean Pt electrode measured $\sim 110\text{mV}$ with respect to the Ag/AgCl electrodes and the ORP was stable during the time period of measurement, i.e., 30min. Therefore, this fabricated Ag/AgCl electrode can serve as a pseudo reference electrode to replace the conventional Ag/AgCl reference electrode with a liquid junction, which is bulky and cannot be integrated inside a microchannel.



a)



Element	App Conc.	Intensity Corrn.	Weight%	Weight% Sigma	Atomic%
Cl K	5.34	1.0729	15.68	0.33	36.13
Ag L	24.62	0.9192	84.32	0.33	63.87
Totals			100.00		

b)

Figure 4.10: Fabrication result of a solid-state Ag/AgCl electrode
 a) Cross-section view; b) EDX inspection

Figure 4.11 shows a device on completion of the wafer processes. The IDAs in this device consists of 40 pairs of interdigitated electrodes. The length upon which the generator and collector electrodes are paired is $120\mu\text{m}$. Among the center 30 pairs of the electrodes, an array of square NiFe magnets are uniformly distributed between the neighboring electrodes (see figure 4.9a), and the total number of the magnets is $75 \times 60 = 4500$.

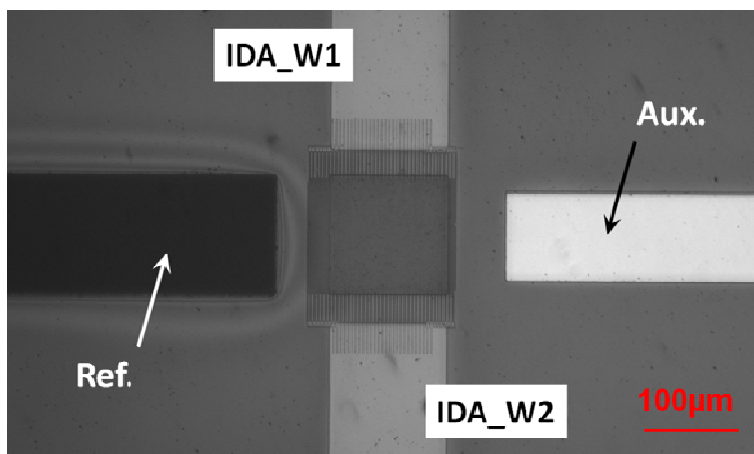


Figure 4.11: An integrated device on completion of the wafer processes

After cutting the wafer into individual dies, PDMS microfluidic channels of $150\mu\text{m}$ wide and $8\mu\text{m}$ high were assembled with the dies. The design of the shallow channel was based on the theoretical calculations for high efficiency of bead capture (see section 4.3). All the electrodes on a sensor die were contained in a single microchannel. Finally, the devices were wire-bonded to a microcircuit packages purchased from AEGIS Inc (New Bedford, MA). A completed device sitting on a rare-earth magnet, purchased from Magcraft® with its magnetic poles on the top and bottom surfaces, and connected to both a syringe pump through capillary tubes and an electrochemical instrument via electronic leads is shown in figure 4.12.

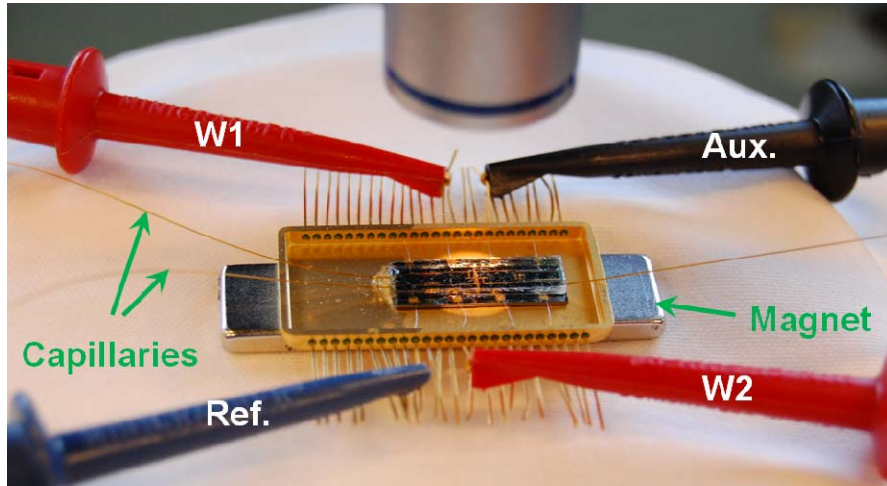


Figure 4.12: Final device in experimental setup

4.4 Experimental Results and Discussion

4.4.1 Magnetic Assembly of MyOne Beads between IDA Electrodes

Before each experiment, Dyanbeads MyOne ($1\mu\text{m}$) from Invitrogen (Carlsbad, CA) were washed by 1X PBS buffer (pH7.4) and incubated with 0.5% bovine serum albumin (BSA) in PBS for 30min, followed by re-suspending them into DI water with 0.05% Tween-20™ to avoid aggregation during the use. The PBS buffer and Tween-20 were from Fisher Scientific (Fair Lawn, NJ), and BSA was from Boehringer–Mannheim (Indianapolis, IN). Different concentrations of beads were prepared ranging from the original concentration of the stock solution ($0.7\text{-}1.2\times 10^{10}$ beads/ml) to 1/100 of the original concentration. A programmable syringe pump from Harvard Apparatus (Model HA2000W) capable of simultaneously controlling two syringes was used to deliver the bead suspension and analyte into the microchannel. An inverted microscope (Nikon Eclipse TE2000) equipped with a CCD camera (Photometrics CoolSNAP HQ2) was used to monitor the bead capturing and assembly process through the optically transparent PDMS microchannel.

During the experiment, the device sat on top of a neodymium-iron-boron rare earth magnet that provides $\sim 0.2\text{T}$ flux density normal to the surface of the device. This field strength is sufficient to saturate the MyOne beads. By connecting the device with a bead suspension-loaded syringe using a capillary tube, we delivered the microbeads to the device with a given velocity adjustable via the flow rate setting in the syringe pump. We observed that the small NiFe magnets could capture the beads from the flow up to a 5mm/sec , beyond which the beads would travel by the NiFe structured region. A typical experimental result is shown in figure 4.13, which provides clear evidence of effective capture of the beads onto the chip surface. The fact that beads didn't land outside of the magnetic area, including the electrode-structured area, suggests that the trapping of beads is solely due to magnetophoresis (MAP) and not due to physical barriers.

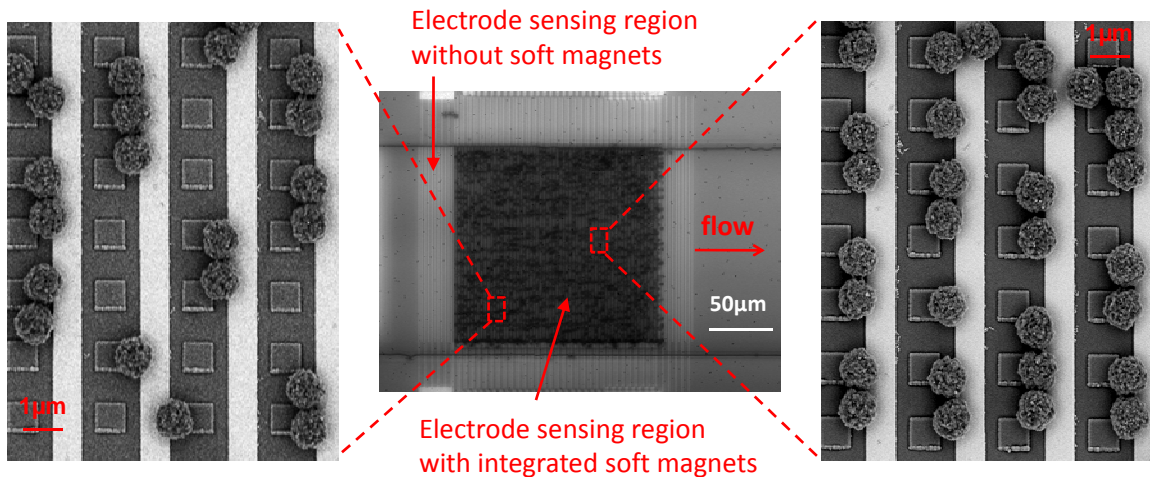


Figure 4.13: A typical result of magnetic assembly of MyOne beads between the IDA electrodes

The device shown in figure 4.13 contains 4500 NiFe magnets on the device and ~ 3500 beads were captured and assembled in the sensing region. We observed that the concentration of the suspension and distribution of the beads in the flow significantly

affects the population of the beads on the soft magnets. The flowing beads mostly focus in the center of the channel at low concentrations and only distribute to the outer area at high concentrations. Since the soft magnets were distributed across the bottom surface of the channel, relatively high concentration of the bead suspension was necessary to achieve uniform bead assembly in the sensing region. The different percentage of bead population among the NiFe pads at the center area of the channel and that close to the channel wall is illustrated by the SEM images.

In real time, we observed that the beads were captured on top of the NiFe magnets without observable influence by the direction of the flow, which verifies the theoretical calculation that the magnetic force on the beads when they are close to the magnet surface is strong relative to the drag force (see figures 4.5-4.7). This result is desirable in IDA electrode sensing because beads landing on top of the electrodes will block some active electrode surface and limit the electron transfer process. For SEM imaging purpose, we dried the aqueous solution and removed the PDMS microchannel while remaining the external magnet in place. We noticed that the beads moved away from the top surface of the magnets to the edge or the gap between two adjacent magnets, as shown in SEM image of figure 4.13, which indicates the surface tension on the beads during the water drying process was even stronger than the magnetic force. Also noticed is that the dense distribution of the soft magnets tends to encourage bead-bead interaction with closest neighboring beads attract each other once they were shifted away from the centers of the soft magnets.

The SEM image in figure 4.13 also indicates that most NiFe magnets captured only one bead, due to the comparable size between the magnets and the beads. Therefore,

these magnets can be used to assemble individual beads with designated separation distance on a surface. The separation distance between the beads can be adjusted with different array density of the NiFe magnets included at the design stage. As shown in figure 4.14, an assembly of beads with equal separation distance ($\sim 2.4\mu\text{m}$) uniformly distributed along and across the electrodes was realized. This uniform distribution of beads would allow each bead to equally contribute to the electrochemical signal at the IDA electrodes, provided the same amount of active enzyme label is associated with each bead.

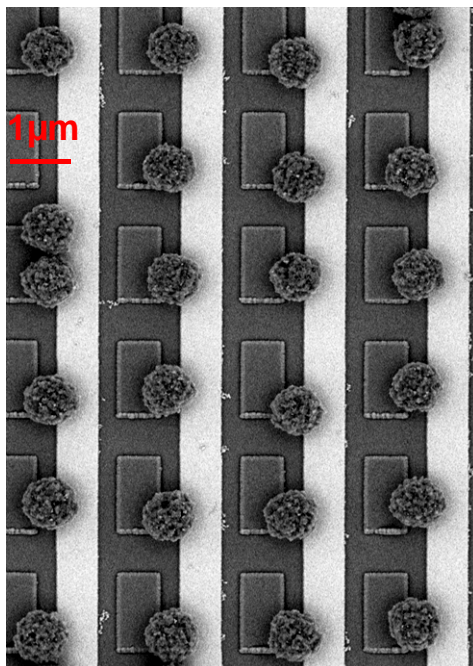


Figure 4.14: Uniform distribution of microbeads with equal separation distance ($\sim 2.4\mu\text{m}$) along and across the electrodes

The capability of controlling bead distribution on a surface is useful for many types of bead-based bioanalysis in lab-on-a-chip systems. In the discussion to follow, we explore its application in electrochemical immunoassay with controllable sample

distribution and pre-concentration by uniformly assembling different number of beads at identical IDA electrode regions.4.4.2 Electrochemical Detection of Enzymes Immobilized on Bead Surface

The integrated MAP-IDA device described here offers an ideal platform for magnetic bead-based biosensing, provided target biomolecules are immobilized on the bead surfaces and labeled with enzymes such as β -galactosidase that produce redox species. The device can bring the biomolecules in close proximity to the electrode sensing region without blocking the active electrode surface. In addition, the distribution and the level of pre-concentration of the target analyte can be controlled via the tunable magnetic assembly of the microbeads.

For device characterization purpose, we directly immobilized β -galactosidase onto the MyOne beads without going through the complete protocol of sandwich immunoassay that involves multiple steps of antibody-antigen interaction, which may complicate the binding efficiency of β -galactosidase onto the bead surface. MyOne beads with recombinant streptavidin covalently and uniformly grafted to the bead surface from Invitrogen (Carlsbad, CA) and biotinylated β -galactosidase from Sigma–Aldrich (St. Louis, MO) were used in the experiment. Following the protocol described in Kim et al. [10] for the direct binding of the biotinylated β -galactosidase to the streptavidin-coated MyOne beads, the binding reaction can be so well controlled that it yields similar number of enzyme molecules on individual beads. The schematic of the resultant bead-enzyme complex is shown in figure 4.15. According to the manufacturer, the binding capacity for biotinylated immunoglobulin (230 kDa) on streptavidin-MyOne beads is 11–12 μ g/mg [125]. β -galactosidase has about half of molecular weight (116 kDa) as immunoglobulin,

thus we can assume a binding capacity about $6\mu\text{g}/\text{mg}$. The prepared beads were re-suspended into 1X PBS buffer with 0.1% Tween-20™ to avoid aggregation during the experiment.

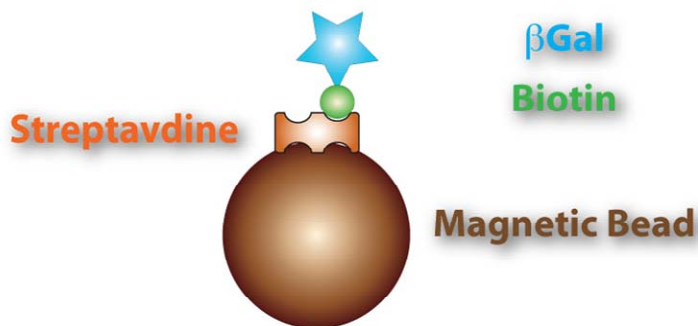


Figure 4.15: Schematic for direct immobilization of enzyme onto the magnetic beads

Before injecting the β -galactosidase modified MyOne beads into a typical device as shown in figure 4.12, the IDA electrodes of the device were cleaned by flowing an EDTA solution into the microchannel and tested with cyclic voltammogram (CV) on ferri/ferrocynide redox couple. An electrochemical analyzer with bipotentiostats from CH Instruments, Inc. (Model CHI832A) was used to apply potentials to the IDAs along with the Pt auxiliary and Ag/AgCl reference contained in the same microchannel. When the individual set of electrodes from IDAs was utilized as single working electrodes in a three electrode system, the classic duck-shaped CV curve was observed and the peak potential separation of $\sim 60\text{mV}$ was verified at several scan rates. With both sets of IDA electrodes connected as working electrodes, a well-defined *sigmoidal* response was observed and the diffusion-limited current was 2-3 folds of the peak current from the single working electrode setup using the same IDA electrodes. The collection efficiency of the redox cycling of the ferri/ferrocynide couple on the IDAs was about 90-95%.

Once the IDA electrodes were proven ready to use, β -galactosidase modified beads were delivered to the microchannel and magnetic assembled between the IDA sensing region. The device used and the bead-assembly result is similar to figure 4.13 and the total number of beads assembled in the IDA region was found to be about 3,000. Then the enzyme substrate, *p*-aminophenyl β -D-galactopyranoside (PAPG), also purchased from Sigma–Aldrich (St. Louis, MO), was injected to the microchannel without disturbing the assembled beads. A relatively high concentration of PAPG solution, 4mM, was used to achieve the maximum rate of *p*-aminophenol (PAP) generation. Once the PAPG solution reached the sensing region, the flow was stopped. Amperometric technique was employed to detect the oxidation of the PAP molecules once they diffuse from the bead surface to the IDAs and form *p*-quinone imine (PQI) at the generator electrodes, as well as monitor the redox cycling between the generator and collector.

Figure 4.16 shows a typical current-time response of the redox reaction with the potentials at the generators and the collectors of the IDAs held at +0.30V and -0.30V vs. Ag/AgCl, respectively. The result indicates that the currents at both the generator and the collector started to increase 90sec after the injected PAPG reached the assembled beads. During the initial stage of the measurement the increase of current was slow, which may be attributed to a possible situation that the flow of PAPG was not completely stopped and that the diffusion of the enzyme product PAP towards the electrodes was affected by the flow convection. However, after about another 90sec the current rose rapidly with a rate of 15pA/sec until a plateau was reached. Figure 4.16 also reveals that the signals

obtained from the generator and the collector were nearly symmetric, implying a high electrochemical reversibility of the PAP/PQI redox couple.

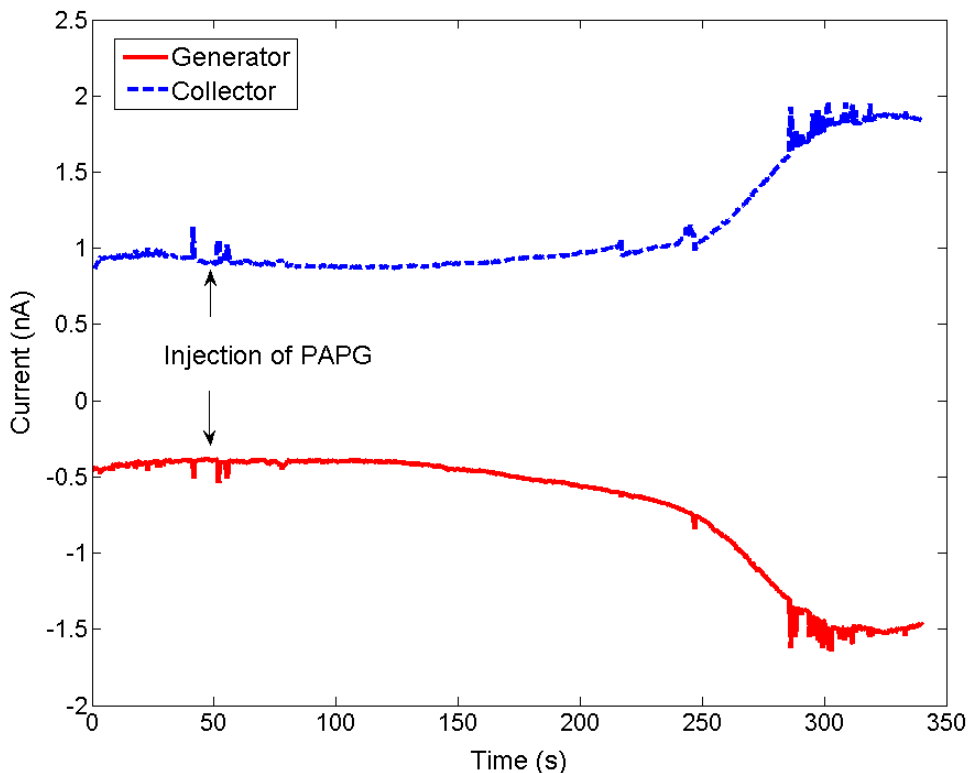


Figure 4.16: The amperometric responses of a 40-pair IDAs to the injection of the PAPG to 3,000 β -galactosidase modified MyOne beads

As discussed in section 4.5.1, because of the capability of our device for assembling individual beads, the number density of the beads on identical IDAs can be controlled by the varying the array density of NiFe magnets. Therefore, we could conveniently investigate the electrochemical response as a function of the number of the beads and their distribution. Assuming individual beads are saturated with similar number of enzyme molecules, the number and distribution of the beads determine the amount and level of pre-concentration of the enzyme in the IDA sensing region. For comparative studies with both positive and negative controls, three identical IDAs (30 pairs) were

fabricated on the same chip and integrated with different numbers of $0.8 \times 1.6 \mu\text{m}$ rectangular NiFe magnets uniformly distributed among the IDAs. The numbers are 0, 1400, and 2000 for reference sensor, active sensor 1 and 2, respectively, among the center 20 pairs of the IDAs. A multichannel electrochemical analyzer from CH Instruments, Inc. (Model CHI1000) was used to simultaneously measure the signals from the three IDAs sharing the same reference and auxiliary electrodes fabricated on the same chip and contained inside the same microchannel.

With slightly different bead-populating yields, active sensor #1 assembled ~ 900 beads with an average bead-separation distance of $3.2 \mu\text{m}$ and $2.4 \mu\text{m}$ along and across the electrodes, respectively, while active sensor #2 assembled ~ 1500 beads with an average separation distance of $2.4 \mu\text{m}$ in both directions. The higher number density of beads on sensor 2 was achieved mainly because of the denser layout of the NiFe magnets. Figure 4.17 presents the amperometric responses of the three sensors including the reference sensor on which no beads were assembled due to the absence of the soft magnets. Note only the signals from the generators are shown, the signals from the collectors were symmetric and similar in trend. The results indicate that the response time for the two active sensors with different number of beads in presence was about 100sec for 900 beads and 50 sec for 1500 beads. It is known that the enzyme product PAP is susceptible to air oxidation [144], allowing only limited time for linear accumulation of product on the electrode surface. However, we observed that in our device the currents from both active sensors kept increasing over the time period of measurement, i.e., for $\sim 6\text{min}$, and a plateau was not yet reached. With this large window for signal acquisition, one can conveniently adjust the detection time according to the desired signal to noise ratio.

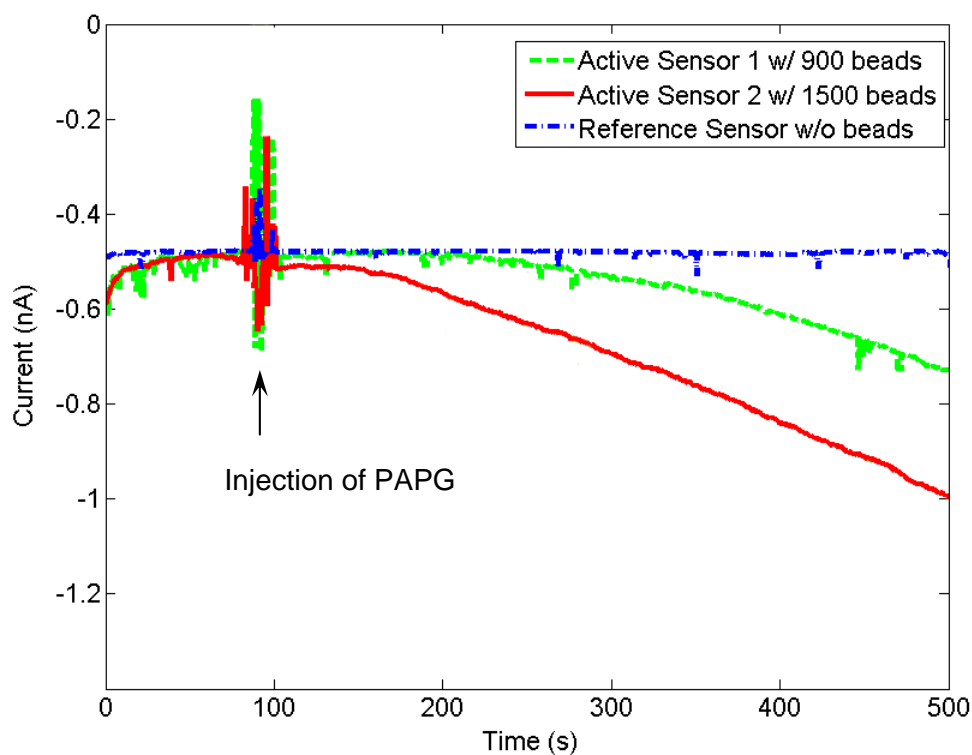


Figure 4.17: The amperometric responses of identical IDAs with different number of beads in presence

The signal from 900 MyOne Dynabeads corresponds to about 50 attomole of β -galactosidase, according to the binding capacity of the beads given by the manufacturer, i.e., $\sim 6\mu\text{g}$ β -galactosidase per mg of beads. This result implies that our device exhibits a significantly improved performance compared with a similar IDA design [145], which detected a minimum number of 140 Dynabeads M-280 ($2.8\mu\text{m}$ in diameter). The surface area of 140 M-280 beads is more than that of 900 MyOne beads, and we are far from reaching the limit of detection yet as the signal to noise ratio from figure 4.17 is much greater than 3. We attribute the improved sensing capability of our devices to the fact that the beads are magnetically assembled in the closest proximity to the electrode surfaces and uniformly distributed among the sensing regions without blocking the electrode, as

no such magnetic manipulations took place in the previous work. The uniform distribution of beads also allows each bead to equally contribute to the electrochemical signal with maximum capacity, because the diffusion of the enzyme product, generated on the bead surface, into bulk solution is minimized.

Figure 4.17 also illustrates that with the smaller number of beads assembled between the IDAs, the current increased at a smaller rate. The slope of the current-time curve corresponds to the rate of the enzymatic reaction that produces PAP at the bead surface. Thus, with concentrated enzyme substrate solution, the larger slope implies that a larger amount of enzyme presents in the sensing region due to more densely assembled beads. From this experimental result, we infer that increasing the pre-concentration level of β -galactosidase via higher number density of microbeads assembled between the IDAs would significantly increase the rate of amperometric current increase. Therefore, achieving denser bead distribution among fewer pairs of the IDAs should further improve the performance including the sensitivity and limit of detection of the immunoassay.

CHAPTER 5

A Microfluidic Mixer Based on Parallel, High-speed Circular Motion of Individual Microbeads in a Rotating Magnetic Field

5.1 Introduction

Mixing of fluid in microchannels is important in a variety of applications, e.g., in the homogenization of reagents for efficient chemical reactions on a chip, and in the control of dispersion of material to desired regions inside the microchannel or along the direction of flows [121]. However, it is difficult to mix solutions continuously flowing through microfluidic channels, because flow in microchannels is laminar in nature due to small Reynolds numbers ($Re < 1$).

Recently, a number of micromixing devices have been reported [146]. Among those, passive mixers have advantages in regards that they are inexpensive, simple to operate, and work for any kind of species to be mixed. The most common passive mixing device is based on the principle of “lamination,” in which the flow is split into many subsequent flows to reduce the diffusion length [147][148]. Passive mixing by generating transverse flow with smart designs of channel geometries that stretch and fold volumes of liquid over the cross section of the microchannel has been demonstrated [121][149]. The disadvantages of passive mixers include the complicated 3-D fabrication and relatively long mixing lengths. Active mixers exert time-dependent disturbance in the flow field. While some active mixers integrate moving components on the chip to impose disturbance in the flow [150], others utilize field effects, such as acoustic wave [151][152][153], electrokinetic phenomena [154][155], and magnetic forces [122][76],

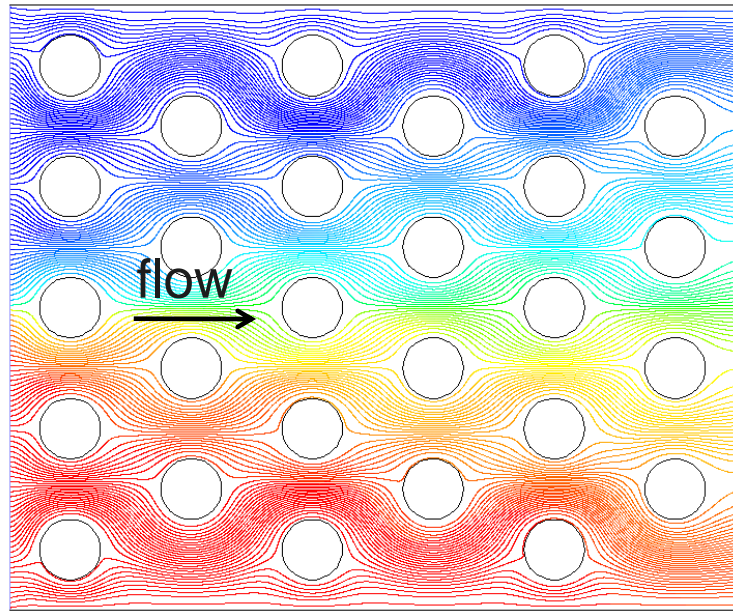
on suspended entities in the fluid. The suspended entities may be the species of interest that need to be mixed or other materials employed to impose perturbations in the flow. Among different kinds of active mixers, magnetic force-based mixing has the advantage of negligible influence on the physical and chemical nature of most species to be mixed.

In this work, we demonstrate a new magnetic micromixer, which is based on parallel manipulation of individual magnetic microbeads that are attracted to soft ferromagnetic features fabricated on the bottom surface of a microchannel. Specifically, we use an external rotating magnetic field to induce synchronized circular motion of individual magnetic beads around the soft magnets, thereby generating secondary flow in the form of local vortices across the microchannel. Mathematical modeling and numerical analysis were used to study the dynamics of the bead motion and predict the performance of the proposed device. The mixing efficiency of the device was demonstrated by fluorescence intensity profiles across the channel after mixing two streams of flow, one fluorescent and the other non-fluorescent, in a microchannel.

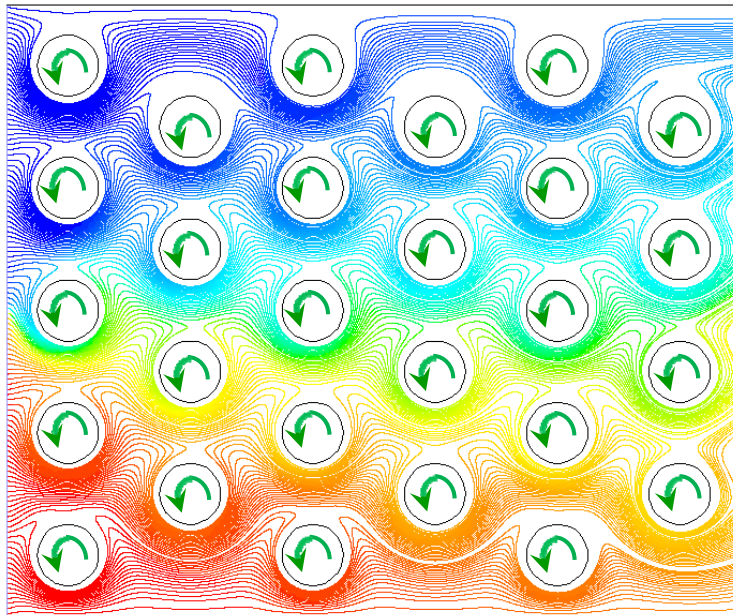
5.2 Methods and Materials

The development of our micromixer started with the investigation of the fluid dynamics of two parallel streams of flow inside a microchannel with the presence of an array of cylinders. To simplify the computation, we devised a 2D model in FLUENT by assuming that the channel is infinitely tall and the cylinders infinitely long. If the cylinders are stationary, the flow simply splits and recombines as it passes by the cylinder array (figure 5.1a). However, if the cylinders were allowed to rotate about their own axes, the flow would be stretched and folded, due to no-slip boundary condition of fluid, as it passes by the rotating cylinders (figure 5.1b). As a result, the mixing of the two flow

streams is more effective due to the local secondary flow. The difference in mixing efficiency in the passive and active micromixers is illustrated by the mass fraction in the simulations with other conditions held the same. The flow speed was 0.5mm/s and diffusion constant $D = 2 \times 10^{-10} \text{ m}^2/\text{s}$ in both cases. The angular speed of the cylinders in figure 5.1b) is 500 rad/s. In addition, for a given flow speed, faster rotation of the cylinders results in more effective mixing due to the more pronounced stretch-fold effect, which induces more secondary flow around the individual cylinders.



a)



b)

Figure 5.1: Top-down view of two streams of flow passing through an array of cylinders ($3\mu\text{m}$ diameter) inside a microfluidic channel
(Streamlines colored by mass fraction)

- a) Flow splits and recombines when passing through stationary cylinders;
- b) Flow is stretched and folded by synchronized rotation of cylinders

It is not very practical to have rotating cylinders inside a microchannel of a simple lab-on-a-chip system. Our idea of generating local secondary flow inside the microchannel was to make the stationary cylinders magnetic and subject them to an external rotating magnetic field. The magnetic stray fields among an array of the magnetic cylinders subjected to an in-plane bias field are shown in figure 5.2a). It illustrates that two field maxima, indicated by the red-orange color, are clearly present at two opposite edges of each cylinder, corresponding to the north and south poles of the cylindrical soft magnets. This simulation was carried out with COMSOL Magnetostatics Module and the properties of a typical soft ferromagnetic material $\text{Ni}_{80}\text{Fe}_{20}$ were used. Figure 5.2a) also shows that the poles of the soft magnets always align with the direction of the bias field, so the rotation of the in-plane bias field leads to the rotation of the magnetic poles of the soft magnets about the centers of the cylinders. Magnetic beads in close proximity will always be attracted to field maxima and hence will follow the rotation of the bias field if the magnetic force on the beads can overcome the reaction forces such as the fluid drag and/or the friction on them. A schematic illustration of two magnetic beads following the rotation of the bias field is presented in figure 5.2b). We point out that the motion of the microbeads will lag behind the bias field due to the reaction forces. The orbital motion of the magnetic beads around the cylinders will induce local disturbance of the incoming flow and can be used for microfluidic mixing purposes. Detailed analysis will appear in the next section.

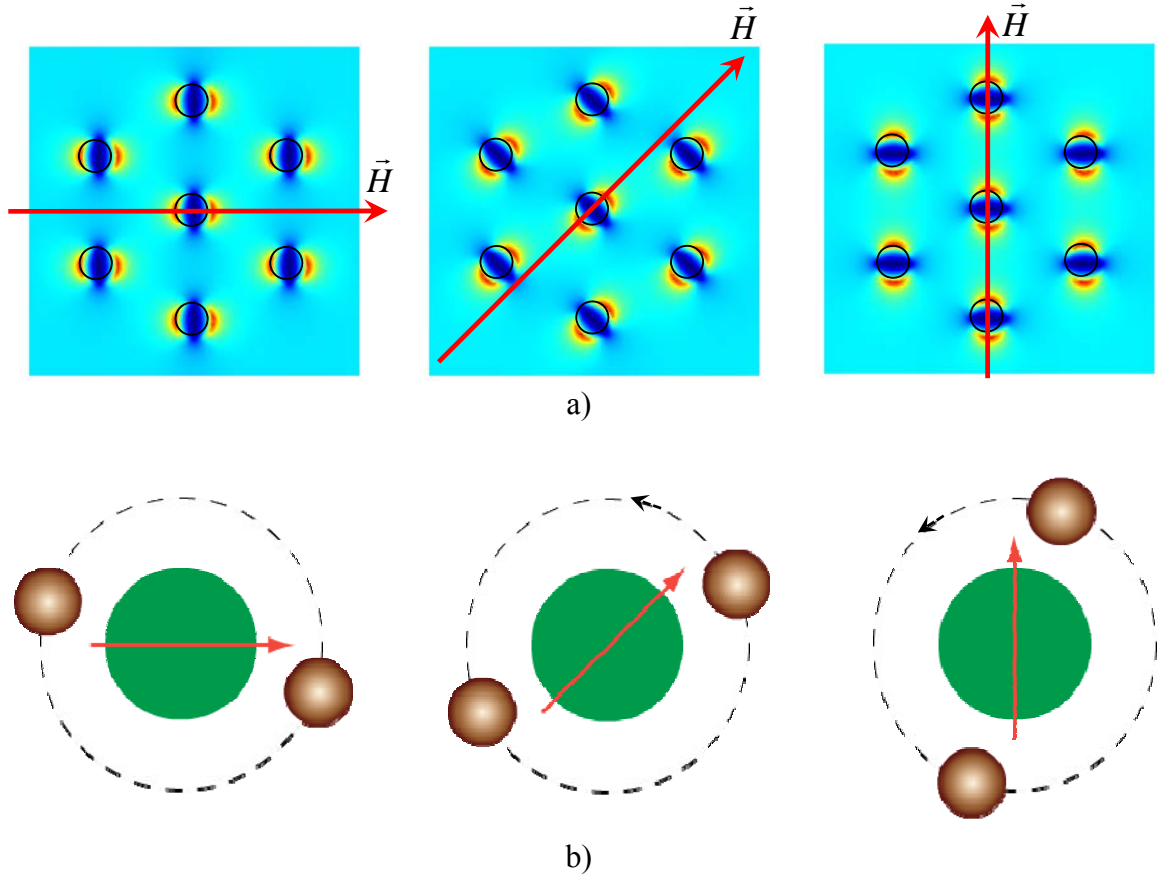


Figure 5.2: Working principle of our magnetic micromixer
a): Top-down view of the magnetic stray fields among NiFe cylinders as the bias field rotates (colored by field strength; the dark circles depict the edges of the cylinders)
b): Schematics of two magnetic beads (brown) orbiting around a magnetic cylinder (green) due to the rotation of the bias field

For easy fabrication and less flow resistance inside the microchannel, we proposed to reduce the magnetic cylinders, i.e., 3D structures, to magnetic discs in the form of 2D structures on the bottom surface of the channel. The sketch of our actual micromixer is shown in figure 5.3. An external magnetic field is oriented in a way it provides an in-plane magnetization of the NiFe disc magnets inside the channel. Nearby magnetic microbeads will be attracted to the maximum stray fields of the discs and trapped there with a downward magnetic force balanced by the reaction force from the

rigid bottom surface of the channel. As the external field rotates, the beads will follow the maxima of the moving stray fields and orbit around the discs, provided the magnetic force on the beads can overcome the relevant resistant forces such as friction and/or fluid drag.

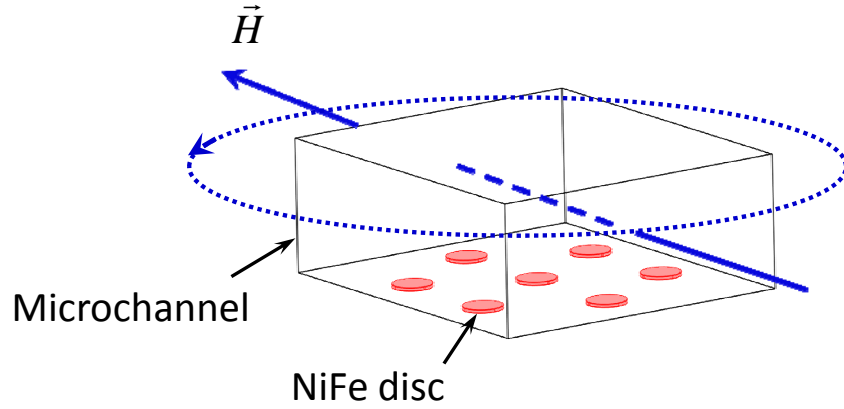


Figure 5.3: Conceptual design of our magnetic micromixer

For parallel control of individual beads in the manipulation, we design the size of the NiFe discs in the same range of that of the target magnetic beads, i.e., Dynabeads M-280 (2.8 μm in diameter). M-280 beads were chosen because the visualization of them using a typical optical microscope is convenient.

5.3 Theoretical Analysis

As the poles of NiFe disc magnet rotate with an angle ϕ , the new location of the field maxima shift relative to the position of the beads at the original field maxima, leading to a different magnetic force on the beads and the net force will drive the beads to new equilibrium locations. The separation between the beads and the closest magnetic poles is determined by the combination of the angle ϕ , the radial location of the bead from the center of the NiFe disc r , and the minimum separation distance between the

bead and the substrate h , as indicated in figure 5.4. Due to symmetry, only one bead is shown in the figure. The resulting magnetic force on the bead can be decomposed into three components: radial, tangential, and z-component magnetic forces, each of which is a strong function of the spatial coordinate r , ϕ , and h .

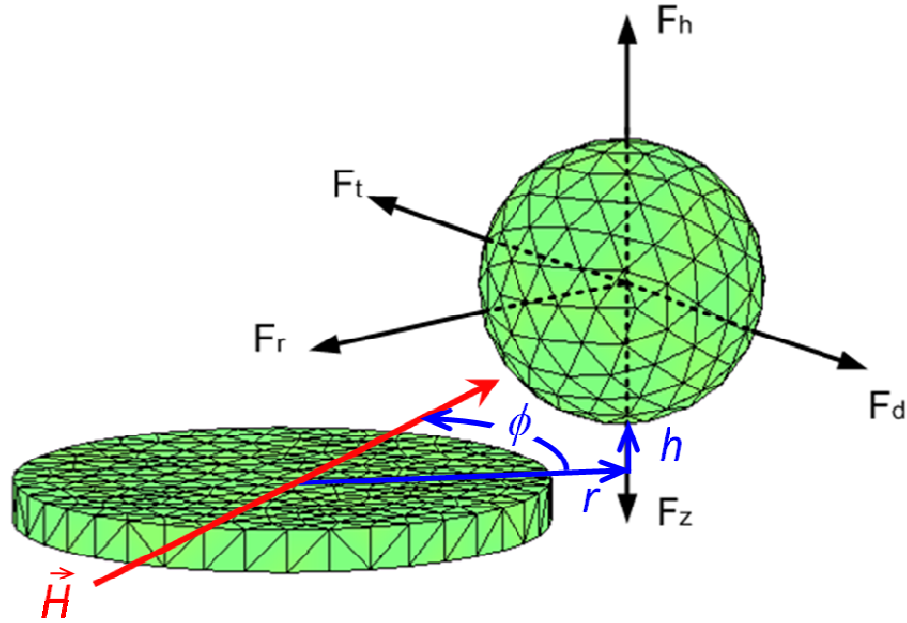


Figure 5.4: Forces on a bead orbiting around a NiFe disc due to a rotating magnetic field

Because of the short relaxation time in magnetizing NiFe alloy, it is reasonable to assume that the rotation of the poles of the NiFe discs is always in phase with the rotation of the external field. With slow rotation of external field, the bead would follow the rotation and circle around the disc with physical contact against the surface of the substrate, i.e., $h = 0$. Thus, friction between bead and the surface is present. As the bead follows a relatively fast rotation of external field, we argue that there is a thin layer of fluid in between the bead and the substrate, and hydrodynamic pressure builds upon the lower surface of the bead as in the case of lubrication problems. In both cases, the beads

will lag behind the field with an angle ϕ due to friction and/or viscous effects of the suspending medium. Relevant forces on the bead in the latter case are sketched in figure 5.4. The gravity and buoyancy forces are neglected because they are relatively small (see analysis in chapter 2). As a result, the tangential magnetic force is balanced by the drag force, and the z-component magnetic force is balanced by the hydrodynamic pressure force, while the radial component of magnetic force serves as the centripetal force to sustain the circular motion of the bead with an angular velocity ω and an orbital radius r . The system of equations for force balance in three directions is given by:

$$F_t(r, \phi, z) = F_d(r, z, \omega) \quad (5.1)$$

$$F_r(r, \phi, z) = mr\omega^2 \quad (5.2)$$

$$F_z(r, \phi, z) = F_h(r, z, \omega) \quad (5.3)$$

where $z = h + R$ with R being the radius of the magnetic bead is the distance between the center of the bead and the substrate, i.e., the orbital height of the bead. At a steady-state rotation of an external magnetic field with a given ω , the corresponding phase angle ϕ , orbital radius r , and orbital height z of the bead can be determined by solving the above equations.

5.3.1 Magnetic Field and Magnetic Force of Cylindrical Soft Magnets

A cylindrical type soft magnet is sketched in figure 5.5 with reference frames. Let R denote the radius of the cylinder, z_1 and z_2 the axial position of the bottom and top of the cylinder.

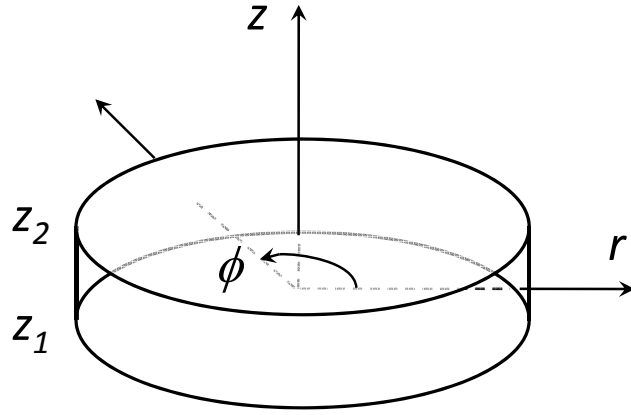


Figure 5.5: Sketch of a cylindrical soft magnet

Assume that the soft magnet is magnetized to saturation, M_s , by an external bias field along a horizontal direction from left to right. The magnetic field of a single cylindrical soft magnet can be derived using a charge model and the results are given by [143]:

$$B_r(r, \phi, z) = \frac{\mu_0 R M_s}{2N_\phi} \sum_{n=0}^{N_\phi} \sum_{k=1}^2 (-1)^{(k+1)} S_\phi(n) \cos(\phi'(n)) \times [r - R \cos(\phi - \phi'(n))] I(r, \phi, z; R, \phi'(n), z_k) \quad (5.4)$$

$$B_\phi(r, \phi, z) = \frac{\mu_0 R^2 M_s}{2N_\phi} \sum_{n=0}^{N_\phi} \sum_{k=1}^2 (-1)^{(k+1)} S_\phi(n) \cos(\phi'(n)) \times \sin(\phi - \phi'(n)) I(r, \phi, z; R, \phi'(n), z_k) \quad (5.5)$$

$$B_z(r, \phi, z) = \frac{\mu_0 R M_s}{2N_\phi} \sum_{n=0}^{N_\phi} S_\phi(n) \times \sum_{k=1}^2 (-1)^k \cos(\phi'(n)) g(r, \phi, z; R, \phi'(n), z_k) \quad (5.6)$$

where ϕ' and S_ϕ are given by:

$$\phi'(m) = \frac{m}{N_\phi} 2\pi, \quad m = 0, 1, 2, \dots, N_\phi \quad (5.7)$$

$$S_\phi(m) = \begin{cases} 1/3 & (m=0) \\ 4/3 & (m=1,3,5,\dots) \\ 2/3 & (m=2,4,6,\dots) \\ 1/3 & (m=N_\phi) \end{cases} \quad (5.8)$$

and the functions g and I are defined by:

$$g(r, \phi, z; r', \phi', z') = \frac{1}{[r^2 + r'^2 - 2rr' \cos(\phi - \phi') + (z - z')^2]^{1/2}} \quad (5.9)$$

$$I = \begin{cases} \frac{(z - z_k)g(r, \phi, z; r', \phi', z')}{r^2 + r'^2 - 2rr' \cos(\phi - \phi')}, & \text{if } r^2 + r'^2 - 2rr' \cos(\phi - \phi') \neq 0 \\ \frac{-1}{2(z - z_k)^2}, & \text{if } r^2 + r'^2 - 2rr' \cos(\phi - \phi') = 0, z \neq z_k \end{cases} \quad (5.10)$$

The above equations can be used to obtain the field of a single soft magnet of given dimensions. For multiple soft magnets in an array with an in-plane magnetization field externally applied, the total field will be the superimposition of individual fields biased by the applied field. Once the magnetic field is known, the magnetic force on a nearby magnetic bead can be calculated.

With an external field applied to an array of NiFe discs at a fixed direction $\phi = 0$, we calculated magnetic force on an M-280 bead as a function of its location (r, ϕ, z) . In the simulation, the array consists of 25×25 $3\mu\text{m}$ NiFe discs with $9\mu\text{m}$ spacing in both directions, and the thickness of the discs is 150nm . The strength of the in-plane bias field is 0.15T , sufficient to saturate both the soft magnets and the microbeads. The saturation flux density of the NiFe disc magnets is assumed to be 660kA/m , and the saturated magnetic moment of the M-280 bead is 15kA/m . The magnetic force was calculated by treating the magnetic bead as a dipole point at its mass center. A numerical code was written in Matlab to calculate the magnetic forces.

A typical trend of the magnetic forces on an M-280 bead as a function of ϕ is shown in figure 5.6. It illustrates that both z-component force F_z and radial force F_r are cosine functions of ϕ , while the tangential force F_t is a sine function of ϕ . The minima of both F_z and F_r locate at $\phi = 0$, where one of the magnetic poles of the NiFe disc locates, while the maxima at $\phi = \pm\pi/2$. Due to the symmetry of the field and field gradient, $F_t = 0$ at $\phi = 0$, and it peaks at $\phi = \pm\pi/4$. The magnitude of the positive and negative F_t is the same, making F_t anti-symmetric about $\phi = 0$. The characteristics of F_t imply that only if the bead lags behind the rotation of the magnetic poles of the NiFe disc will it be subjected to a positive tangential force. In addition, the tangential force increases with increasing phase angle up to $-\pi/4$, beyond which the tangential force starts to decrease. This result implies that the practical phase angle of the bead with respect to the rotating bias field is within the range from 0 to $-\pi/4$, as indicated in figure 5.6.

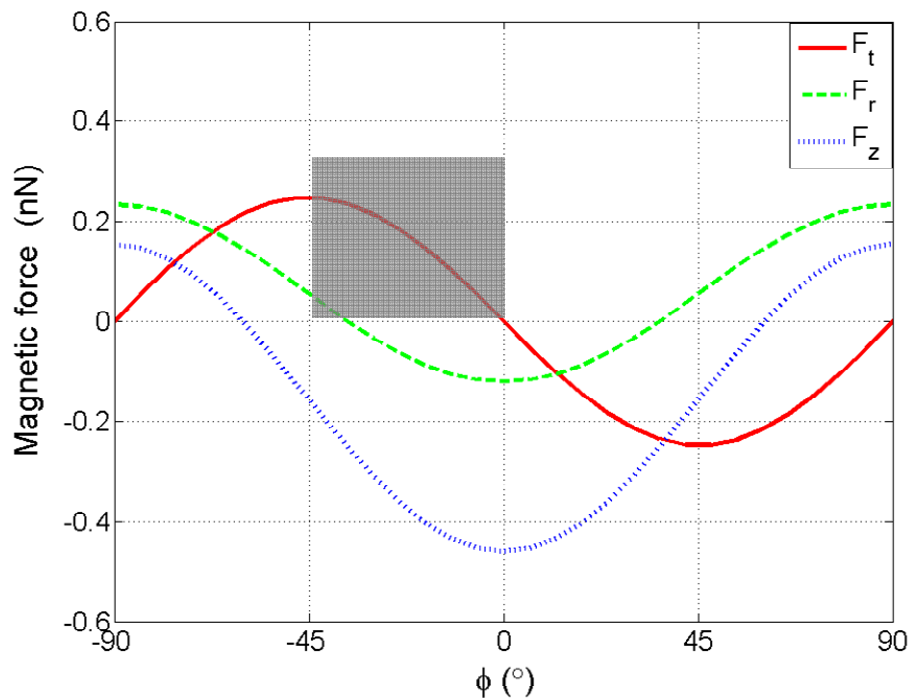


Figure 5.6: Magnetic force on a M-280 bead as a function ϕ ($r = 3\mu\text{m}$ and $h = 70\text{nm}$)

The magnetic force as a function of radius r with the phase angle ϕ between 0 and $-\pi/4$ is shown in figure 5.7. It suggests that F_z changes from positive to negative as r increases from 0, the center of the NiFe disc, to $6\mu\text{m}$, the center of the gap between two neighboring discs. This result suggests that, with an in-plane bias field, the magnetic force is repulsive on top of the disc, and downward attraction occurs outside of the edge of the disc. The maximum attraction locations locate outside of the edge ($r = 1.5\mu\text{m}$) of the disc and the attraction strength decreases with increasing lag of the bead. At the same time, F_t is always positive along r with ϕ between 0 and $-\pi/4$, and it increases with larger phase angle. The maximum tangential force locates just outside of the edge of the disc. Figure 5.7 also illustrates that F_r changes direction from directing outwardly to inwardly as r increases from the center of the NiFe disc to the center of the gap. The transition point occurs at a larger r with increasing lag of the bead, and the magnitude of the inward force decreases with larger phase angle. The fact that the inward radial force, which is required to sustain the circular motion of a bead around the NiFe disc, exists outside of the edge of the discs implies that the orbital radius will always be greater than the radius of the discs and will increase with increasing lag. The actual orbital radius of the bead will be a function of other forces in the system and must be determined by solving the system of equations (5.1-5.3) simultaneously.

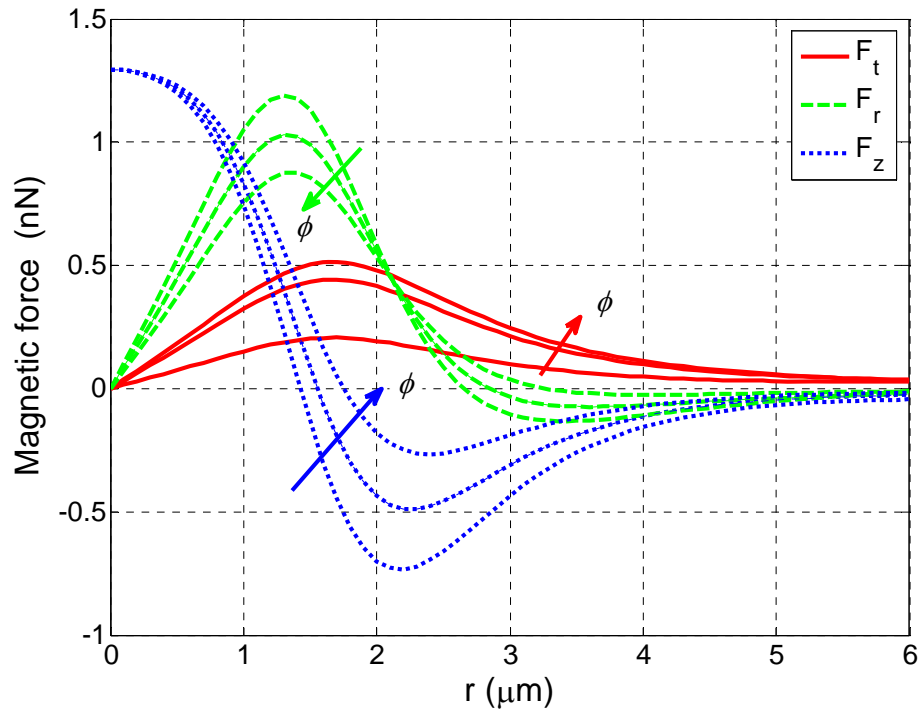


Figure 5.7: Magnetic force on a M-280 bead as a function r and ϕ ($h=70nm$)

5.3.2 Drag Force on a Microbead Moving Close to Substrate

Drag force on a microbead in bulk fluid with relative motion to the fluid was discussed in Chapter 2. The result is described by Stokes' law: $\vec{F}_D = 6\pi\eta RU$. When the microbead moves close to the substrate, the influence of the wall has an effect on the drag force. As the minimum separation between the bead and the substrate h approaches zero, a correction factor needs to be introduced to Stokes' law. R. G. Cox and co-workers [156] as well as M. E. O'Neill and co-workers [157] have independently worked out this correction factor by matching asymptotic expansions of an inner solution valid within a region in the vicinity of the minimum separation point with an outer solution valid elsewhere. In the inner region where the velocity gradient and pressure are large, the leading terms of the asymptotic expansion of the solution satisfies the lubrication theory.

The result by O'Neill and co-workers using tangent sphere coordinates represents a more accurate solution when compared with the 'exact' solution [158]. In terms of a non-dimensional parameter $\varepsilon = \frac{h}{R}$ where R is the radius of the bead, the drag force derived

by O'Neill and co-workers is of the following form:

$$\vec{F}_d = -6\pi\eta RU \left[0.5846 + \left(\frac{8}{15} + \frac{64}{375} \varepsilon \right) \log\left(\frac{2}{\varepsilon}\right) + O(\varepsilon) \right] \quad (5.11)$$

For circular motion of the microbead, $U = r\omega$ in the above equation. For microfluidic mixing purpose, the actual angular speed of the beads orbiting around the NiFe discs is of significance. Therefore, in the discussion that follows, we focus our analysis on the theoretical maximum angular velocity of the microbead.

5.3.3 Maximum Angular Velocity of Microbeads

The characteristics of the tangential magnetic force from figures 5.6 and 5.7 suggest that the phase angle between the microbeads and the rotating magnetic field must fall between 0 and $-\pi/4$ for a given rotation. With an increasing rotation speed, the lag must increase so that the bead is subjected to a larger tangential magnetic force to overcome the increasing drag force according to equation (5.1). Once the rotating speed of the magnetic field is increased to a point that the lag of the bead reaches $-\pi/4$, the maximum tangential magnetic force the system can provide is reached. Beyond this speed, the bead won't be able to follow the rotation anymore due to imbalanced drag force. Therefore, the maximum tangential magnetic force that the system can possibly provide determines the maximum angular velocity at which the beads can orbit around the NiFe discs.

Since the maximum tangential magnetic force always occurs at a phase lag $\phi = -\pi/4$, it is only of function of the orbital radius r and orbital height h . Combining equations (5.1) for $\phi = -\pi/4$ and (5.11) yields the following expression for the maximum angular velocity of the bead:

$$\omega_{\max} = \frac{F_t(-\pi/4, r, h+R)}{6\pi\eta Rr} \left[0.5846 + \left(\frac{8}{15} + \frac{64}{375} \frac{h}{R} \right) \log\left(\frac{2R}{h}\right) \right]^{-1} \quad (5.12)$$

Meanwhile, this maximum angular velocity must satisfy equations (5.2) and (5.3) in the form of

$$mr \omega_{\max}^2 = F_r(-\pi/4, r, h+R) \quad (5.13)$$

$$F_h(r, h+R, \omega_{\max}) = F_z(-\pi/4, r, h+R) \quad (5.14)$$

Because of the complexity in deriving an explicit relation between F_h and the variables r , h , and ω , simultaneously solving equations (5.12-14) for ω_{\max} is not trivial. In addition, other physical forces such as electrostatic force and Van de Waals force may be relevant when the separation h between the bead and the surface is small. To avoid the complication, we focus on simultaneously solving the force balance in ϕ and r directions (equation 5.12 and 5.13) only for ω_{\max} as a function of the separation h . As long as the range of h considered covers the actual equilibrium separation that satisfies the force balance in z -direction, i.e., equation (5.14), this simplification is justified without the loss of generosity. The resultant angular velocity ω_{\max} of the bead corresponds to the critical rotating speed of the magnetic field beyond which the bead won't be able to follow the rotation of the external magnetic field at a given separation distance h . Figure 5.8 plots the relation between the critical rotating speed of the external magnetic field and the

separation distance h between the M-280 beads and the magnetic chip described previously.

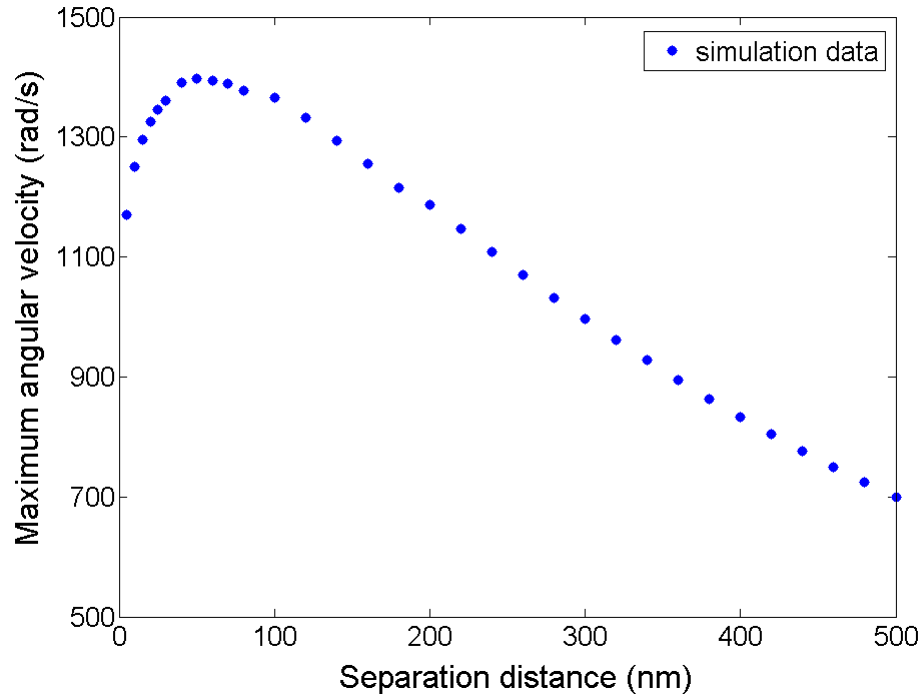


Figure 5.8: Theoretical maximum angular velocity of Dynabeads M-280 as a function of the separation h between the bead and the surface of the magnetic chip

The result from figure 5.8 suggests that our system can achieve extremely high angular velocities of the orbiting beads, i.e., in the order of 1,000 rad/s, over a range of separation between the bead and the magnetic chip, which indicates a relatively large tangential magnetic force the system can exert on the beads. Figure 5.8 also illustrates that the critical rotation speed, in general, increases linearly with decreasing separation distance between the bead and the magnetic chip. This is expected because the tangential magnetic force is stronger when the bead is closer to the magnetic chip. Beyond a turning point, however, the trend is reversed as the separation distance becomes extremely small. We attribute this reversal to the dramatic increase of drag force as a function of the

separation distance (see equation 5.11). Although predicting the actual separation distance is out of the scope of this work, we believe the separation distance to be within the range shown in figure 5.8, i.e., from 5nm to 500nm; and because the z-component magnetic force close to the surface of the magnetic chip is relatively large, i.e., in the order of nN (see figure 5.6 and 5.7), we expect it to fall in the lower range. In the discussion to follow, we seek to probe this parameter through experimental data.

5.4 Device Preparation and Experimental Setup

Arrays of NiFe micro discs were fabricated on a silicon wafer using lithography, e-beam evaporation, and lift-off techniques, followed by conformal deposition of a SiO₂ layer (see detailed in chapter 3). A typical device is shown in figure 5.9. The diameter of the NiFe discs is 3 μ m and the spacing between closest neighboring discs was 9 μ m in this device. The thickness of the discs is about 150nm. The triangular layout of the NiFe micro discs was intended for better loading of the beads to the discs from a flow of bead suspension inside a microchannel.

After dicing the wafer into individual magnetic chips, the SiO₂ surface of the chips was treated with 3-aminopropyltriethoxysilane (APTES). Then microfluidic channels made in PDMS, 20 μ m tall and 120 μ m wide, were aligned and assembled with individual magnetic chips. Before delivering microbeads to the NiFe disc magnets, PEGylation of the chip surface was carried out by introducing a PEG-NHS solution (pH8.0) to the microchannel and allow it to react with APTES-treated surface. PEG-coated surface significantly minimizes the non-specific adhesion of the beads to the chip surface (see detailed discussion on surface treatment in chapter 3 and Appendix A).

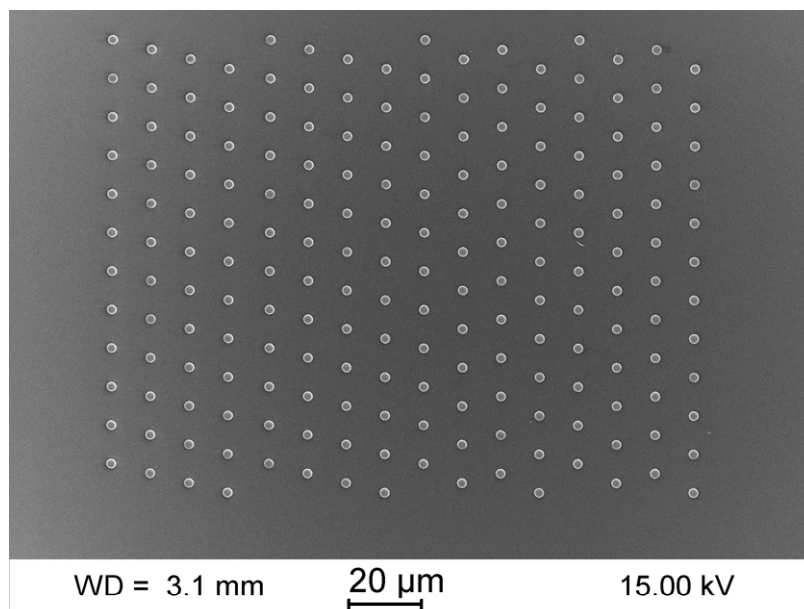


Figure 5.9: A magnetic chip designed and fabricated for microfluidic mixing

A rotating magnet field can be constructed in many ways. The simplest way is to use an external permanent magnet that rotates above the microchip with NiFe discs contained in a microchannel. To provide an in-plane magnetization to the NiFe discs, the external magnet needs to be orientated in such a way that the magnetic field lines are parallel to the surface of the magnetic chip. The tunable rotation of the external magnet can be realized by attaching it to a motor, which is driven by a DC power supply with adjustable current input for speed control. A fixture for attaching a permanent magnet to a motor was machined for this work as shown in figure 5.10a.

The external magnet attached to the motor is a neodymium-iron-boron rare earth magnet purchased from Magcraft® with its dimensions and magnetic pole orientation shown in figure 5.10b. Hence, the arrangement in figure 5.10a provides major magnetic field lines parallel to the magnetic chip beneath the magnet. The magnitude of the applied in-plane field depends on the separation distance between the magnetic chip and the

external magnet, which can be adjusted by the z-travel function of the magnet holder included in the fixture. The rotation center of the permanent magnet was aligned to the normal of the NiFe disc array on the magnetic chip by adjusting the x- and y-travel functions of the magnet fixture. Hence the separation distance between the disc array and the external magnet does not change as the magnet rotates. Because the size of the NiFe disc array is relatively small compared to that of the external magnet, the variation in the magnitude of the bias field applied to each NiFe disc is negligible at any instant in time during the rotation of the magnet.

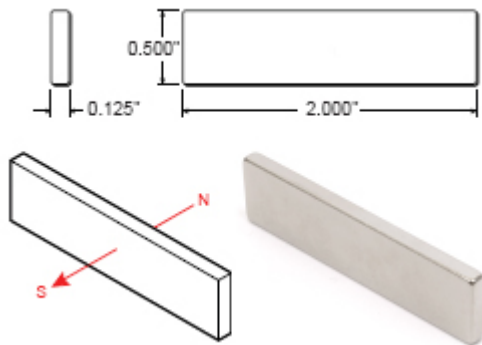
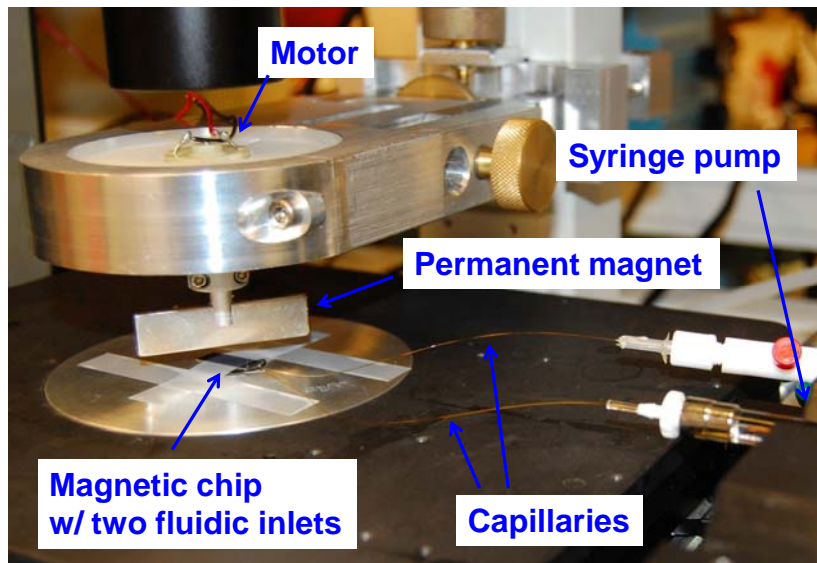


Figure 5.10: Experiment setup for our magnetic micromixer
a) Picture of the setup; b) The dimensions and pole orientation of the magnet

A programmable syringe pump from Harvard Apparatus (Model HA2000W) was used to load the beads to the magnetic chip and control two streams of fluid inside the microchannel for mixing experiment. An inverted microscope (Nikon Eclipse TE2000) equipped with a fast speed CCD camera, Phantom (version 9.1) from Vision Research (NJ, USA), was used to monitor the motion of the beads inside the microchannel through the optically transparent PDMS. At 960×720 resolution, the Phantom camera can shoot up to 2,000 frames-per-second.

5.5 Experimental Results

5.5.1 High-speed Orbital Motion of Individual Microbeads on a Magnetic Chip

For high loading efficiency, Dynabeads M-280 with original concentration, i.e., $6-7 \times 10^9$ beads per ml, were introduced to the microchannel. The external magnet sits at ~ 1 mm above the magnetic chip (shown in figure 5.10), providing ~ 0.15 T in-plane flux density as measured by a magnetometer. This field is sufficient to magnetically saturate both the NiFe discs on the chip and the M-280 beads inside the microchannel. During the bead loading step, most individual NiFe discs attracted two beads at opposite edge locations (figure 5.11a). This was expected because around each NiFe disc there are two field maxima, i.e., poles, induced by the external field (see figure 5.2). Because the size between the NiFe discs and the beads is comparable, only one bead populates one of the two magnetic poles of each disc. We note from figure 5.11a) that the location of the beads was outside the perimeter of the NiFe discs, which is in consistence with the theoretical analyses (see figure 5.7 and corresponding discussion).

Once the beads were loaded to the magnetic chip, the rotation of the external magnet was driven by a motor and the speed was controlled by adjusting the DC power

supply to the motor. Figure 5.11 shows a series of snapshots of the orbital motion of the loaded beads around individual NiFe discs recorded by the CCD camera. The beads were observed to synchronously orbit around individual NiFe discs, following the rotation of the external magnet. As the rotation speed of the external magnet was increased by increasing the current into the driving motor, the beads orbited around the NiFe discs with increasing speed and kept following the rotation as suggested by visual observation through the eyepiece of the microscope. The fastest rotation of the external magnet experimented was 9,000 rpm, as measured by a photo tachometer (Extech L957245). From the image analysis of the movie recorded by the Vision Research CCD camera (Phantom v9.1) operated at 2000 frames-per-second, we verified that the angular speed of the beads was 942 rad/s, confirming that the beads were able to follow the rotation of the external magnet. For safety concerns, we didn't experiment rotation speed beyond 9,000 rpm to identify the critical speed at which the beads won't be able to following the rotation of the external magnet.

The experimental result that the beads were able to follow the rotation of the external magnet above 942 rad/s strongly supports our mathematical model and numerical simulations on the proposed device in previous sections. In addition, it suggests that the separation distance between the bead and the surface of the magnetic chip indeed fall into the lower range of that shown in figure 5.8.

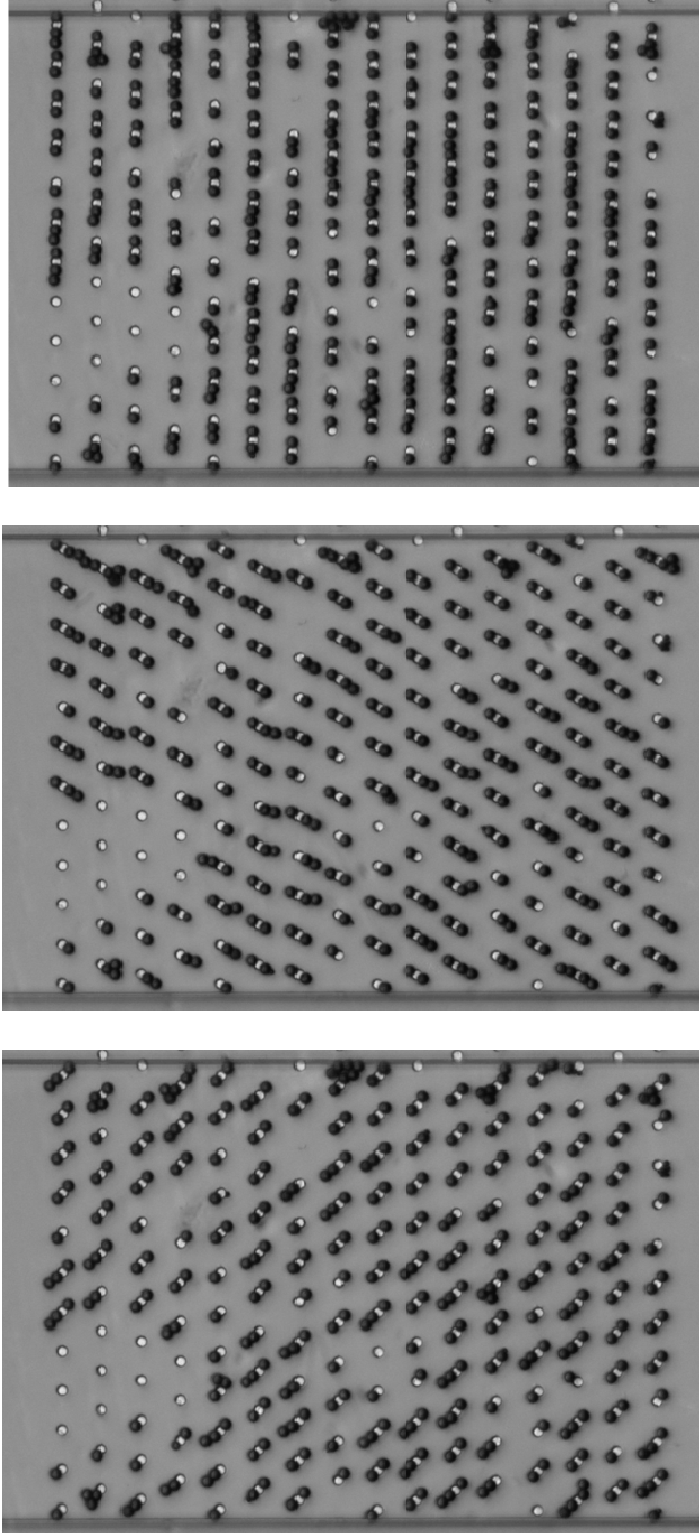


Figure 5.9: Snapshots from a movie, recorded by a CCD camera operated 2000 frames-per-second, of magnetic beads M-280 (black) orbiting around NiFe discs (white) counter clockwise while the external magnet rotated CCW at 9000 rpm

5.5.2 Mixing of Two Streams of Fluid in a Microchannel

The corresponding linear velocity of the beads orbiting around the NiFe disc at 9000 rpm is ~ 3 mm/s, assuming an orbital radius of $3\mu\text{m}$. This relatively high speed can produce significant secondary flow inside a microfluidic channel, because typical flow in microchannel is in the order of mm/s or less. In a sequential experiment using the same device shown in figure 5.11, we injected two streams of fluid, one of which was pure DI water and the other with fluorescent nanoparticles, into the microchannel while the external magnet was rotating at 9,000 rpm. The fluorescent nanospheres Fluoresbrite™ YG (~ 40 nm) were purchased from Polysciences Inc. (Warrington, PA). Original concentration with 2.62% solids-latex in water was used in the experiment. The average flow speeds of both streams were controlled at ~ 1 mm/sec by the syringe pump (Harvard Apparatus HA2000W) capable of controlling the flow rate out of two syringes in parallel. As revealed in figure 5.12, in the upstream of the channel where NiFe discs and orbiting microbeads were absent, the two streams of fluid flew parallel with each other without observable mixing. As they reach the mixing region where individual M-280 beads were simultaneously orbiting around the NiFe discs at 9,000 rpm, the two separate streams started to mix immediately. The mixing region was about $120\mu\text{m}$ wide and $200\mu\text{m}$ long as indicated in figure 5.12b).

The required length of mixing region strongly depends on the ratio between the linear speed of the orbiting beads and the speed of the flow. The experiment shown in figure 5.12 corresponds to a linear velocity of the beads about three times of the flow speed. Figure 5.12b) indicates that within $200\mu\text{m}$ mixing length, the two streams seemed to have effectively mixed with each other. This mixing length is considerably smaller than the several millimeters reported for passive mixer using statically packed

microbeads [159] at flow speeds in the same range. In addition, there are plenty room for improvement in our magnetic micromixers. First, we are far from reaching the critical angular speed of the microbeads yet. Secondly, we can further increase the critical speed of the microbeads in the mixer by increasing the magnetic force through using microbeads with larger magnetic moment and/or thicker NiFe discs.

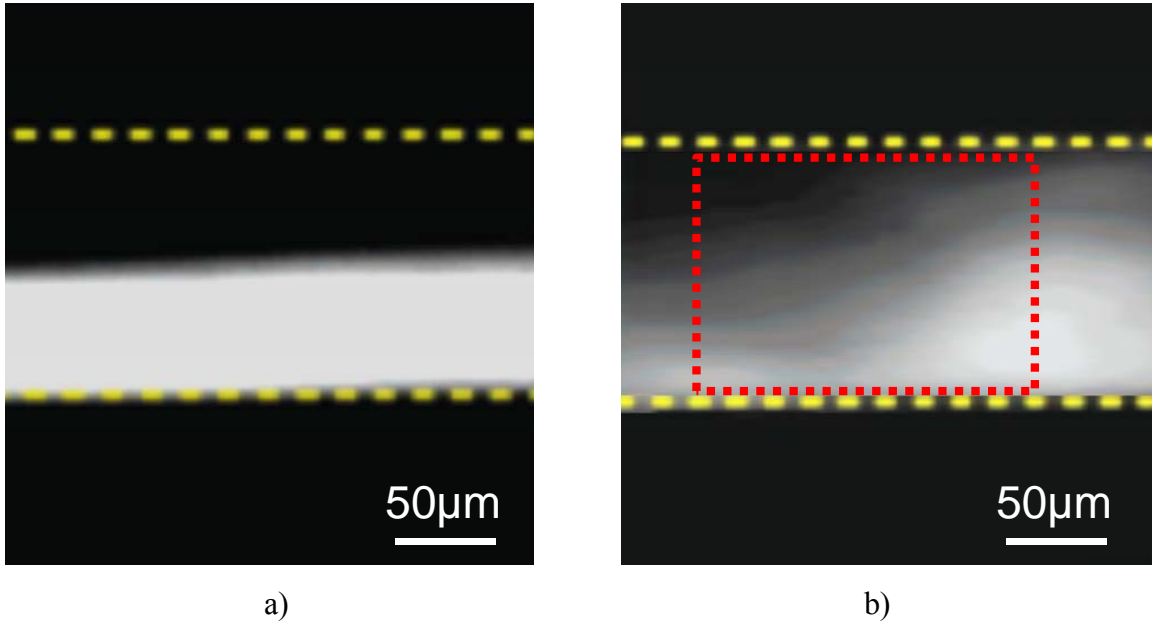


Figure 5.10: Top-down view of two streams of fluid in the microchannel
a) upstream of the channel in the absence of NiFe disc arrays; b) mixing region with individual M-280 beads orbiting around $3\ \mu\text{m}$ NiFe discs at 9,000 rpm
(The dashed yellow lines indicate the walls of the microchannel, and the dotted red rectangle denotes the location of the NiFe disc array)

5.5.3 Controlling the Number Density of Orbiting Beads on a Magnetic Chip

The spacing between the NiFe discs can be used to control the number of the beads circling around each disc. The device shown in figure 5.13 has a reduced spacing, i.e., $3\ \mu\text{m}$ in both directions, among the $3\ \mu\text{m}$ discs. With this design, the orbital radius of two neighboring discs overlaps and interference would occur as the beads move synchronously. Only one of the two competing beads at the opposite magnetic poles from

two adjacent discs can survive to occupy the common orbital radius. As a result, only one bead can orbit around each disc at steady-state condition, as shown in figure 5.13. In comparison with the device shown in figure 5.11, this device has advantage in assembling the beads with higher number density, and the orbital motion of the beads can probably create more pronounced secondary flow for mixing purpose.

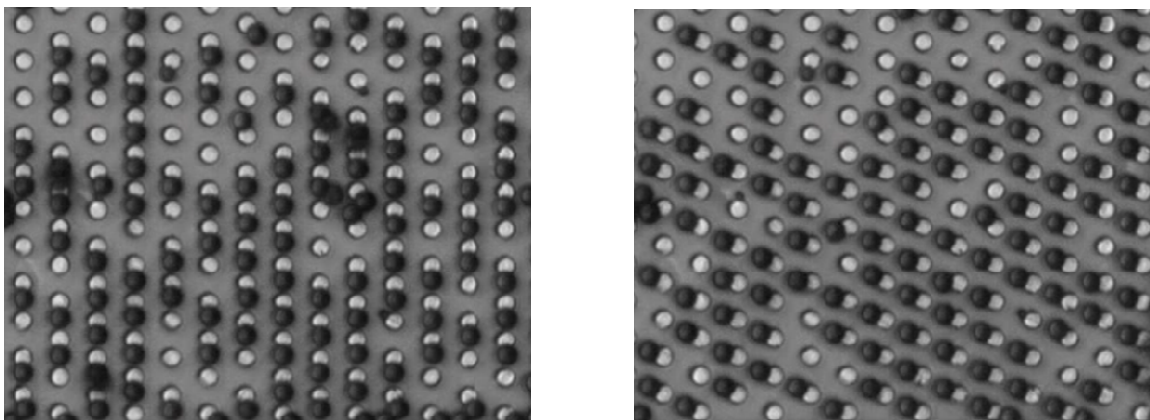


Figure 5.11: Snapshots of single M-280 beads (black) circulating around individual NiFe discs (white) in an external rotating magnetic field

In a device with further reduced spacing between the NiFe discs, i.e., $2\mu\text{m}$, we observed that the interference of the M-280 beads in the rotating field generated a chaotic motion of the beads without predefined path among the array of discs. The chaotic motion of the beads in the mixing region may produce better mixing result. However, the retention of the beads by the NiFe discs in a flow field was seem to be undermined due to the chaotic trajectories of the beads.

5.6 Discussion

The advantages of our micromixer based on the aforementioned magnetophoretic system over other type of micromixers include the following. First, it is simple and free of concerns for heat dissipation, because complicated design of the soft magnetic patterns

or addressable conducting wires are not required. Second, it offers great flexibility since it is rather easy to set up a rotating magnetic field and scale up the array size of the soft magnets to allow synchronized motion of a large number of individual beads on the magnetic chip. Third, the magnetic force in the system is strong enough to retain the orbiting beads against typical flow rates in microfluid systems, making it an ideal platform for mixing continuous flows. And the magnetic force can be further increased by fabricating thicker NiFe discs using electroplating techniques and/or employing magnetic beads with stronger magnetic moment.

We believe the high-speed orbital motion of the microbeads inside the microfluidic channel can also enhance the capture of a target from a continuously flowing fluid onto the surface of functionalized beads. Therefore, this technology may also be used for on-chip sample pre-concentration purpose.

In a separate experiment in which the presence of the NiFe discs is absent and the fluid is stagnant, we observed the magneto rotation of individual beads around their body center in a rotating external field. Hence, we infer that the relaxation time constant of the iron oxide nanoparticles in the M-280 beads is significant enough to cause the magnetic moment of the bead to lag behind the rotation of the external field, resulting in a magnetic torque on the bead surface. This phenomenon has also been recently reported by Janssen et al. [160]. It is believed that the torque can be quantitatively described with a frequency dependent complex susceptibility. Therefore, with the presence of the NiFe discs in a rotating field, the self-spinning of the beads while they orbit around the discs should also be expected. As a result, we infer that in our experiment the beads were spinning about their own mass center as they orbited around the NiFe discs, just like the

motion of earth, self-spinning as it orbits around the sun. The self-spinning of the beads would generate more complicated secondary flow than discussed previously, which may have further contributed to the effective mixing of micro flows as shown in figure 5.12. We note that the spinning of the microbeads without the presence of the soft magnets inside the microchannel cannot be used for mixing continuously flowing streams, because without magnetic force to retain the beads inside the microchannel the spinning beads will be flushed away by the incoming fluid.

The interference of induced orbital motion of microbeads among an array of dense NiFe discs may be utilized for bead sorting purposes. As described previously, if the spacing between the discs is smaller than the diameter of the beads, the beads inside a rotating field can hardly be retained by the NiFe disc array against a flow field due to chaotic trajectories. At the same time, if beads with a diameter smaller than the spacing are also present, the beads will be retained by the array with predefined orbital trajectories around individual discs. Therefore, one can use this phenomenon to separate small beads from large ones in a bead mixture. By integrating two or more arrays of NiFe discs with different spacing inside a microchannel, one can sort magnetic beads according to their size and separate them into different groups and retain them at different locations inside the channel.

CHAPTER 6

Transport and Sorting of Magnetic Beads on a Chip in a Rotating Magnetic Field with Time-varying Strength

6.1 Introduction

Micrometer-sized magnetic beads consisting of magnetic nanoparticles embedded in a polymer matrix offer convenient and inexpensive ways of handling, separating, concentrating, and detecting biological substance including cells and subcellular entities. With the development of microfluidic lab-on-a-chip, microfabricated magnetic devices have been built for a variety of bead manipulations. For example, microscale core/coil design [70], current-carrying wires [69], wire matrix [71], and micropatterned conductors [161] have been design and implemented to trap and transport magnetic beads inside microfluidic channels. However, micro electromagnetic systems are limited to manipulation of small numbers of beads and with low magnetic forces due to complex architecture and Joule heating concerns.

To address these issues, micropatterned soft ferromagnetic features have been used to manipulate magnetic beads. The magnet domains, both orientation and size, of soft ferromagnetic materials can change with an externally applied bias field. As a result, the magnetization of these features, i.e., soft magnets, changes with the bias field. As the magnetization of the soft magnets changes, the nearby magnetic beads will respond to the change due to the magnetic force on the beads. A rotating magnetic field applied to an array of soft magnets can induce periodical change of their magnetization. Using this idea, researchers have demonstrated controlled transport of magnetic beads among the soft magnets [74]. However, the transport mechanism relies on the partial magnetization

saturation levels of the geometrical anisotropy of the material, which is hard to control. Alternative means for bead transport among soft magnets have been demonstrated with travelling wave magnetophoresis [72]. In this system, the construction of the out-of-plane rotating magnetic field was fairly complicated and the transport rate is limited in the order of $\mu\text{m}/\text{sec}$. A more recent work achieved bead transport by translatable local field maxima created by variations in local radii of curvature at the soft magnet edges [73]. In this approach, the geometry of the soft magnets has to be carefully designed with the knowledge of magnetic bubble memory and the transport path is fixed and no flexibility can come from the external control of the rotating magnetic field.

In this work, we employ a simple design of the soft magnets and easy construction of the external rotating field to achieve circular motion of magnetic beads around disc type soft magnets and effectively transport them across the array of the magnetic discs. Our design allows for parallel manipulation of individual beads. A theoretical basis was established to explain the new transport mechanism. We further apply this transport mechanism for on-chip sorting of magnetic beads according their size. The rate of bead transport and sorting in our system are much higher than previous work. The ability to induce the circular and translational motions of individual beads and control their distribution as well as localization on a chip promises a powerful platform for biological sample preparation with multiplexing capability in a lab-on-a-chip environment.

6.2 Working Principles

As discussed in chapter 5, when the rotation axis of the permanent magnet was aligned to the normal of the array of NiFe discs on the magnetic chip, the separation

distance between the disc array and the external magnet does not change as the magnet rotates. Figure 6.1a) shows the side-view of such an experimental setting. The bias field in the plane of the magnetic chip can be calculated using equations (4.2-4) with the geometry and the strength of the pre-magnetization of the permanent magnet. Figure 6.1b) shows the computational result of the bias field of a given rare earth magnet across the centerline of the magnetic chip in x direction. It illustrates that the strength of the bias field peaks at the point directly below the magnet, because of the shortest separation distance between the bottom surface of the permanent magnet and the top surface of the magnetic chip, and decreases with increasing separation distance away from this point. The field decreases to zero at a certain distance and then switches direction with a small increase in magnitude. A plateau is followed before it decreased back to zero as the distance increases far enough (not shown). The point at which the field switches direction depends on the separation between the permanent magnet and the magnetic chip. For a slim and long rectangular magnetic, the magnetic field across the magnetic chip in x direction does not vary much along the length of magnet in y direction, i.e., into the paper.

In case the rotation axis of the external magnet is aligned to the normal of the NiFe disc array on the magnetic chip, the discs are always subjected to the peak bias field during the rotation of the magnet and only the direction of the bias field changes with time. As a result, the magnitude of the magnetic force driving a nearby bead around a disc is the same over a revolution. However, if the rotation axis of the magnet was offset from the normal of the NiFe disc array, the separation distance between the discs and the magnet changes within each revolution of the external magnet, leading to periodically

varying strength of the applied field on the discs and the nearby beads. A schematic of the off-centered rotation of an external magnet above a NiFe disc for one revolution is shown in figure 6.2. The external magnet is represented by combined red and blue rectangles to indicate its south and north magnetic poles, respectively. The red arrow on the NiFe disc (green) indicates the direction of the magnetization and the size of the arrow denotes the magnitude of the magnetization.

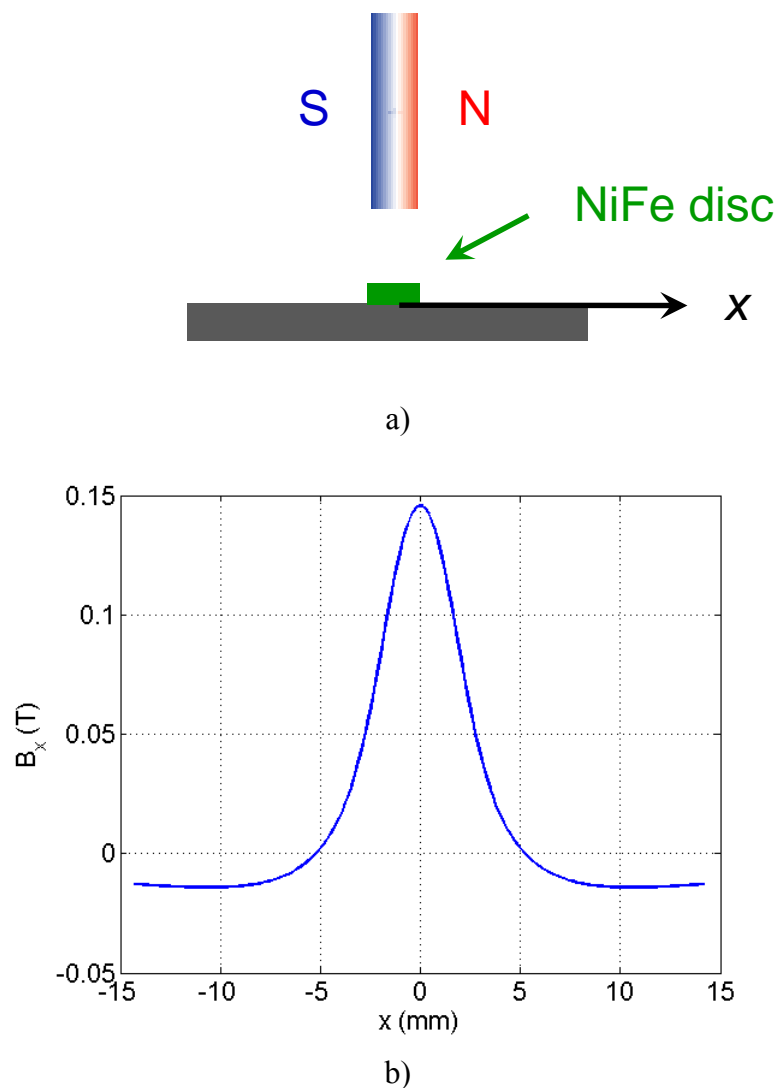


Figure 6.1: a) Side view of a rare-earth magnet sits above a magnetic chip; b) The bias field of the external magnet across the magnetic chip (the pre-magnetization of the magnet is assumed to be 2000 Oe; the separation between the bottom of the magnet and the magnetic chip is 2mm)

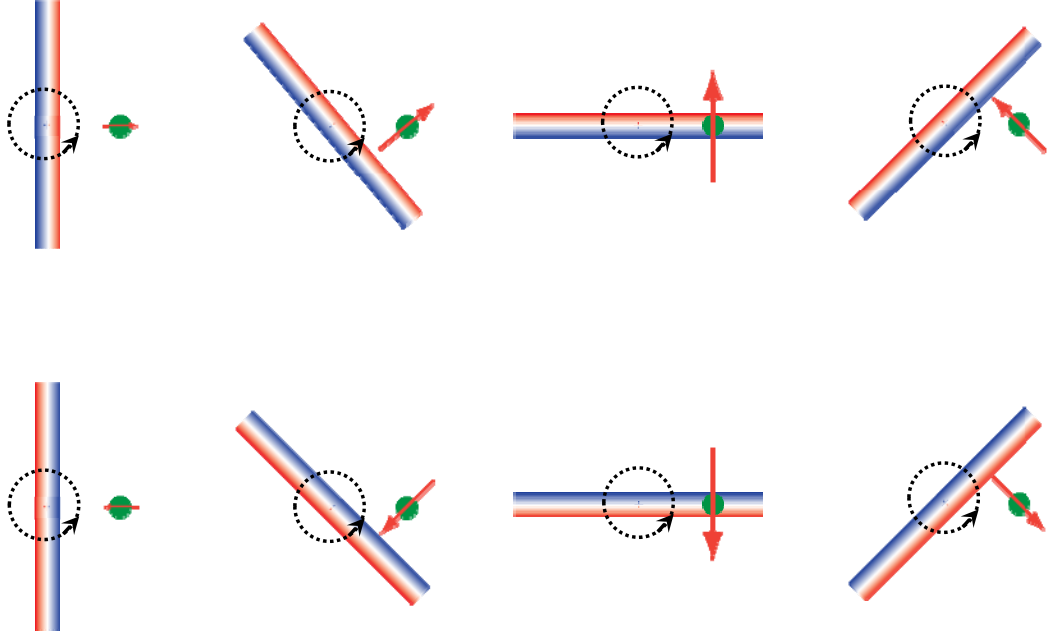


Figure 6.2: A sequence of top-down views of an external magnet (red-blue rectangle) rotating above a NiFe disc (green circle, not drawn to scale) with an offset between the rotation axis of the magnet and the normal of the disc

From the analysis in chapter 5, the system of equations on the force analysis of a magnetic bead circling around a NiFe disc in a rotating magnetic field is given by:

$$F_t(\phi, r, z) = F_d(r, z, \omega) \quad (6.1)$$

$$F_r(\phi, r, z) = mr\omega^2 \quad (6.2)$$

$$F_z(\phi, r, z) = F_h(r, z, \omega) \quad (6.3)$$

where ϕ is the phase lag between the bead and the direction of the bias field, r the orbital radius of the bead, z the orbital height, and ω the angular speed of the external magnet and the bead. With a known magnetic forces as a function of the spatial coordinates, the equilibrium position of the bead (r, ϕ, z) can be determined by simultaneously solving equations (6.1-6.3) for a given ω . However, because the explicit expression of F_h as a function of (r, z, ω) is not available, simultaneously solving the equations is not trivial. In

the discussion to follow, a qualitative analysis on the working principles of the magnetic transport is given.

Among all the variables that describe the equilibrium position of the bead, the orbital radius, r , is of significance for magnetic transport purpose. Meanwhile, among all the forces involved, the radial magnetic force F_r is dominant in determining the orbital trajectory of the bead. From the discussion in chapter 5, within the feasible range of the phase angle ϕ between 0 and $-\pi/4$ (the largest possible lag of the bead if it were to follow the external rotating field), F_r changes from positive (directing outwardly) to negative (directing inwardly) as r increases from the center of the NiFe disc to the center of the gap. We note that, because of the small size of the magnetic beads and the NiFe discs in this study, the required centripetal force $F_c = mr\omega^2$ is relatively small, even at relatively large angular speed, compared to typical magnitude of the radial magnetic force on the bead. For example, $F_c \sim 2.5 \times 10^{-14}$ N for a Dynabead M-280 orbiting around a $3\mu\text{m}$ NiFe disc at $\omega = 1000$ rad/s. The analysis in chapter 5 (see figure 5.7) suggests that the radial magnetic force is usually in the range of pN to nN except in vicinities where the force changes direction from outward to inward. Therefore, the radial magnetic force that satisfies equation (6.2) can be simplified as

$$F_r(\phi, r, z) \approx 0 \quad (6.4)$$

Equation (6.2) and (6.4) together imply that the equilibrium orbital radius r corresponds to the transition point of F_r from directing outwardly to inwardly.

As the bead experiences varying bias field within a revolution around the NiFe disc, the magnetic force on the bead varies as it orbits around the disc. As shown in figure 6.3, as the strength of the bias field increases, the rate of increase of the tangential

magnetic force F_t as a function of phase angle ϕ increases. Therefore, the bead must change its phase lag to a smaller value so it is subjected to the same magnitude of the tangential magnetic force that balances the drag force at a constant rotation speed of the external magnet. In the same time, the radial magnetic force F_r as a function of r increases with increasing bias field and the transition point from directing outward to inward shifts to larger r values, as indicated in figure 6.4. Therefore, with increasing bias field the bead will be pushed outwardly while it orbits around the NiFe disc.

In summary, if the minimum magnetic force within a revolution is strong enough to drive the bead following the rotation of the external magnet at a given ω , the equilibrium position of the bead including the phase angle ϕ , the orbital radius r , and probably the orbital height z , would vary within a revolution. As far as the orbital radius is concerned, an elliptical trajectory of the bead orbiting around the NiFe disc is expected. If the antipodal point of the major axis of the elliptical orbit crosses over the center of the gap between two closest neighboring NiFe discs, the bead will be attracted more by the neighboring disc when it is at the antipodal point. As a result, transport of the bead from one disc to the other can take place. It is based on this theory that we designed our magnetic transport device.

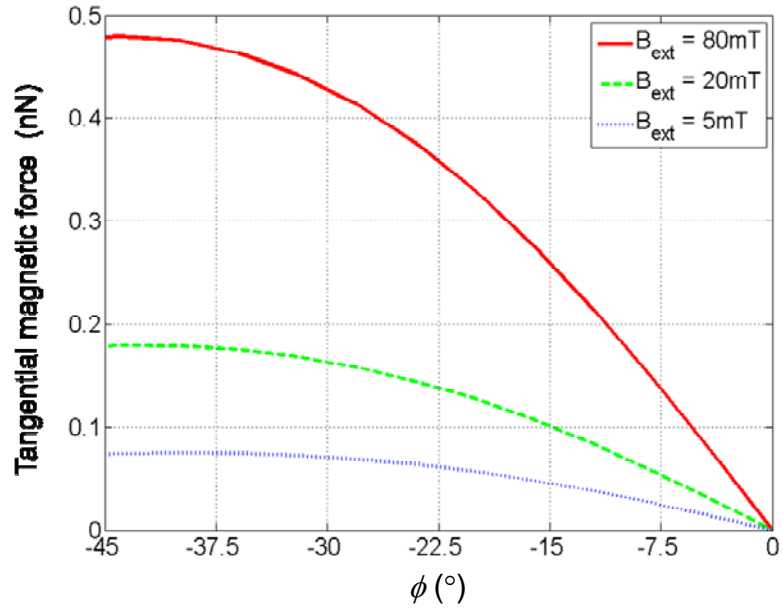


Figure 6.3: Tangential magnetic force on a M-280 bead as a function of ϕ at different bias fields ($r = 2.5\mu\text{m}$, $h = 70\text{nm}$)

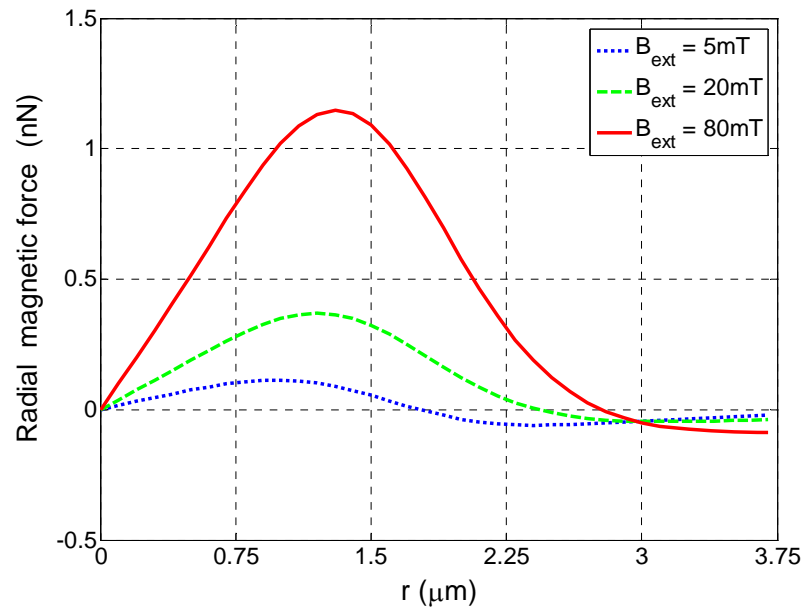


Figure 6.4: Radial magnetic force on a M-280 bead as a function of r at different bias fields ($\phi = 15^\circ$, $h = 70\text{nm}$)

We point out that the diameter of the NiFe discs in the simulation is $3\mu\text{m}$, comparable to the size of targeted magnetic beads, so that we can achieve parallel

manipulation of individual beads. The thickness of the NiFe discs is 150nm, the spacing between the NiFe in both x- and y-directions is 4.5 μ m, and 25 \times 25 NiFe discs in an array were simulated. With an external magnet of 2000Oe sitting 2mm above the magnetic chip, figure 6.1b) implies that the bias field on the chip peaks at <150mT and plateaus at \sim 10mT. Because NiFe material is easily saturated in external magnetic field ($M_s \sim 1$ mT) [130], we assumed that the NiFe discs are always subjected to magnetic saturation, i.e., 660kA/m [130], within a revolution of the off-centered rotation. On the other hand, because $M_s \sim 200$ mT for Dynabeads and is greater than the peak bias field on the chip, we assume the instant magnetic moment of the beads is a linear function of the varying bias field within a revolution of the off-centered rotation, i.e., $\vec{M} = \chi_{eff} \vec{H}_{ext}$, where χ_{eff} is the magnetic susceptibility of the beads. For simplicity, the magnetic force was calculated by treating the magnetic bead as a dipole point at its mass center. In addition, because the size of the NiFe disc array is relatively small compared to that of the external magnet, the magnitude of the external bias field applied to each NiFe disc and every bead inside the microchannel is assumed the same at any instant in time during the rotation.

6.3 Experimental Setup and Device Fabrication

The design of our experiment setup for magnetic transport is shown in figure 6.5. The important feature of this setup is that it allows the translation of the permanent magnet in x, y, and z directions while it rotates. By controlling the x- and/or y-travel of the external magnet, the rotation axis of the permanent magnet can offset from the normal of a NiFe disc array on the magnetic chip fixed on the microscope sample holder.

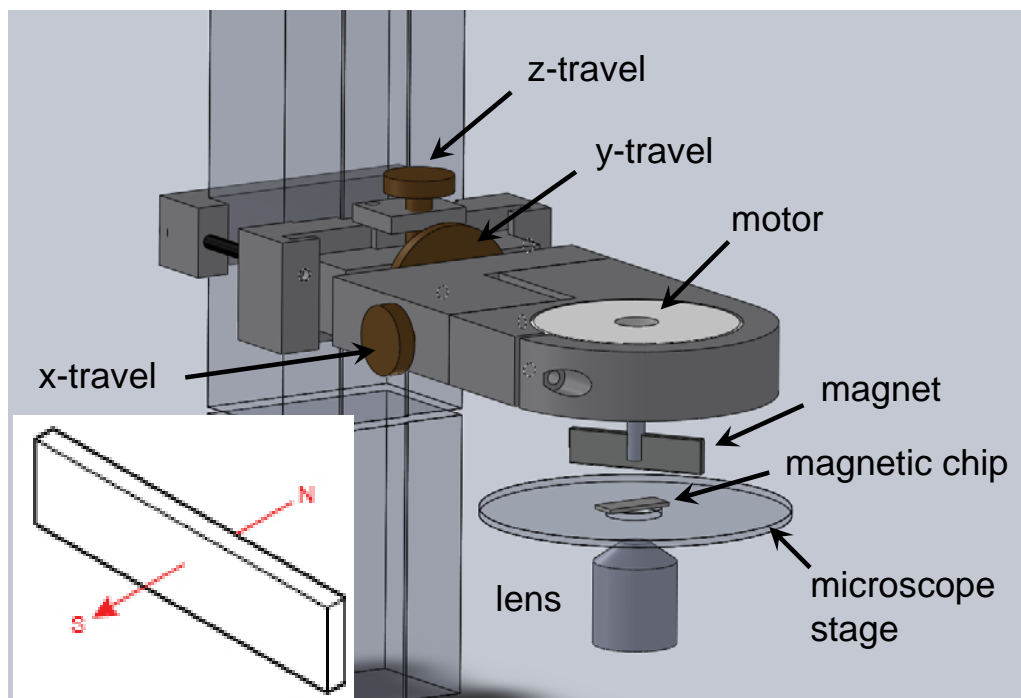


Figure 6.5: Design of a fixture for simultaneous control of the rotation and translation of a permanent magnet (Inset: orientation of the magnetic poles of the permanent magnet)

To realize the transport of magnetic beads, a special magnetic chip was designed to work in combination with the rotating magnet that travels in x or y direction above the chip. As shown in figure 6.6, the magnetic chip consists of a triangular array of $3\mu\text{m}$ NiFe discs. To facilitate the bead transport with a designated path, e.g., across the microchannel, the spacing between the NiFe discs in this direction was set relatively small ($4.5\mu\text{m}$), while that in the other direction, i.e., along the channel, was much larger ($9\mu\text{m}$). The comparable size between the NiFe discs and the targeted magnetic beads M-280 and MyOne was intended to reduce the probability of bead agglomerate on individual discs.

The fabrication of the magnetic chip and the assembly with a PDMS channel, as well as surface treatment of the device, were the same as such discussed in chapter 5 (see

section 5.4). The concentration of Dynabeads M-280 was adjusted to $\sim 1 \times 10^8$ beads per ml, about 5X dilution from the stock solution before each experiment. The concentration of MyOne beads was also adjusted to $\sim 1 \times 10^8$ beads per ml, about 100 times dilution from the stock solution. The mixing of the two bead suspension resulted in a bead mixture with a 1:1 number ratio between the two difference sizes of beads. A syringe pump from Harvard Apparatus (Model HA2000W) was used to load the beads to the magnetic chip through the microchannel. An inverted microscope (Nikon Eclipse TE2000) equipped with a fast speed CCD camera, Phantom v9.1 from Vision Research (NJ, USA), was used to monitor the transport of the beads inside the microchannel through the optically transparent PDMS.

6.4 Experimental Results

6.4.1 Controlled Transport of Microbeads on a Magnetic Chip

Figure 6.6a) shows the random loading of the beads among the NiFe discs on the magnetic chip with the rotating permanent magnet aligned to the normal of disc array. The loading efficiency was controlled to be relatively low by introducing a dilute bead suspension intentionally prepared, so that the transport of the beads can be clearly visualized and easily characterized. The walls of the PDMS microchannel running from left to right in figure 6.6, i.e., in x direction, are not shown. The separation between the magnet and the chip in z direction was ~ 1 mm. As we allowed the rotating magnet to travel across the microchannel from top to bottom in figure 6.6, i.e., in negative y direction, an offset between the rotation axis of the magnet and the normal of the disc array was created. As a result, the orbital trajectory of the beads changed from circular to elliptical. The major axis of the ellipse increased as the offset became larger, and

eventually the beads started to translate from their original ‘host’ discs to the neighboring discs, as shown in figure 6.6b). The direction of the translational motion of the beads was opposite to the direction of the travel of the magnet. The comparison between the figures 6.6a) and b) suggests that the transport of the individual beads took place simultaneously and the rate of transport for each bead was similar, since the original pattern of the bead loading was maintained during the transport process. Figure 6.6c) shows all the beads were transported across the channel as the process continued, and the translation of the beads stopped at the edge of the NiFe array due to the absence of neighboring NiFe discs.

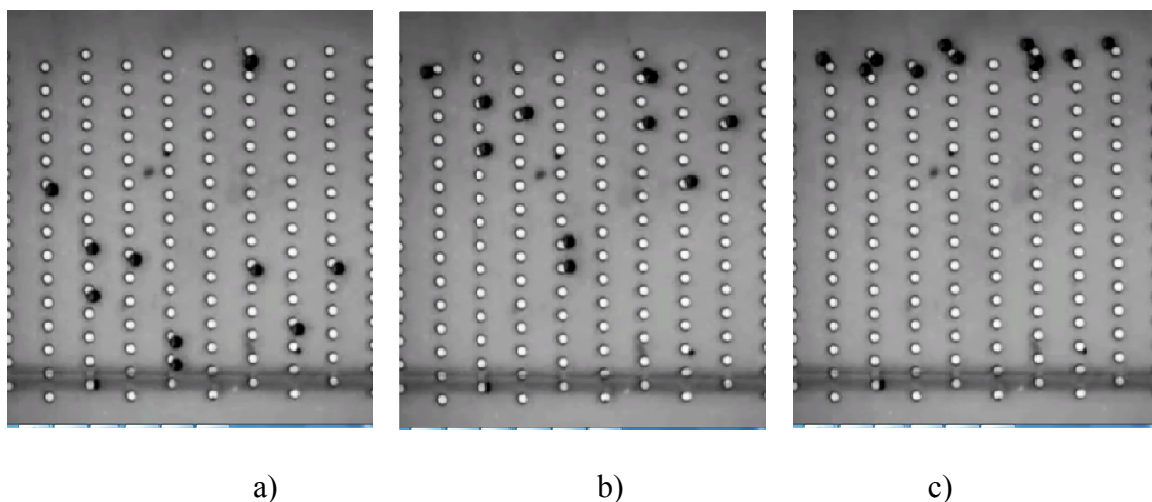


Figure 6.6: Simultaneous transport of individual Dynabeads M-280 on a magnetic chip

We observed that as the beads were transported and stopped at the edge of the disc array, they maintained the orbital motion around individual discs, following the rotation of the external magnet. This observation is illustrated by the different orientation of the beads with respect to the discs in figure 6.6a-c. We infer that the concurrent orbital motion of the beads is necessary for achieving the transport because if we turned off the rotation of the external magnet the transport wouldn't occur.

Figure 6.7 shows that the beads can be transported back and forth across the channel by reciprocal movement of the external rotating magnet in y direction. Initially, the rotation axis of the external magnet offset from the normal of the NiFe disc array with a negative y value with respect to the center of the disc array, leading to the loading of the beads at the y-positive edge of the disc array (figure 6.7a). Then the rotating magnet traveled towards the positive y direction until the offset became positive, and the beads were observed to translate in the opposite direction (figure 6.7b-d). As the rotating magnet traveled back to its original position, the beads were transported back (figure 6.7 e-g). The concurrent circular motion of the beads while they translated is indicated by the different angular location of the beads at different NiFe discs along the transport path.

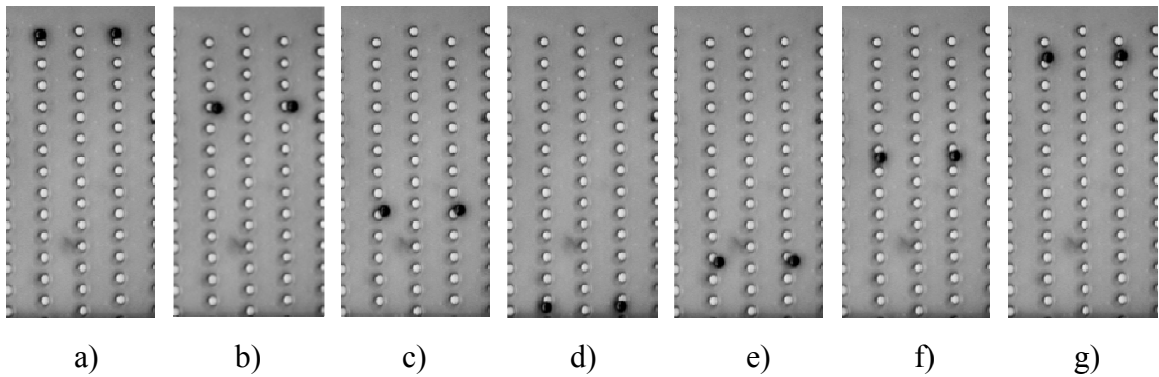


Figure 6.7: Snapshots of two M-280 beads be transported back and forth across the microfluidic channel

The transport rate of the beads on the magnetic chip was observed to strongly correlate to the rotation speed of the external magnet and the offset distance between the rotation axis and the normal of the disc array. With the same offset distance, faster rotation of the magnet results in faster transport rate of the beads. Similarly, with the same rotation speed, larger offset leads to faster transport rate. The travelling function of the external magnet was controlled by macroscale thumb screws in our system, therefore,

precise control of the travel speed and offset distance was not very easy. With a rough estimation of offset distance while the magnet rotating at 1000 rpm travels, we observed that the transport of the beads initiated at an offset distance about 1mm, and the transport rate increased to $\sim 1\text{mm/sec}$ as the offset distance became $\sim 3\text{mm}$. We also observed that the cross-channel transport of the beads was not affected by a continuous flow along the channel at an average flow speed of 0.5mm/sec .

The magnetic transport of microbeads on a chip while retaining the beads inside the channel against a continuous flow can find many applications in lab-on-a-chip systems. For example, it can help increase the population of beads on a dense array of the NiFe discs, and uniformly distribute the beads across the channel during the loading stage. As discussed in chapter 4 and reported by Doyle et al. [162], in a passive magnetic capture/assembly system with soft magnets subjected to a static external field, the load efficiency and population density in the soft magnet region strongly depends on the concentration of the bead suspension being injected into the microchannel. With dilute bead suspensions that are applicable in most applications, the loading efficiency is usually low and beads are mostly populated in the center area of the microchannel. Actively transporting the beads captured by the soft magnets on the magnetic chip in x- and y-directions during the loading stage can dramatically improve the population density and distribution uniformity. In addition, the synchronized orbital motion of the beads exposes the bead surface with more opportunities to interact with the fluid flow than the case for statically trapped beads. Such a condition is desired in sample preparation and detection in which maximum contact between the analyte and the bio-active coating of the beads is required.

6.4.2 Size-dependent Sorting of Magnetic Beads on a Chip

Before we discuss the experimental result in this section, we first differentiate the meaning of magnetic separation in this context from the conventional meaning. In the conventional magnetic separation, magnetic beads are separated by the action of a magnetic field from the flow, but are transported using a liquid flow. In magnetic transport-based separation, magnetic forces selectively transport different groups of beads to specific locations to accomplish the bead separation or sorting. The latter is a bigger challenge because it requires magnetic forces that act on a larger range than necessary for conventional separation. The unique transport mechanism discussed before can be utilized for the size-dependent separation of magnetic beads on a chip.

From the analysis in section 6.2, the elliptical trajectory of the beads orbiting around the NiFe discs under the off-centered rotation of the external magnet was formed due to the varying radial and tangential magnetic forces within a revolution. Because the magnetic force scales with the volume of the beads, smaller beads will experience significantly smaller tangential and radial magnetic forces on the same magnetic chip with the same external field. As a result, the major axis of their elliptical trajectory will be much shorter than that of the larger beads orbiting around the same NiFe discs. We note that the minor axis will be similar for small and large beads as it is determined by the size of the disc. The transport of the beads can only occur if the antipodal point of the major axis of the elliptical orbit crosses over the center of the gap between two neighboring NiFe discs. Therefore, this transport mechanism can be employed for the size-dependent separation of the beads on a chip.

To prove this concept, a bead mixture consists of Dyanbeads MyOne and M-280 was loaded to the magnetic chip. With a y-negative offset between the rotation axis of the

magnet and the normal of the disc array, both MyOne and M-280 beads were loaded at the y-positive edge of the disc array (figure 6.8a). As we allowed the rotating magnet to travel towards the positive y direction and created y-positive offset, the larger beads (M-280) started to translate towards the opposite edge of the channel, while the smaller beads (MyOne) remained orbiting around their original host discs (figure 6.8b). On completion of the selective transport process, the originally mixed beads were divided according to their size and grouped at the opposite edges of the NiFe disc array across the microfluidic channel (figure 6.8c).

The ability of our device to separating the beads on a chip can be utilized for on-chip bioseparation, provided different groups of beads are specifically functionalized to immobilize different biological substances such as cells and subcellular entities. On-chip separation of biological samples will significantly facilitate the *in-situ* detection of multiple analytes.

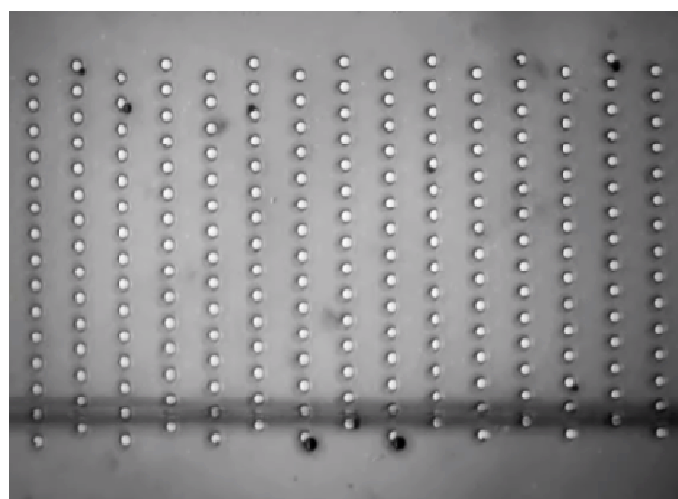
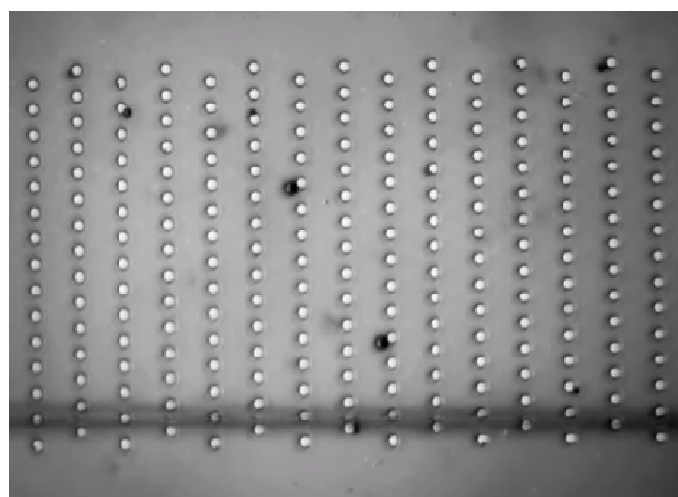
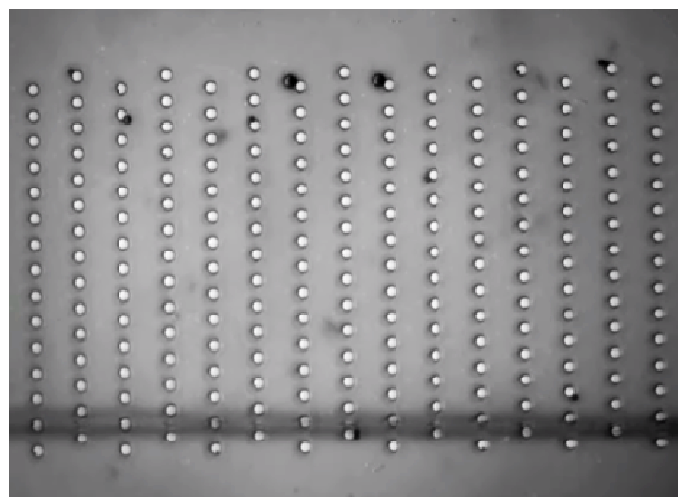


Figure 6.8: On-chip separation of Dynabeads M-280 from Dynabeads MyOne

6.5 Discussion

The advantages of our magnetic separation method include the following. First, most separation techniques need to deal with the non-specific adhesion between the target and the surface of the separation devices, while in our approach this is not a problem because the continuous motion of the beads during the separation process minimizes the chance of physical contact between the beads and the surface. Second, the smaller spacing between the discs in y direction (across the channel) than in x direction (along the channel) in our devices resulted in the preferential transport across the channel, even if the travel direction of the external magnet was not precisely aligned in the y direction. Therefore, one can easily modify the current design in order to produce a preferential transport along the channel or at an inclined angle with the wall of the channel. In addition, we believe more interesting transport path such as zigzag shape can be realized by controlling the travel path of external rotating magnets. Third, by reducing the spacing among the NiFe discs and using smaller NiFe discs, our approach can be used to separate smaller magnetic particles. The limitation with other separation techniques for nanoparticles was reportedly related to the significant Brownian motion that critically decreases the specificity of the separation [42]. In our system, the Brownian motion of the magnetic nanoparticles would be suppressed by dominating magnetic forces in the system, thus eliminating the time-dependent displacement away from their designated location.

In chapter 5, we discussed that without the presence of the NiFe discs, magnetic beads spin around their own center by following the rotation of the external magnet. In the current study, we further observed that a translational motion of the spinning beads can be also induced when the rotating external magnet travels in the x-y plane. To the

contrary of the translational motion of the beads orbiting around the NiFe discs, the spinning beads follow the travel direction of the external rotating magnet. This phenomenon can be explained by the existence of a time-averaged field gradient due to the offset between the rotation axis of the external magnet and spinning beads. In comparison, the translational motion of the beads across an array of NiFe discs opposite to the travel direction of the rotating magnet seemed counter-intuitive. However, our previous discussions suggest a completely different transport mechanism. With the presence of the NiFe discs, the local field and field gradient are much stronger and complicated than without. Therefore, the time-averaged field gradient from the external field itself does not play important role any more. We note that in the absence of the NiFe discs, the translational motion of spinning beads under the traveling, rotating field is very slow ($\sim\mu\text{m}/\text{sec}$) due to the small gradient of the time-averaged field, and the translational motion is easily affected by incoming flow. In contrast, the transport rate of beads across the NiFe disc array is remarkably faster at the same traveling speed of the external rotating magnet and the beads can be retained on-chip by the NiFe discs against moderate flow in the microchannel.

Our mathematical model and numerical simulations presented in section 6.2 do not suggest whether the translation of the beads across the NiFe disc array follows or opposes the travelling direction of the external rotating magnet. It is possible that the present model has omitted some relevant forces in the system, particularly along the radial direction. For instance, we didn't include the spinning of the bead about its body center while orbiting around the NiFe disc. Because both spinning and orbiting are caused by the rotation of the external magnet, the two motions have the same

sense/direction according to the right-hand rule. It is possible that the spinning of the bead in the same direction as the orbiting of the bead leads to the translation of the bead in the opposite direction in which the external magnet travels. In addition, the fact that there is a small step between the top surface of the NiFe disc and the substrate may produce some complicated hydrodynamic pressure that affects the motion of the bead while it orbits around the disc.

CHAPTER 7

Out-of-plane Motion of Microbeads Using Combined Magnetic and Dielectrophoretic Manipulations

7.1 Motivations

In terms of particle handling, either physically positioning the particles to a designated locations or steadily transporting them relative to the device within which they reside, the fundamental requirement is that the net force on the particles is zero. Additionally, the particles must be at a stable zero, i.e., they must do work to move from that zero [163] (pp. 710). In most electrical and magnetic manipulations such as electrophoresis (EP), positive dielectrophoresis (pDEP), and magnetophoresis (MAP), a restoring force from a rigid surface is needed to create a stable holding point for any deterministic particle trap. Similarly, forces required to steadily transport the particles relative to the device is often balanced by fluid drag or gravity force. To stably hold the particles away from the device surface, potential energy wells must exist above the surface. In the situation of negative dielectrophoresis (nDEP), electrical potential energy wells are created at electric field minima away from the electrode surface, hence it can deterministically trap the particles in solution in which the particle is suspended without additional forces [164].

The motivation of this work was to integrate a particle trap on a surface due to magnetophoresis with a particle trap above the surface due to negative dielectrophoresis, thereby achieving out-of-plane motion of the beads. Two different bead manipulations will be investigated: oscillation across the channel height and high-resolution tweezing in liquid. If the two traps are alternatively switched on and off, a particle can oscillate

between the two traps across the channel height. On the other hand, if both traps are activated, the particle can be held at an arbitrarily position between the two traps. By fine-tuning the competing MAP and nDEP forces on the particle through external control of the strength of the magnetic and electric fields, one can control the equilibrium positions of the particle with high spatial resolutions.

With the competing magnetic and DEP forces on the bead, one can always apply sufficiently large magnetic and DEP forces and still result in a small net force for high-resolution bead tweezing. This unique feature prevents the size effect such as the Brownian motion from imposing a physical limitation on the spatial resolutions of the tweezers, because the Brownian motion can be suppressed by applying dominant magnetic and DEP forces to the beads. Previous work has demonstrated that the magnitude of DEP force on small particles and even DNA macromolecules can be sufficient to overcome the diffusion barrier due to Brownian motion [109]. Our study presented throughout this thesis suggests that magnetic energy of small beads can be orders of magnitude greater than their thermal fluctuation energy $k_B T$, particularly when the beads are located close to the surface of magnetic elements. Therefore, how much our tweezers move the particle from one equilibrium position to another is only limited by the technology that can be used to apply the control signals. Current electronic instruments offer extremely high precision already, therefore promising high spatial resolution of the proposed tweezers.

In order to combine MAP and nDEP for particle handling, the particles need to have both magnetic and dielectric properties. As discussed in chapter 2, Dynabeads[®] offer both properties because they are made of polystyrene matrix (dielectric) with doped

iron oxide nanoparticles (superparamagnetic). For proof-of-concept studies, Dynabeads[®] M-280 (2.8 μ m) was chosen in this work. Although soft magnets do not pose Joule heating issue, electromagnet based on conducting wires was chosen in this work because it has the advantage in precise adjustment of the field strength and easy integration with DEP electrodes.

7.2 Theoretical Analysis and Device Design

7.2.1 DEP Force

In order to estimate the DEP force on Dynabeads[®] M-280, it's important to know the permittivity and conductivity of the medium in which the beads are suspended in an actual experiment. A typical medium for Dynabeads with biological derivatization on their surface is phosphate buffer saline (PBS) solution. The composition of this buffer solution includes 137mM NaCl, 2.7mM KCl, 10mM Na₂HPO₄, and 1.8mM KH₂PO₄ dissolved in DI water. At pH = 7.4, the conductivity of the PBS measured about 1.6S/m by a conductivity meter (Yokogawa Model SC72). The permittivity of the solution can be approximated by the permittivity of water, i.e., $\epsilon = 80\epsilon_0$. In the same time, the conductivity and permittivity of polystyrene are $\sim 2 \times 10^{-4}$ S/m and $2.4\epsilon_0$, respectively. Therefore, the real part of the Clausius-Mossotti factor is negative at both low frequency limit and high frequency limit (see figure 2.5). Thus, the DEP force on Dynabeads[®] in PBS buffer will be repulsive regardless of the field frequency. The theoretical value of $\text{Re}\{f_{CM}(\omega)\}$ is about -0.5 at both frequency limits. The theoretical nDEP force on an M-280 bead can be calculated once the value of ∇E_{ms}^2 is known from computer simulation for a given design of the DEP electrodes and the electrical signals applied to them.

7.2.2 MAP Force from Conducting Wires

Due to the limitation of Joule heating, the magnetic field strength from miniature conducting wires is relatively small, compared to that from a soft magnet. However, it is convenient to precisely adjust the magnetic field using the current-carrying wires. In addition, magnetic field from different sets of current-carrying wires in an array can be selectively activated and deactivated by controlling the current input signals.

In the case of an array of conducting wires with the fields from different wires overlapping, the fields influence each other due to the vector nature of the magnetic field. The superposition of the fields determines the overall field strength in space. Because the field from each wire is oriented around the circumference of the wire according to the right hand rule, the superposition of the fields from different wires either enhances the field at specific locations or cancels it at other locations depending on the direction of the current in the wires. Thus, the field and field gradient among a wire array can also be adjusted by configuring the direction of the current flowing through the wires. In order to find out the dependence of field and field gradient on the geometry and layout of a wire array as well as the configuration of the current, a computer simulation is required. The resultant field and field gradient give rise to the magnetic force on a nearby magnetic bead.

For a conductor with rectangular cross-section, Derec and Wilhelm [165] derived and experimentally showed that:

$$B = f \frac{\mu_0 I}{2\pi(a + y)} \quad (7.1)$$

where f is the pre-factor and depends on the exact geometry of the conductor, y is the distance away from the conductor and a the equivalent radius of the rectangular

conductor. As a result of this empirical relationship, the magnetic force on a magnetic bead is given by

$$F_M = f^2 \frac{\chi_{eff} \mu_0 R^3 I^2}{3\pi(a+y)^3} \quad (7.2)$$

This analytical result is used to verify the numerical simulations to be carried out during the device design stage.

7.2.3 Design of Integrated MAP-DEP Devices

The key component in designing the integrated nDEP-MAP device for out-of-plane manipulation of Dynabeads[®] is the spatial arrangement of the conducting wires and the electrodes for magnetic and electric field generation. Both the magnitude and the gradient of the two fields should be designed in such a way that when changing the strength of one of the fields the net force on the beads directs normal to the device surface or along a predictable direction. One such design is given in figure 7.1.

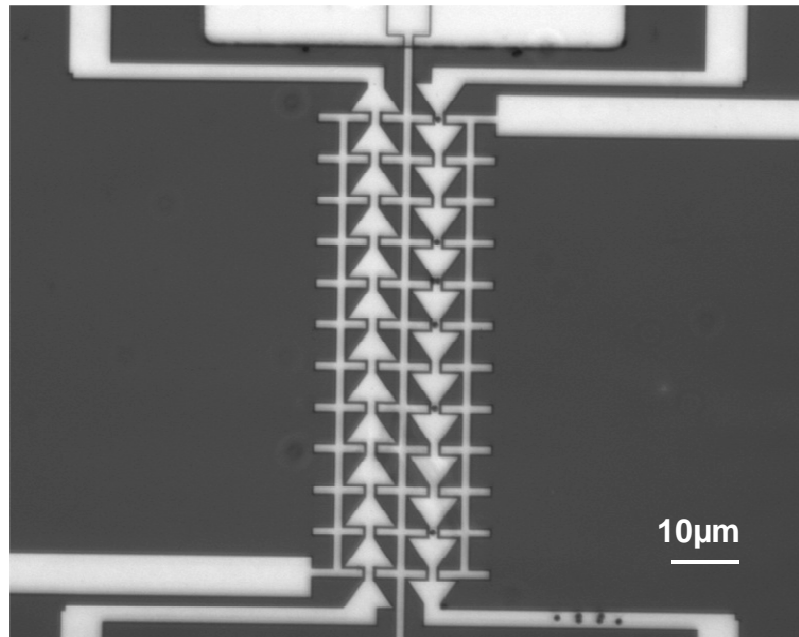


Figure 7.1: A prototype nDEP-MAP device

The conducting wires were designed with tapered dimensions so that the current density is larger at the narrower sections ($2\mu\text{m}$) of the conductor, leading to larger magnetic field and field gradient at these locations. This design was intended to localize the magnetic beads to the narrow sections, i.e., magnetic traps, of the conductor. In the same time, the fingered electrodes would produce larger electric field and gradient at the finger tips due to the smaller spacing ($3\mu\text{m}$). For nDEP, these locations will provide strongest repulsive force. We refer the narrow conductor sections between a pair of electrode finger tips as the matching locations for maximum forces. Due to the symmetry of the fields, a particle at the matching locations would experience both forces in the normal direction.

COMSOL AC/DC Module was used to study feasibility and performance of the prototype device. For simplicity, a 2D model on the cross-section of the device across the conductors and electrodes along the matching locations was carried out. Quasi-static-electric module with in-plane electric currents was chosen for the electric field simulation and static-magnetic module with perpendicular induction current and vector potential for magnetic field simulation. The thickness of the conductor and the electrodes is assumed to be $0.5\mu\text{m}$. Both DEP and magnetic forces were calculated by treating the M-280 bead as a dipole point at its mass center. The numerical simulation results (figure 7.2) suggest that 50mA current input to the conductors can generate a magnetic attraction force in the order of 240pN if the M-280 bead sits close to the matching locations. Meanwhile, electric potential 5V peak-to-peak applied to the electrodes can repel the bead from the matching location with an nDEP force of similar magnitude. Forces in this range can

introduce a speed of the 1cm/sec of the M-280 bead in water (see the discussion in chapter 2).

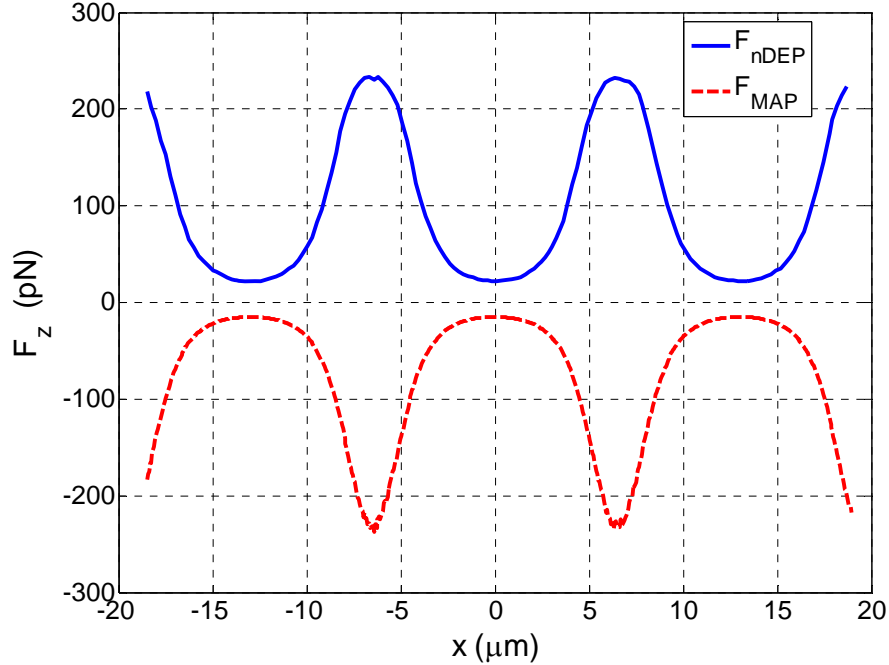


Figure 7.2: Theoretical magnitude of nDEP and MAP forces on an M-280 bead ($z = 2\mu\text{m}$ above the device surface)

In figure 7.3, the magnitude of both MAP and DEP forces on an M-280 bead as a function of the separation distance between the beads and the surface of the matching location is shown. The positions where the two forces intersect is the equilibrium positions of the bead. From this result, by applying 15mA current to the conductors and 1.5V peak-to-peak to the electrodes, the equilibrium position is at $z = 1.45\mu\text{m}$, which implies that the bead will be held at 50nm above the surface of the matching location (recall bead radius $R = 1.4\mu\text{m}$). It is straight forward that different combination of the signals can result in the same equilibrium position of the bead. For instance, the simulation suggests that 50mA current in the conductors and $5V_{pp}$ on the electrodes can also hold the bead at 50nm above the surface.

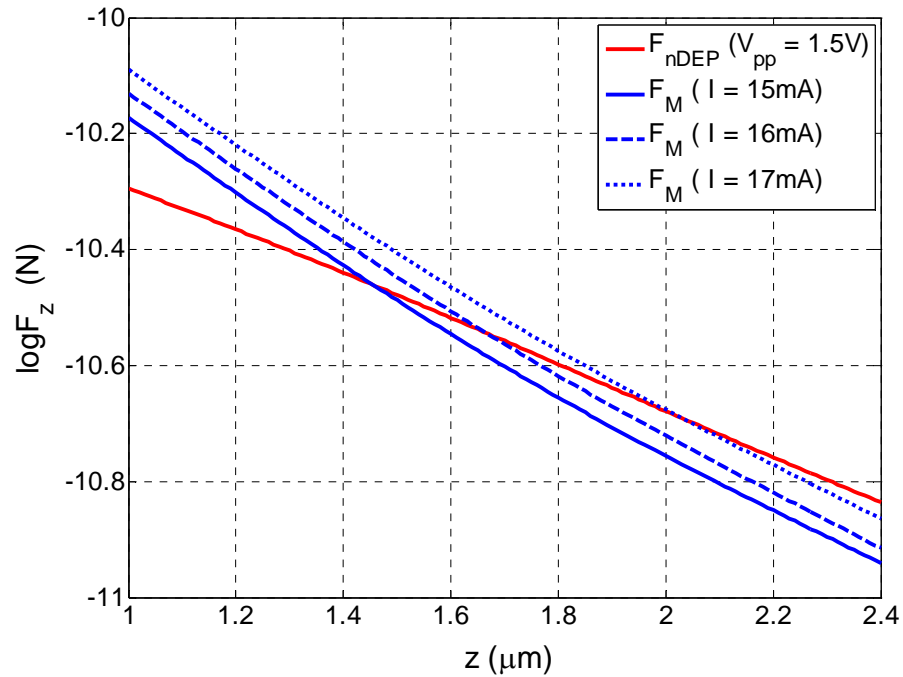


Figure 7.3: Theoretical prediction of the equilibrium positions of an M-280 bead under different control signals
 (We note different sets of control signals can be used to produce similar control of the bead position and displacement.)

By increasing the current in the conductors from 15mA to 16mA and then to 17mA while holding the potentials on the DEP electrodes the same, one can expect to increase the separation from 50nm to 250nm and then to 650nm. The disproportional change of separation distance with increasing current is expected due to the exponential decrease of the DEP and magnetic forces with increasing separation of the bead from the substrate. We note that the DEP force decreases slower with increasing separation than the magnetic force does. Thus, the same incremental force from adjusting the electrical field would produce smaller displacement of the bead than from adjusting magnetic field.

7.3 Experimental

The fabrication of the nDEP-MAP device on a silicon wafer followed the standard procedure of lithography, e-beam evaporation, and lift-off. The thickness of the conducting wires and DEP electrodes is $0.5\mu\text{m}$. The comparable size among the finger tips of DEP electrodes, the narrow sections of the conducting wires, and the Dynabeads M-280 was intended for individual bead manipulation.

After dicing the batch fabricated nDEP-MAP devices from the silicon wafer, PDMS channels with $20\mu\text{m}$ in height and $100\mu\text{m}$ in width were assembled onto individual devices. The concentration of Dynabeads M-280 was adjusted to $\sim 1 \times 10^8$ beads per ml, about 5 times dilution from the stock solution, and re-suspended in PBS buffer before each experiment. A syringe pump from Harvard Apparatus (Model HA2000W) was used to load the beads to the nDEP-MAP chip. An inverted microscope (Nikon Eclipse TE2000) equipped with a CCD camera (Photometrics CoolSNAP HQ2) was used to monitor the motion of beads through the optically transparent PDMS microchannel.

7.3.1 Out-of-Plane Oscillation of Microbeads

The experimental setup for realizing out-of-plane oscillation of microbeads on a chip is shown in figure 7.4. A DC power supply with two outputs was used to apply constant current to the two conducting wires for magnetic field generation. A function generator was used to supply high-frequency signal to the DEP electrodes. Both the DC power supply and the function generator were connected to a house-made multi-waveform modulator (figure 7.5a).

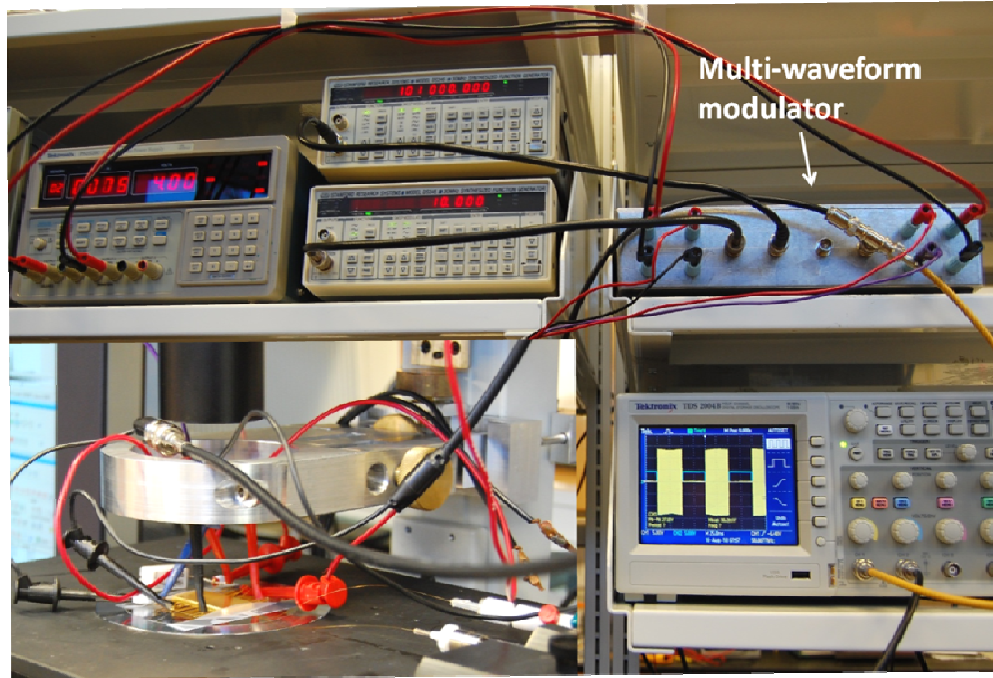
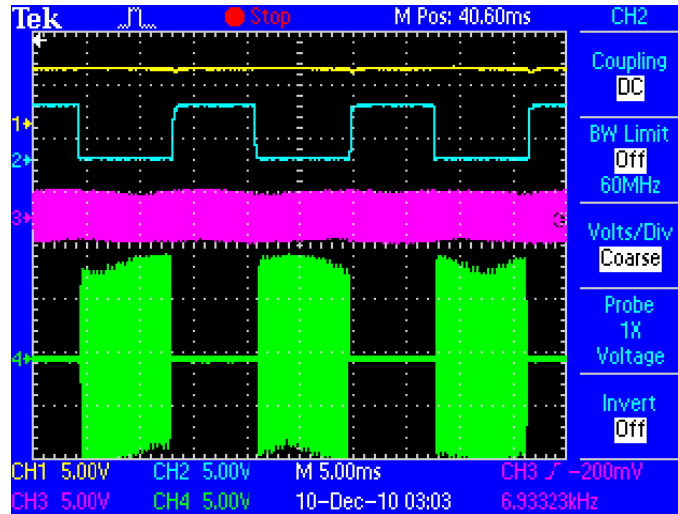


Figure 7.4: Experiment setup for nDEP-MAP manipulations

As shown in figure 7.5b), with an input of a triangular waveform from a separate function generator, the modulator converts the constant DC signal (channel 1) to a square wave (channel 2) and the continuous AC signal (channel 3) with an on-off sequence (channel 4) that synchronously alternates with the square wave. Therefore, the output signals from the modulator applied to the nDEP-MAP device can alternately switch on and off the electric and magnetic fields. The switching frequency is controlled by the frequency of the triangular waveform from the second function generator. The block diagram of the multi-waveform modulator is presented in Appendix B.



a)



b)

Figure 7.5: a) A picture of the multi-waveform modulator; b) Demonstration of the function of the multi-waveform modulator

With the electric and magnetic fields alternately switched on and off in the NDEP-MAP device, Dynabeads M-280 loaded to electrode and conductor region inside the microchannel experienced alternating nDEP and MAP force. Figure 7.6 shows, when the magnetic field was switched on with a 50mA current passing through the conductor, the M-280 beads were attracted to the conductor by magnetic force. As expected, most of

the beads localized at the narrow sections of the conductors. In this experiment, we activated only one of the two conductors for demonstration purpose and used the inactive conductor as a control. As the magnetic field switched off and the electric field switched on with a 5V, 2MHz signal on the DEP electrodes, the beads were repelled away from the tips of electrode pairs, i.e., the narrow sections of the conductors and the DEP/MAP matching locations. The fact that the beads became out of focus indicates that they were levitated from the bottom surface of the microchannel, and by refocusing the beads we estimate that they have reached the top surface of the microchannel, i.e., 20 μ m away from the bottom surface. The distribution of the beads while they were repelled to the top surface of the microchannel suggests that the nDEP energy wells locate above the narrow sections of the electrodes and separated by the fingers of the electrodes. The distance between the centers of the narrow sections of the conductor and that of the electrode is 9 μ m, leading to an average lateral movement of the beads of 9 μ m while they were levitated from the bottom to the top surface of the channel.

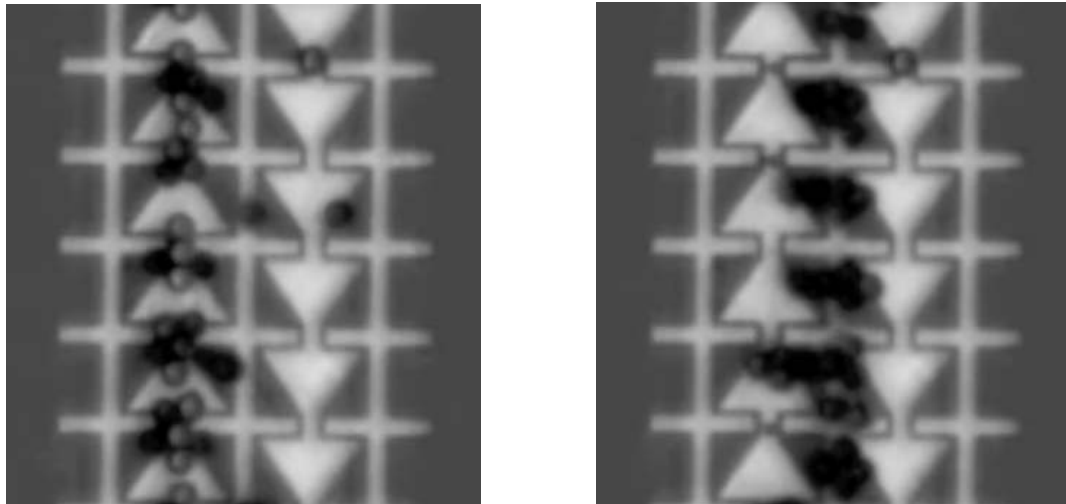


Figure 7.6: Dynabeads M-280 attracted to the conductor by MAP (left) and repelled to the top surface of the microchannel by nDEP (right)

With the 50mA and 5V_{pp}, 2MHz signals, we increased the switching frequency from 1Hz up to 100Hz, and the beads were observed to oscillate at the same frequency. Beyond 100Hz, the oscillation amplitude started to decrease, implying that the critical switching frequency was reached. We note that the oscillation frequency can be increased by using larger electrical current and potential for stronger magnetic and electric fields, respectively. In addition, the speed of the beads moving upward and downward can be independently adjusted by changing the strength of the electric and magnetic fields separately.

The nDEP force on the M-280 beads in the PBS buffer was obvious in a range of frequency from ~1M to ~15MHz, and not observed outside of this range both below and above up to 30 MHz. In theory, we expect the nDEP force in the same order of magnitude over all frequency range (see discussion in section 7.2.1). We attribute this discrepancy to the facts that beads are not made by pure polystyrene, but a composite with fillings of iron oxide, and that the beads were coated with a thin layer of different

polymers (see figure 2.1) and streptavidin molecules in this batch. These facts would result in a very different complex permittivity including the frequency dependent conductivity, and require a multilayer model of the beads in DEP force analysis.

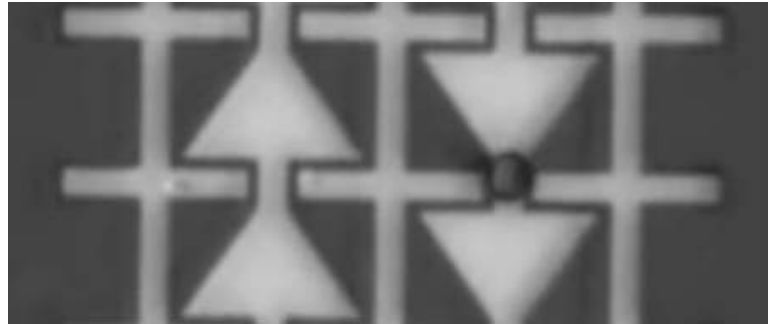
The out-of-place oscillation of the beads across the channel height can be employed for bead interaction with multiple layers of flow streams arranged from top to bottom of a microchannel.

7.3.2 High-resolution Tweezing of Microbeads

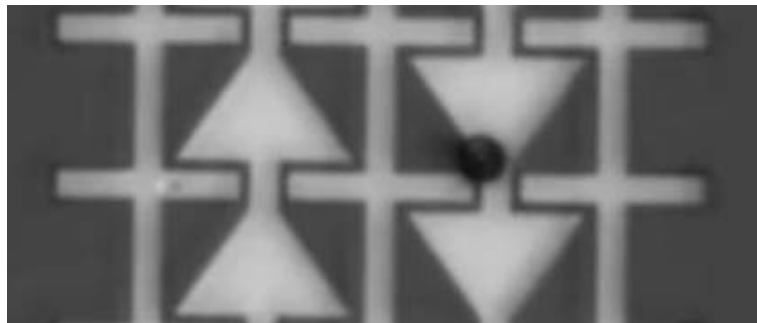
The same experimental setup shown in figure 7.4 can be utilized for high-resolution tweezing of the microbeads in liquid. Instead of separately switching the electric and magnetic fields on and off, both fields are simultaneously switched on during the tweezing experiment. As a result, the competing MAP and nDEP forces on a nearby bead will balance at some point in liquid between the magnetic traps at the narrow sections of the conductors and nDEP energy wells above the narrow sections of the electrodes. Because the two forces can be adjusted by changing the strength of the electric and magnetic fields independently, one can move the bead from one equilibrium position to another. The displacement of the bead can be controlled by the amount of electric current or potential changed during the experiment.

In figure 7.7, about $3\mu\text{m}$ levitation of the bead originally held on the surface of the narrow sections of the conductor is shown. The movement of the bead was realized by increasing the current in the conductor from 15mA to 20mA, while holding the potential on the DEP electrodes at $1.5V_{pp}$. The height of levitation was estimated by comparing the recorded optical images with an image map of the same bead (figure 7.8), created as a reference library for calibration purposes. A numerical algorithm was used to

calculate the cross-correlation coefficients to find the closest match between the recorded images with the calibrated heights. We confirmed that the bead was originally on the surface by reducing the current below 15mA and no downward motion was observed.



a)



b)

Figure 7.7: Bead tweezing with a large step, i.e., $\sim 3\mu\text{m}$ levitation from a) to b)

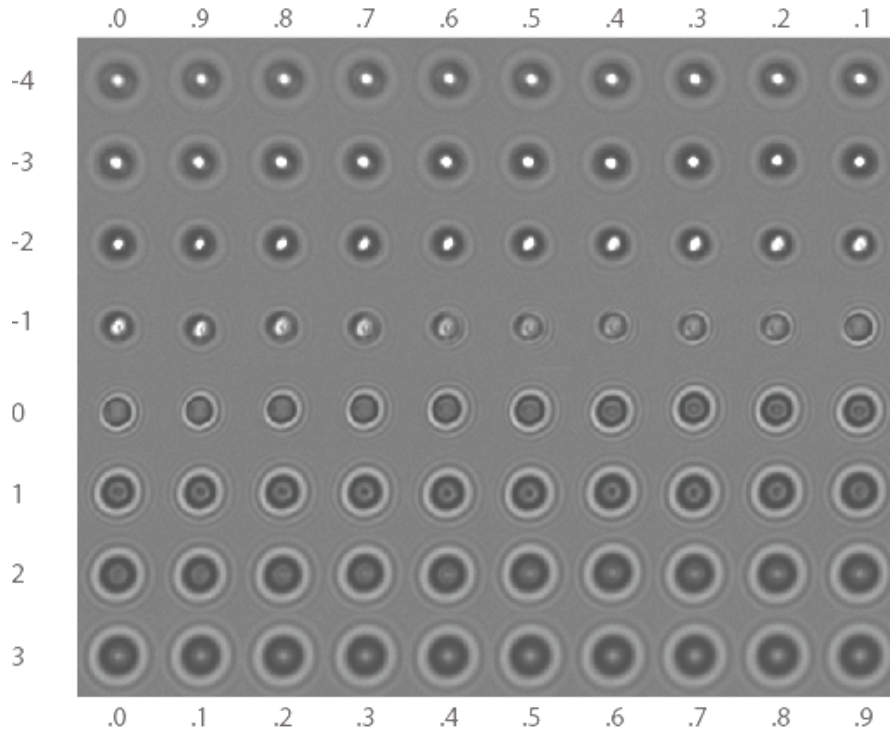
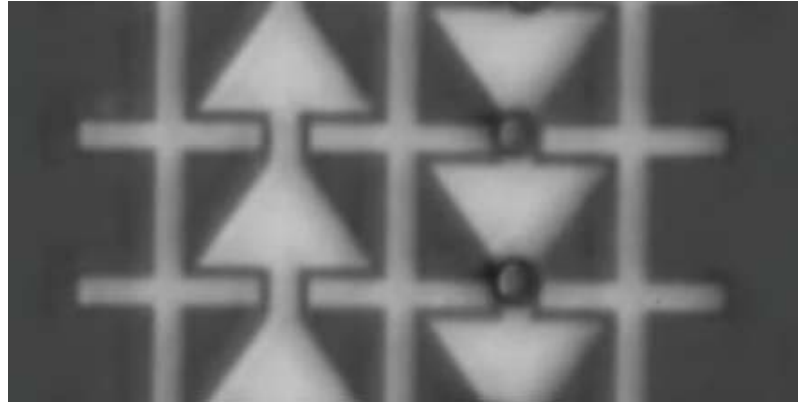


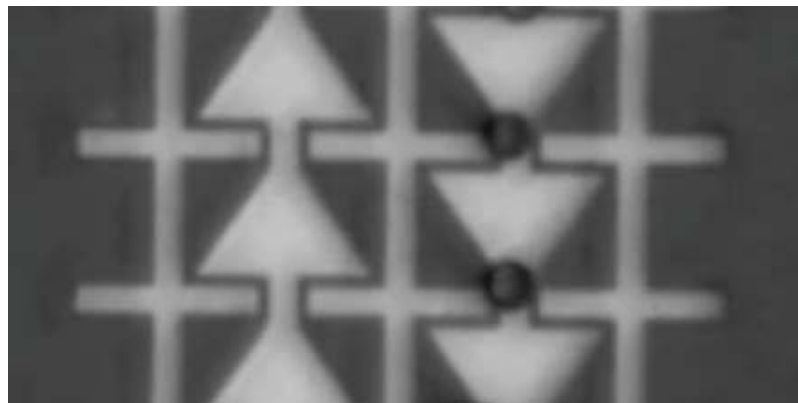
Figure 7.8: Image map of an M-280 bead at different height above a surface (Unit on both axes: μm)

In figure 7.9, levitation of two beads in parallel was demonstrated. In addition, by changing a small amount of the electric potential or the current in the device, high spatial resolution of bead tweezing in solution was realized. The out-of-plane displacement of the beads from figure 7.9a) to b) is $\sim 0.5\mu\text{m}$, controlled by increasing the current in the conductor from 15mA to 16mA, while holding the potential on the DEP electrodes at $1.5V_{pp}$. This experimental result agrees very well with the theoretical prediction on the bead displacement under the same change of current input (see figure 7.3). We note that the tweezers can move the beads at much finer steps by adjusting the current with a much smaller increment with a precision power supply. However, with the optical height detection technology offered by our current system, it is very challenging to observe the motion of the beads from one equilibrium position to another with a displacement below

0.5 μm . A better optical microscope system or a different technique such as atomic force microscope is required to calibrate the nDEP-MAP tweezers at nanoscale resolutions.



a)



b)

Figure 7.9: Bead tweezing with a small step, i.e., $\sim 0.5\mu\text{m}$ levitation from a) to b)

From both figures 7.7 and 7.9, we note the concurrent lateral movement of the bead while it was tweezed out-of-plane. This result is due to the inherent characteristics of the two dimensional layout of the conductors and the electrodes, which results in a lateral offset between the magnetic trap on narrow sections of the conductor and the nDEP trap above the narrow sections of the electrodes. The consistent direction of the

lateral movement was caused by the non-symmetric pattern of the triangular conductor that results in non-symmetric magnetic field above the narrow sections of the conductor.

7.4 Discussion

The MAP-nDEP device presented in this work can be used as a new type of bead-based biomolecular tweezers. A proposed MAP-nDEP biomolecular tweezers is schematically shown in figure 7.10. In this design, DC electromagnetic field-based MAP attraction and AC electric field-based DEP repulsion are simultaneously applied. Because the two forces can be independently adjusted by changing the strength of the electric and magnetic fields, the equilibrium position of the microbead can be controlled at a point very close to the surface, so as to facilitate the biomolecular interaction between, e.g., the antigen bound to the bead surface and the antibody immobilized on the surface of the chip. Then, one can adjust either the DC signal to reduce the magnetic attraction force or the AC signal to increase the DEP repulsion force to introduce a net upward force on the bead. As a result, the bead will move upward and apply a force to the molecular bonds.

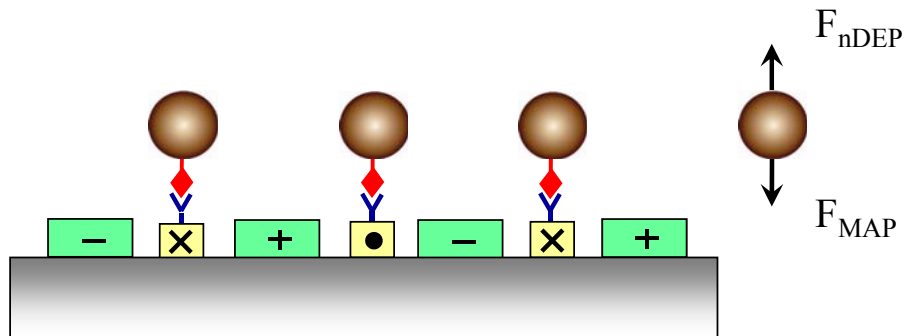


Figure 7.10: Conceptual design of MAP-nDEP tweezers for parallel tweezing of antigen-antibody bonds

Because spatially periodic electric and magnetic fields can be easily configured by arraying microelectrodes and conducting wires, massively parallel nDEP-MAP

biomolecular tweezers can be realized on a single chip. Therefore, the capability of high throughput adds to the aforementioned advantages of this new biomolecular tweezers over conventional ones such as optical tweezers, magnetic tweezers, and AFM.

Smaller beads along with smaller conductors and electrodes can be used to construct the biomolecular tweezers with still higher level of parallelism. Recall the magnetic force and dielectrophoretic force given by the following expressions:

$$\vec{F}_M = \frac{2\pi R^3 \mu_0 \chi_{eff}}{3} \nabla |\vec{H}|^2 \quad (7.3)$$

$$\langle \vec{F}_{DEP} \rangle = 2\pi R^3 \varepsilon_r \varepsilon_0 \operatorname{Re}\{f_{CM}(\omega)\} \nabla E_{rms}^2 \quad (7.4)$$

where χ_{eff} and ε_r are the effective magnetic susceptibility and the relative permittivity of the microbead, respectively, and R is the radius of the microbead. The magnetic permeability of vacuum $\mu_0 = 4\pi \times 10^{-7} \text{ H/m}$, and the permittivity of free space $\varepsilon_0 = 8.854 \times 10^{-12} \text{ F/m}$. The balance between magnetic force and negative DEP force yields

$$\frac{\nabla |\vec{H}|^2}{\nabla E_{rms}^2} = \frac{3\varepsilon_0 \varepsilon_r \operatorname{Re}\{f_{CM}(\omega)\}}{\mu_0 \chi} \quad (7.5)$$

With typical values of χ_{eff} , ε_r , and $\operatorname{Re}\{f_{CM}(\omega)\}$, we obtain:

$$\frac{\nabla |\vec{H}|^2}{\nabla E_{rms}^2} \sim \mathcal{O}\left(\frac{\varepsilon_0}{\mu_0}\right) \cong \mathcal{O}(7 \times 10^{-6}) \quad (7.6)$$

This result implies that in the force balance equation the required ∇E_{rms}^2 is about 6 orders of magnitudes larger than $\nabla |\vec{H}|^2$. This is an inherent advantage of our nDEP-MAP devices from the scaling perspective, because DEP force strongly favors miniaturization,

while magnetic force from conducting wires does not favor miniaturization under the constraint of Joule heating (see discussion in chapter 2). From equations (7.3) and (7.4), both magnetic force and DEP force scale with the volume of the beads, i.e., $F_M \sim R^3$ and $F_{DEP} \sim R^3$. At the same time, the scaling law of DEP force is given by $F_{DEP} \sim d^{-3}$ (see discussion in chapter 2). Therefore, the same magnitude of DEP force can be applied to smaller beads. Although the strength of magnetic field must decrease with miniaturization due to Joule heating, equation (7.6) implies that a very weak magnetic field can generate a magnetic force that balances the nDEP force on the same bead from a very strong electric field. Therefore, the size of the beads does not affect the limitation of spatial resolution on our tweezers as significantly as it does to other types such as optical tweezers.

CHAPTER 8

Conclusions and Recommendations for Future Work

8.1 Conclusions

The intent of this work was to explore controlled parallel manipulation of individual magnetic microbeads functionalized with specific molecules for lab-on-a-chip and biomolecular tweezing applications. In particular, the focus of this dissertation was to propose and investigate new manipulation modes of magnetic beads for the advancement of on-chip sample preparation (including mixing, separation, and concentration) and detection schemes, and the development of massively parallel biomolecular tweezers.

Chapter 1 introduced the previous work in these research fields, compared the current manipulation methods, and identified the research topics for this work. Chapter 2 presented the theoretical background and fundamental principles in magnetic and dielectrophoretic manipulations. Chapter 3 described the microfabrication techniques for making NiFe soft magnets and microfluidic channels on a chip, and the surface treatment of the magnetic chip for reducing non-specific adhesion of the microbeads to the chip surface. In chapter 4 we investigated a new platform for electrochemical immunoassay based on the magnetic assembly of the magnetic beads between interdigitated array electrodes on the chip. In chapter 5 we developed a magnetic micromixer for continuous flow in microchannels based on externally induced high-speed orbiting of magnetic beads around NiFe discs on a magnetic chip. In chapter 6 we demonstrated magnetic transport and sorting of microbeads on a magnetic chip with an external rotating magnet that translates. In chapter 7, we integrated conducting wires and electrodes to combine magnetic and dielectrophoretic manipulations for out-of-plane motions of microbeads.

In this work, arrays of soft magnets made of NiFe patterns subjected to an external magnetic field were chosen over conducting wires for magnetic assembly of microbeads on a chip, based on the analysis of scaling of magnetic force with respect to miniaturization. Mathematical model and numerical simulations were used to guide the design of the magnetic chip with optimum layout of the submicron NiFe patterns and appropriate channel height. The theoretical analysis of the efficiency of magnetophoretic (MAP) capturing of Dynabeads MyOne (1 μ m) onto the NiFe soft magnets in an array agreed well with experimental results. Because the size of NiFe magnets was comparable to that of the magnetic beads, assembly of individual beads into an array was realized. The condition for high loading efficiency with uniform assembly of the beads among the soft magnet array was investigated.

MAP assembly was employed to develop a magnetic bead-based immunoassay with electrochemical detection technique. An advanced micro/nanofabrication method was developed to integrate submicron NiFe magnets with similar size of interdigitated array (IDA) electrodes, taking advantage of the high alignment accuracy in multilayer structures offered by JEOL JBX-SF9300 electron beam lithography system. The integrated MAP-IDA device capable of magnetically assembling microbeads between interdigitated array electrodes proved to be a powerful platform for electrochemical immunoassays. Using MyOne beads immobilized with enzyme molecules (β -galactosidase), we found the magnetic assembly method not only provided sample preconcentration in close proximity to the IDA sensing region without blocking the active area of the electrodes, but also allowed each individual bead to maximally contribute to the amperometric signal. The signal from the device as a function of the number density

of the beads, which represents the distribution and level of the preconcentration of enzyme molecules, was shown to be proportional to the number of beads uniformly assembled between identical IDA electrodes. The signal from the smallest number of beads tested, i.e., 900 beads, corresponding to about 50 attomole of β -galactosidase, was significantly larger than the noise level. Therefore, it was far from approaching the limit of detection yet. In addition, the period of signal increase was much extended compared with previous work, allowing a large window for signal acquisition. Furthermore, the rate of the current increase significantly increased with higher number density of microbeads assembled between the IDAs. This result suggests that achieving denser bead distribution among fewer pairs of the IDAs should further improve the performance of the electrochemical immunoassay with enzyme labels.

Next, a new type of active micromixer was realized to locally stir the continuous flow with high-speed orbiting of individual magnetic beads around an array of NiFe discs inside a microchannel. The motion of the beads was induced by an external permanent magnet rotating above the channel. A theoretical basis was developed for determining the effectiveness of the magnetic mixer, by predicating the possible maximum angular velocity of the Dynabeads M-280 (2.8 μ m) the rotating magnetophoresis system could provide. The theoretical prediction suggested surprisingly large angular velocities of the proposed system, i.e., in the order of 1000 rad/sec; and they were shown to agree well with experimental results and were significant for microfluidic mixing purposes. The superior performance of the micromixer was demonstrated by fluorescence intensity profiles across the channel after mixing two streams of flow, one fluorescent and the other non-fluorescent, in the microchannel.

The required length of mixing region strongly depends on the relative speed between the linear speed of the orbiting beads and the speed of the flow. In a microchannel of 120 μm wide and 20 μm tall, we demonstrated that only 200 μm long mixing region is required in our system when the speed of the beads is three times faster than the flow speed. This mixing length is considerably shorter than those reported in literature at flow rates in the same range inside a similar channel. There is still ample room to increase the orbital speed of the beads in our current system for further improvement of mixing efficiency; and one can always generate larger angular speed of the beads with increasing magnetic force from thicker NiFe discs and/or magnetic beads with stronger moment.

The same rotating magnetophoresis system was explored for magnetic transport of the microbeads on a chip. With specially designed magnetic chips and by adding controls to translate the external magnet while it's rotating, we discovered a new mechanism for transporting magnetic beads across an array of NiFe discs on a surface. The working principle was based on the fact that an elliptical orbital trajectory can be induced by varying the field strength on the NiFe discs and the beads within a revolution of the rotation of the external magnet. As the antipodal point of the major axis of the elliptical orbit crosses over the center of the gap between two adjacent NiFe discs, the bead was attracted more by the adjacent disc when it is at the antipodal point. As a result, transport of the bead from one disc to the other took place. The rate of transport was shown to be proportional to the rotational and translational speed of the external magnet. Simultaneous transport of a large number of M-280 (2.8 μm) beads in the order of mm/sec was demonstrated.

We employed this unique transport mechanism for on-chip sorting of magnetic beads based on size, i.e., between 1 μm MyOne and 2.8 μm M-280 beads. Because the magnetic force scales with the volume of the beads, smaller beads experiences significantly smaller magnetic force on the same magnetic chip with the same external field. As a result, the major axis of their elliptical trajectory was much shorter than that of the larger beads orbiting around the same NiFe discs. Hence, the selective transport of larger beads and sorting them from smaller beads was achieved. This on-chip bead sorting technique can facilitate sample separation for *in-situ* detection of multiple analytes, provided different groups of beads are specifically functionalized by immobilization of different biological receptors such as antibodies, proteins, or aptamers. In addition, the transport phenomenon can be employed to increase the loading efficiency and assembly uniformity of the magnetic beads among the NiFe disc array from a flow of bead suspension, removing their dependence on the concentration of the beads in the flow.

Because the magnetic Dyanbeads are composed of mostly polystyrene, which is electrically polarizable, we also explored the dielectrophoretic (DEP) manipulation of the magnetic beads. In particular, out-of-plane motion of the beads was investigated by combining the magnetic attraction and DEP repulsion on the same bead. We chose conducting wires over soft magnets for magnetic field generation in this task because of the easy adjustment of magnetic force. Order-of-magnitude analysis of the integrated device was first conducted. The result suggested some inherent advantages of this integration from both the scaling and the power consumption point-of-views.

A multi-waveform modulator was constructed to generate synchronized square wave for magnetic force and AC signal with on-off sequence for DEP force and to control the switching frequency between the magnetic force and DEP force. Out-of-plane oscillation of M-280 beads in PBS buffer across the channel height (20 μ m) was observed up to 100Hz switching frequency at 50mA and 5V_{pp} 2MHz signals applied to the device. The switching frequency can be increased by using stronger signals for the larger electric and magnetic fields.

Out-of-plane motion of the beads in PBS buffer at high-resolutions was also investigated with both magnetic and electric fields switched on at the same time. The competing magnetic and DEP forces could hold the bead at some equilibrium point in solution. By fine-tuning one of the forces, we were able to tweeze the bead either upward or downward at high spatial resolutions, e.g., in submicron range. The spatial resolution of the MAP-DEP tweezers is not limited by Brownian motion of the beads, regardless of their size, because one can always apply sufficiently large magnetic and DEP force to suppress the Brownian motion and still result in a small net force for high-resolution bead tweezing. In theory, the resolution of our tweezers is only limited by the technology that can be used to apply the control signals. Therefore, the spatial resolution of the proposed tweezers can be very high as current electronic instruments can already offer extremely high precision. In practice, the spatial resolution of the MAP-DEP tweezers will be limited by the technology used to quantify the motion of the beads. The proposed micro/nano tweezers are capable of both spatial and temporal controls in parallel. Therefore, it has the potential to evolve to massively parallel tweezers that can generate

experiment data with statistical significance and high reliability in a single run, leading to high throughput analysis.

Overall, this dissertation presents new capabilities in controlled parallel manipulation of individual magnetic beads for lab-on-a-chip applications (including sample mixing, separation, concentration, and detection) and their potentials in generating novel analytical tools such as parallel biomolecular tweezers and tools for multiplexing many analytes at the point of care.

8.2 Recommendations for Future Work

Additional investigation of the topics and technologies presented in this dissertation will offer enhanced performance and new functionality, as well as broader impact in the field. In this section, we recommend a few future projects as the advanced extensions of the current work.

8.2.1 On-Chip Sorting of Magnetic Beads in Continuous Flow

A new magnetic separation system was presented in chapter 6 that is capable of on-chip separation of magnetic beads into different groups based on size. However, we only demonstrated the separation and sorting of the beads across the microchannel in a stationary fluid. As discussed in both chapters 5 and 6, the magnetic force in our system is strong enough to retain the beads inside the microchannel against a continuous flow while they were orbiting around the individual NiFe discs and translating across the array of discs. Therefore, the separation and sorting of magnetic beads from continuous flow of bead mixture should be feasible, and will lead to enhanced throughput. In addition, the transport of the beads in our system can be guided to defined directions with respect to the flow. Therefore, the idea of selectively transport different groups of beads along or

against the flow seems to be an exciting prospect for continuous bead sorting inside the microchannel. In the mean time, the exact control over forces involved in sorting microbeads with small difference in size is challenging. We believe our off-centered rotating magnetophoresis system can overcome this challenge, because varying bias field between zero and the saturated field strength for different groups of magnetic beads can be conveniently applied to the magnetic chip, leading to a wide range of the magnetic force for selection.

The ability to sorting microbeads of small difference in continuous flow can significantly facilitate the analysis of multiple analytes on a single chip, because different groups of beads can be specifically functionalized to interact and immobilize different analyte onto their surface. An important feature of our separation system is that the beads are always in continuous motion, which exposes the bead surface with a great deal of opportunities to interact with the fluid flow. Such a condition is desired in continuous sample separation in which maximum contact between the analyte and the bio-active coating of the beads is required.

8.2.2 Combining Sample Preparation and Detection on the Same Chip

So far, we have demonstrated effective sample preparation schemes including mixing, separation, and pre-concentration through magnetic circling, transport, and assembly of the microbeads among arrays of NiFe discs. Meanwhile, sensitive detection was demonstrated. However, all these different functions were achieved on different chips as separate lab-on-a-chip modules. A natural next step in advancing our technology is to combine and integrate all these functions on a single chip and realize a true lab-on-a-chip system. During the integration process, it is important to consider seamless

interfaces between different functions and possible synergies from combining the functions. The dominating advantages of our rotating magnetophoresis system for sample preparation and detection include: 1) magnetic field has negligible effect on most chemical and biological substances; 2) magnetic field does not interfere with most of the detection methods including optical and electrochemical means; 3) the sample preparation scheme does not involve in any manipulating elements with heat generation. Hence, we believe our magnetic lab-on-a-chip system will create a powerful alternative to the standard analytical and diagnostic instruments currently used in research labs and clinics.

One application of the proposed integrated system we currently have in mind is the sensing of multiple interleukins on a single chip. Interleukins are a group of cytokines that were first seen to be expressed by white blood cells (leukocytes, hence the term -*leukin*) as a means of communication (*inter-*). The function of the immune system depends in a large part on interleukins, and rare deficiencies of a number of them have been described, all featuring autoimmune diseases or immune deficiency. Therefore, it is important to accurately detect the level of multiple interleukins from the body fluids of the patient. We believe our technology can play a remarkable role in this endeavor.

8.2.3 Development of Massively Parallel Biomolecular Tweezers

In chapter 7, proof-of-concept experiments have been demonstrated for tweezing microbeads in a biologically buffer, i.e., PBS, at high spatial resolutions. The next step is to characterize and calibrate the net force, resulting from the competing magnetic and DEP forces, as a function of the externally adjustable current and voltage input. Currently, the characterization of the MAP-DEP tweezers is limited by the optical

imaging technique that we use to quantify the displacement of the beads. A better technology is needed that is capable of measuring the displacement of the beads in nanometer scale and the corresponding force they experience while being displaced. Then the correlation between the displacement as well as the force and the electrical signal input can be established. Once the nDEP-MAP tweezers is well characterized and calibrated, the device can be used as a new prototype for biomolecular tweezers, as proposed in chapter 7 (section 7.5). Because spatially periodic electric and magnetic fields can be configured by arraying microelectrodes and conducting wires on a chip using microfabrication techniques, the proposed device can be easily scaled up to realize massively parallel biomolecular tweezers on a single chip for high-throughput analysis of biomolecular interactions.

One of the most important questions in cell biology is how cells interact with each other and with extracellular matrix to regulate various signaling processes. Cell growth, differentiation, and adhesion processes are regulated by molecular interactions between cell surface-anchored receptors and their ligands on the counter-surface. Often, the complicated environment with a very wide range of internal forces from actin and myosin affect the interaction kinetics. Our nDEP-MAP tweezers are inherently suitable for measuring force-dependent kinetics of these receptor-ligand interactions. Meanwhile, accurate analysis of the force-dependent kinetics requires a large number of data. While AFM and bio-membrane force probes are very inefficient because they generate kinetics data in a serial manner, often one by one in an experiment, we believe our parallel nDEP-MAP tweezers will revolutionize the existing technologies with high throughput and tight control of experimental conditions. For example, the paradigm adhesion protein

fibronectin (Fn) plays an important role in the mechanical interactions between integrins on the cell surface and the extracellular matrix, due to its unique structural and functional characteristics. Recent studies suggest that the biochemically active portions of Fn – including the central cell binding domain for integrins and growth factor binding domains – are responsible for initiating the overall mechanical interactions between cells and the extracellular matrix. As a result, considerable interest has been focused on the identification of the mechanosensitive peptides of Fn. In general, a large number bacteriophage library (in the order of 10^6 - 10^9) is required to identify the peptide sequence of interest. While no existing technology is available for this task, the massively parallel capability of our tweezers may provide a practical solution for this research. Similarly, our technological platform can be employed for high-throughput analysis of cell adhesion processes, which are regulated by molecular interactions between blood cell surface-anchored receptors and their ligands on endothelial cell surfaces. The association and dissociation rates of individual ligand-receptor pairs are significantly relevant to the immune responses of our body. Comparing with the fast increase of our understanding of cell adhesion processes enabled by the current inefficient technologies, we believe our new, high-throughput technology will accelerate this field at a much faster pace.

APPENDIX A

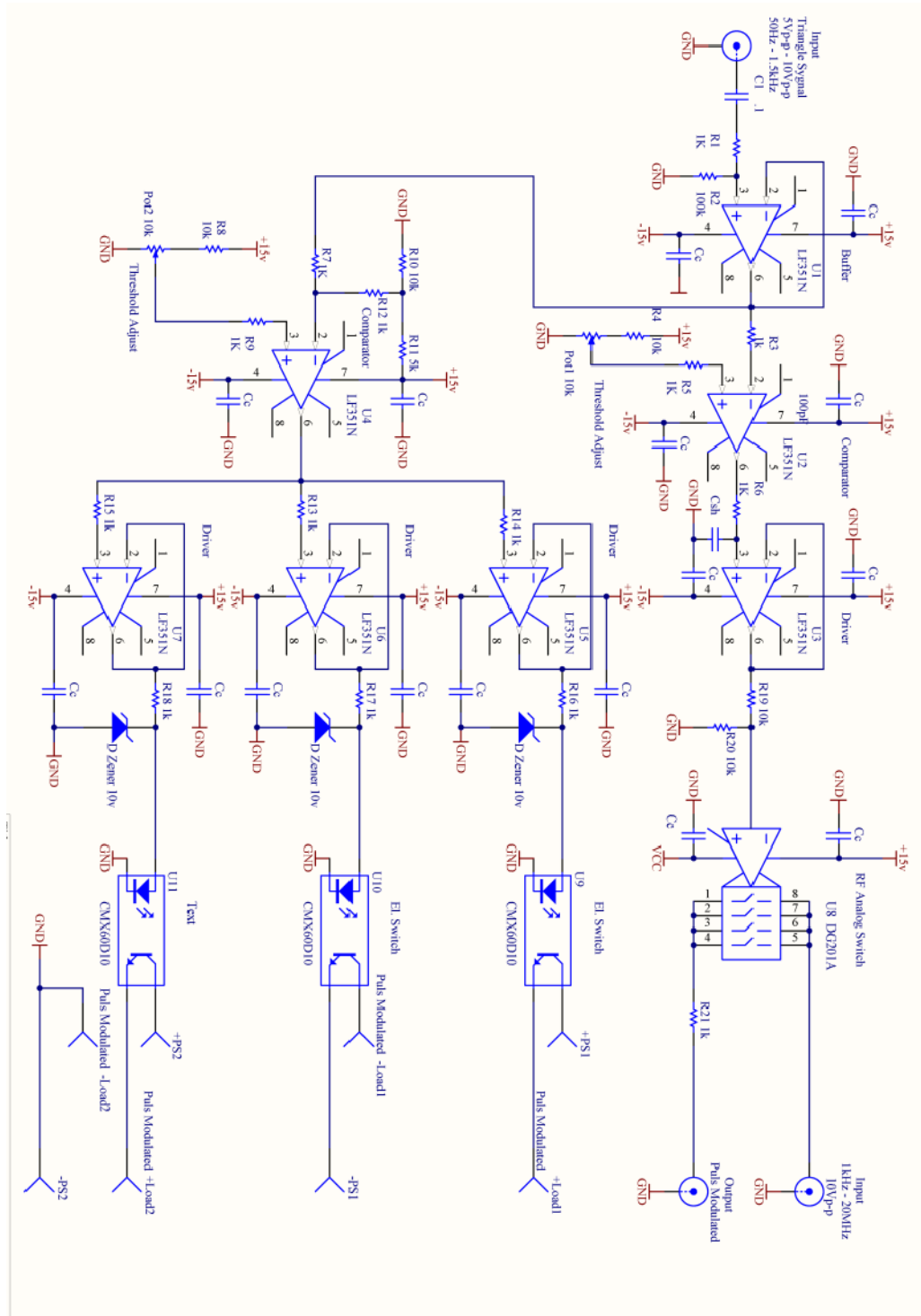
Protocol for Preparing PEGylated Surface

1. Sonicate the magnetic chips inside a vial for 20 minutes in:
 - a). ethanol,
 - b). 0.5 M KOH,
 - c). ethanol.Rinse with DI water after every step, including the last one.
2.
 - a). Measure out 94 mL of isopropanol in a graduated cylinder. Drop in a stir bar.
 - b). Add 6 μ L of glacial acetic acid (17.5 M stock, \sim 1 mM final). Stir for 2 minutes.
 - c). While stirring, add 1 mL of 3-aminopropyltriethoxysilane (i.e. APTES, 1% final concentration).
 - d). Add 5 mL of DI water (5% final concentration), dropwise. Stir for 2 minutes.
3. While preparing the silanization solution, rinse the magnetic chips into isopropanol in a vial. Decant all the solvent out of the vial before the next step.
5. Add the silanization solution to the vial and sonicate for 15 minutes.
6. Decant the silanization solution and wash 2x with isopropanol.
7. Recover the chips from the vial and bake at 90°C for 2hrs. Use a hybridization oven for this step.
9. Recover the chips and place them back into a vial and sonicate 2x20 minutes in ethanol. Do not wash with water before or between the ethanol treatments.
10. Individually remove the chips from the ethanol-filled vial using a pair of forceps and rinse them in DI water by repeated dipping. Rack the pieces and dry them in the 60°C drying oven for an hour.

11. Individually recover the magnetic chips and assemble PDMS microchannels to them.
12. Inject 100 mM HEPES pH 8.0 (i.e. H100-8) into the microchannel to wet the chip surface.
13. Bring the powder stocks of PEG-NHS (MW5000) to room temperature. Weigh out ~10 mg of PEG-NHS and dissolve in H100-8 to make 10 mg/mL solutions.
14. Slowly flow the PEG-NHS solution through the channel and let the reaction between NHS with amine group on the chip surface proceed for 1 hr at room temperature.
15. Flush the channel with DI water, then it's ready to use.
16. Store the device in a moisture environment in a cold room.

APPENDIX B

Block Diagram of Multi-Waveform Modulator



REFERENCES

- [1] G. M. Whitesides, "The origins and the future of microfluidics," *Nature*, vol. 442, no. 7101, pp. 368–373, 2006.
- [2] D. R. Reyes, D. Iossifidis, P. A. Auroux, and A. Manz, "Micro total analysis systems. 1. Introduction, theory, and technology," *Anal. Chem*, vol. 74, no. 12, pp. 2623–2636, 2002.
- [3] H. A. Stone, A. D. Stroock, and A. Ajdari, "Engineering flows in small devices," 2004.
- [4] E. Bassous, H. H. Taub, and L. Kuhn, "Ink jet printing nozzle arrays etched in silicon," *Applied Physics Letters*, vol. 31, p. 135, 1977.
- [5] S. C. Terry, J. H. Jerman, and J. B. Angell, "A gas chromatographic air analyzer fabricated on a silicon wafer," *IEEE Transactions on Electron Devices*, vol. 26, pp. 1880–1885, 1979.
- [6] A. Manz, Y. Miyahara, J. Miura, Y. Watanabe, H. Miyagi, and K. Sato, "Design of an open-tubular column liquid chromatograph using silicon chip technology," *Sensors and actuators B: Chemical*, vol. 1, no. 1, pp. 249–255, 1990.
- [7] A. Manz, N. Graber, and H. M. Widmer, "Miniaturized total chemical analysis systems: a novel concept for chemical sensing," *Sensors and actuators B: Chemical*, vol. 1, no. 1, pp. 244–248, 1990.
- [8] D. C. Duffy, J. C. McDonald, O. J. Schueller, and G. M. Whitesides, "Rapid prototyping of microfluidic systems in poly (dimethylsiloxane)," *Anal. Chem*, vol. 70, no. 23, pp. 4974–4984, 1998.
- [9] R. Schasfoort, S. Schlautmann, J. Hendrikse, and A. van den Berg, "Field-effect flow control for microfabricated fluidic networks," *Science*, vol. 286, no. 5441, p. 942, 1999.
- [10] D. J. Harrison, K. Fluri, K. Seiler, Z. Fan, C. S. Effenhauser, and A. Manz, "Micromachining a miniaturized capillary electrophoresis-based chemical analysis system on a chip," *Science*, vol. 261, no. 5123, pp. 895–897, 1993.
- [11] N. Davis, T. Favero, C. de Hoog, and others, "Quantitative monitoring of gene expression patterns with a complementary DNA microarray," *Science*, vol. 270, p. 467, 1995.
- [12] J. M. Ramsey, S. C. Jacobson, and M. R. Knapp, "Microfabricated chemical measurement systems," *Nature Medicine*, vol. 1, no. 10, pp. 1093–1095, 1995.
- [13] T. M. Squires and S. R. Quake, "Microfluidics: Fluid physics at the nanoliter scale," *Reviews of modern physics*, vol. 77, no. 3, pp. 977–1026, 2005.
- [14] T. Thorsen, S. J. Maerkl, and S. R. Quake, "Microfluidic large-scale integration," *Science*, vol. 298, no. 5593, p. 580, 2002.
- [15] S. Haeberle and R. Zengerle, "Microfluidic platforms for lab-on-a-chip applications," *Lab on a Chip*, vol. 7, no. 9, pp. 1094–1110, 2007.
- [16] D. R. Walt, "Chemistry: miniature analytical methods for medical diagnostics," *Science*, vol. 308, no. 5719, p. 217, 2005.
- [17] P. S. Dittrich and A. Manz, "Lab-on-a-chip: microfluidics in drug discovery," *Nature Reviews Drug Discovery*, vol. 5, no. 3, pp. 210–218, 2006.
- [18] C. Situma, M. Hashimoto, and S. A. Soper, "Merging microfluidics with

- microarray-based bioassays,” *Biomolecular engineering*, vol. 23, no. 5, pp. 213–231, 2006.
- [19] K. Sato, M. Yamanaka, H. Takahashi, M. Tokeshi, H. Kimura, and T. Kitamori, “Microchip-based immunoassay system with branching multichannels for simultaneous determination of interferon- γ ,” *Electrophoresis*, vol. 23, no. 5, pp. 734–739, 2002.
- [20] E. P. Kartalov, J. F. Zhong, A. Scherer, S. R. Quake, C. R. Taylor, and W. F. Anderson, “High-throughput multi-antigen microfluidic fluorescence immunoassays,” *Biotechniques*, vol. 40, no. 1, p. 85, 2006.
- [21] D. A. Vignali, “Multiplexed particle-based flow cytometric assays,” *Journal of immunological methods*, vol. 243, no. 1, pp. 243–255, 2000.
- [22] T. Yang, S. Jung, H. Mao, and P. S. Cremer, “Fabrication of phospholipid bilayer-coated microchannels for on-chip immunoassays,” *Anal. Chem*, vol. 73, no. 2, pp. 165–169, 2001.
- [23] A. Dodge, K. Fluri, E. Verpoorte, and N. F. de Rooij, “Electrokinetically driven microfluidic chips with surface-modified chambers for heterogeneous immunoassays,” *Anal. Chem*, vol. 73, no. 14, pp. 3400–3409, 2001.
- [24] E. Verpoorte, “FocusBeads and chips: new recipes for analysis,” *Lab on a Chip*, vol. 3, no. 4, pp. 60–68, 2003.
- [25] H. Kawaguchi, “Functional polymer microspheres,” *Progress in polymer science*, vol. 25, no. 8, pp. 1171–1210, 2000.
- [26] N. Pamme, “Magnetism and microfluidics,” *Lab on a Chip*, vol. 6, no. 1, pp. 24–38, 2006.
- [27] K. Sato et al., “Integration of an immunosorbent assay system: analysis of secretory human immunoglobulin A on polystyrene beads in a microchip,” *Anal. Chem*, vol. 72, no. 6, pp. 1144–1147, 2000.
- [28] M. B. Meza, “Bead-based HTS applications in drug discovery,” *Drug Discovery Today*, vol. 5, pp. 38–41, 2000.
- [29] G. H. Seong and R. M. Crooks, “Efficient mixing and reactions within microfluidic channels using microbead-supported catalysts,” *J. Am. Chem. Soc*, vol. 124, no. 45, pp. 13360–13361, 2002.
- [30] D. C. Pregibon, M. Toner, and P. S. Doyle, “Multifunctional encoded particles for high-throughput biomolecule analysis,” *Science*, vol. 315, no. 5817, p. 1393, 2007.
- [31] S. Derveaux et al., “Synergism between particle-based multiplexing and microfluidics technologies may bring diagnostics closer to the patient,” *Analytical and Bioanalytical Chemistry*, vol. 391, no. 7, pp. 2453–2467, 2008.
- [32] B. B. Yellen and G. Friedman, “Programmable assembly of heterogeneous colloidal particle arrays,” *Advanced Materials*, vol. 16, no. 2, pp. 111–115, 2004.
- [33] V. Sivagnanam, B. Song, C. Vandevyver, J. C. Bünzli, and M. A. Gijs, “Selective Breast Cancer Cell Capture, Culture, and Immunocytochemical Analysis Using Self-Assembled Magnetic Bead Patterns in a Microfluidic Chip,” *Langmuir*, vol. 26, no. 9, pp. 6091–6096, 2010.
- [34] B. M. Taff and J. Voldman, “A scalable addressable positive-dielectrophoretic cell-sorting array,” *Anal. Chem*, vol. 77, no. 24, pp. 7976–7983, 2005.
- [35] P. Y. Chiou, A. T. Ohta, and M. C. Wu, “Massively parallel manipulation of single cells and microparticles using optical images,” *Nature*, vol. 436, no. 7049, pp.

- 370–372, 2005.
- [36] C. Simonnet and A. Groisman, “High-throughput and high-resolution flow cytometry in molded microfluidic devices,” *Anal. Chem.*, vol. 78, no. 16, pp. 5653–5663, 2006.
- [37] L. Riegger et al., “Read-out concepts for multiplexed bead-based fluorescence immunoassays on centrifugal microfluidic platforms,” *Sensors and Actuators A: Physical*, vol. 126, no. 2, pp. 455–462, 2006.
- [38] J. Seo and L. P. Lee, “Disposable integrated microfluidics with self-aligned planar microlenses,” *Sensors and Actuators B: Chemical*, vol. 99, no. 2, pp. 615–622, 2004.
- [39] A. Ashkin, “Acceleration and trapping of particles by radiation pressure,” *Physical Review Letters*, vol. 24, no. 4, pp. 156–159, 1970.
- [40] A. Ashkin and J. M. Dziedzic, “Optical trapping and manipulation of single living cells using infra-red laser beams,” *Berichte der Bunsengesellschaft für physikalische Chemie*, vol. 93, no. 3, pp. 254–260, 1989.
- [41] R. M. Simmons, J. T. Finer, S. Chu, and J. A. Spudich, “Quantitative measurements of force and displacement using an optical trap,” *Biophysical Journal*, vol. 70, no. 4, pp. 1813–1822, 1996.
- [42] J. Voldman, “Electrical forces for microscale cell manipulation,” *Biomedical Engineering*, vol. 8, no. 1, p. 425, 2006.
- [43] T. Grahl and H. Märkl, “Killing of microorganisms by pulsed electric fields,” *Applied microbiology and biotechnology*, vol. 45, no. 1, pp. 148–157, 1996.
- [44] R. K. Adair, “Constraints on biological effects of weak extremely-low-frequency electromagnetic fields,” *Physical Review A*, vol. 43, no. 2, pp. 1039–1048, 1991.
- [45] M. Groschl, “Ultrasonic separation of suspended particles-Part I: Fundamentals,” *Acta Acustica united with Acustica*, vol. 84, no. 3, pp. 432–447, 1998.
- [46] S. M. Woodside, J. M. Piret, M. Gröschl, E. Benes, and B. D. Bowen, “Acoustic force distribution in resonators for ultrasonic particle separation,” *AIChE Journal*, vol. 44, no. 9, pp. 1976–1984, 1998.
- [47] M. Evander et al., “Noninvasive acoustic cell trapping in a microfluidic perfusion system for online bioassays,” *Anal. Chem.*, vol. 79, no. 7, pp. 2984–2991, 2007.
- [48] F. Petersson, L. Åberg, A. M. Swärd-Nilsson, and T. Laurell, “Free flow acoustophoresis: microfluidic-based mode of particle and cell separation,” *Anal. Chem.*, vol. 79, no. 14, pp. 5117–5123, 2007.
- [49] J. M. Guldbakke and J. Hesselbach, “Development of bearings and a damper based on magnetically controllable fluids,” *Journal of Physics: Condensed Matter*, vol. 18, p. S2959, 2006.
- [50] J. D. Carlson, W. Matthis, and J. R. Toscano, “Smart prosthetics based on magnetorheological fluids,” in *Proceedings of SPIE*, vol. 4332, p. 308, 2001.
- [51] R. E. Rosensweig, Y. Hirota, S. Tsuda, and K. Raj, “Study of audio speakers containing ferrofluid,” *Journal of Physics: Condensed Matter*, vol. 20, p. 204147, 2008.
- [52] N. Xia et al., “Combined microfluidic-micromagnetic separation of living cells in continuous flow,” *Biomedical Microdevices*, vol. 8, no. 4, pp. 299–308, 2006.
- [53] B. I. Haukanes and C. Kvam, “Application of magnetic beads in bioassays,” *Nature Biotechnology*, vol. 11, no. 1, pp. 60–63, 1993.

- [54] R. De Palma et al., "Magnetic bead sensing platform for the detection of proteins," *Anal. Chem*, vol. 79, no. 22, pp. 8669–8677, 2007.
- [55] Q. A. Pankhurst, J. Connolly, S. K. Jones, and J. Dobson, "Applications of magnetic nanoparticles in biomedicine," *Journal of Physics D: Applied Physics*, vol. 36, p. R167, 2003.
- [56] D. L. S. Company, *Centrifugal separation: a science and an art*. The De Laval Separator Company, 1978.
- [57] R. F. Probstein, *Physicochemical hydrodynamics: an introduction*. John Wiley and Sons, 1994.
- [58] M. A. Hayes, N. A. Polson, A. N. Phayre, and A. A. Garcia, "Flow-based microimmunoassay," *Anal. Chem*, vol. 73, no. 24, pp. 5896–5902, 2001.
- [59] G. Jiang and D. J. Harrison, "mRNA isolation in a microfluidic device for eventual integration of cDNA library construction," *The Analyst*, vol. 125, no. 12, pp. 2176–2179, 2000.
- [60] V. I. Furdul and D. J. Harrison, "Immunomagnetic T cell capture from blood for PCR analysis using microfluidic systems," *Lab on a Chip*, vol. 4, no. 6, pp. 614–618, 2004.
- [61] Y. Jiang, M. E. Miller, M. E. Hansen, M. N. Myers, and P. S. Williams, "Fractionation and size analysis of magnetic particles using FFF and SPLITT technologies," *Journal of Magnetism and Magnetic Materials*, vol. 194, no. 1, pp. 53–61, 1999.
- [62] N. Pekas, M. Granger, M. Tondra, A. Popple, and M. D. Porter, "Magnetic particle diverter in an integrated microfluidic format," *Journal of Magnetism and Magnetic Materials*, vol. 293, no. 1, pp. 584–588, 2005.
- [63] N. Pamme, J. C. Eijkel, and A. Manz, "On-chip free-flow magnetophoresis: Separation and detection of mixtures of magnetic particles in continuous flow," *Journal of magnetism and magnetic materials*, vol. 307, no. 2, pp. 237–244, 2006.
- [64] J. C. Giddings, F. J. Yang, and M. N. Myers, "Flow-field-flow fractionation: a versatile new separation method.," *Science (New York, NY)*, vol. 193, no. 4259, p. 1244, 1976.
- [65] J. W. Choi et al., "An integrated microfluidic biochemical detection system for protein analysis with magnetic bead-based sampling capabilities," *Lab on a Chip*, vol. 2, no. 1, pp. 27–30, 2002.
- [66] K. Y. Lien, J. L. Lin, C. Y. Liu, H. Y. Lei, and G. B. Lee, "Purification and enrichment of virus samples utilizing magnetic beads on a microfluidic system," *Lab on a Chip*, vol. 7, no. 7, pp. 868–875, 2007.
- [67] T. Deng, M. Prentiss, and G. M. Whitesides, "Fabrication of magnetic microfiltration systems using soft lithography," *Applied physics letters*, vol. 80, p. 461, 2002.
- [68] S. S. Guo, C. C. Zuo, W. H. Huang, C. Peroz, and Y. Chen, "Response of superparamagnetic beads in microfluidic devices with integrated magnetic microcolumns," *Microelectronic engineering*, vol. 83, no. 4, pp. 1655–1659, 2006.
- [69] T. Deng, G. M. Whitesides, M. Radhakrishnan, G. Zabow, and M. Prentiss, "Manipulation of magnetic microbeads in suspension using micromagnetic systems fabricated with soft lithography," *Applied Physics Letters*, vol. 78, p. 1775, 2001.

- [70] Q. Ramadan, C. Yu, V. Samper, and D. P. Poenar, "Microcoils for transport of magnetic beads," *Applied Physics Letters*, vol. 88, p. 032501, 2006.
- [71] C. S. Lee, H. Lee, and R. M. Westervelt, "Microelectromagnets for the control of magnetic nanoparticles," *Applied Physics Letters*, vol. 79, p. 3308, 2001.
- [72] B. B. Yellen, R. M. Erb, H. S. Son, R. Hewlin, H. Shang, and G. U. Lee, "Traveling wave magnetophoresis for high resolution chip based separations," *Lab on a Chip*, vol. 7, no. 12, pp. 1681–1688, 2007.
- [73] R. S. Conroy, G. Zabow, J. Moreland, and A. P. Koretsky, "Controlled transport of magnetic particles using soft magnetic patterns," *Applied Physics Letters*, vol. 93, p. 203901, 2008.
- [74] K. Gunnarsson et al., "Programmable motion and separation of single magnetic particles on patterned magnetic surfaces," *Advanced Materials*, vol. 17, no. 14, pp. 1730–1734, 2005.
- [75] A. Rida and M. A. M. Gijs, "Dynamics of magnetically retained supraparticle structures in a liquid flow," *Applied physics letters*, vol. 85, p. 4986, 2004.
- [76] A. Rida and M. A. M. Gijs, "Manipulation of self-assembled structures of magnetic beads for microfluidic mixing and assaying," *Anal. Chem*, vol. 76, no. 21, pp. 6239–6246, 2004.
- [77] R. Wirix-Speetjens, W. Fyen, K. Xu, J. De Boeck, and G. Borghs, "A force study of on-chip magnetic particle transport based on tapered conductors," *IEEE transactions on magnetics*, vol. 41, no. 10, 2005.
- [78] L. E. Helseth, T. M. Fischer, and T. H. Johansen, "Domain wall tip for manipulation of magnetic particles," *Physical review letters*, vol. 91, no. 20, p. 208302, 2003.
- [79] E. Mirowski, J. Moreland, S. E. Russek, and M. J. Donahue, "Integrated microfluidic isolation platform for magnetic particle manipulation in biological systems," *Applied Physics Letters*, vol. 84, p. 1786, 2004.
- [80] A. Ashkin, J. M. Dziedzic, J. E. Bjorkholm, and S. Chu, "Observation of a single-beam gradient force optical trap for dielectric particles," *Optical angular momentum*, p. 196, 2003.
- [81] M. Carrion-Vazquez et al., "Mechanical and chemical unfolding of a single protein: a comparison," *Proceedings of the National Academy of Sciences of the United States of America*, vol. 96, no. 7, p. 3694, 1999.
- [82] C. Gosse and V. Croquette, "Magnetic tweezers: micromanipulation and force measurement at the molecular level," *Biophysical Journal*, vol. 82, no. 6, pp. 3314–3329, 2002.
- [83] C. H. Chiou and G. B. Lee, "A micromachined DNA manipulation platform for the stretching and rotation of a single DNA molecule," *Journal of Micromechanics and Microengineering*, vol. 15, p. 109, 2005.
- [84] U. Häfeli, W. Schütt, J. Teller, and M. Zborowski, *Scientific and clinical applications of magnetic carriers*. Plenum Press New York, 1997.
- [85] M. A. Gijs, "Magnetic bead handling on-chip: new opportunities for analytical applications," *Microfluidics and Nanofluidics*, vol. 1, no. 1, pp. 22–40, 2004.
- [86] I. Braslavsky, B. Hebert, E. Kartalov, and S. R. Quake, "Sequence information can be obtained from single DNA molecules," *Proceedings of the National Academy of Sciences of the United States of America*, vol. 100, no. 7, p. 3960, 2003.

- [87] M. L. Sin, Y. Shimabukuro, and P. K. Wong, "Hybrid electrokinetics for separation, mixing, and concentration of colloidal particles," *Nanotechnology*, vol. 20, p. 165701, 2009.
- [88] P. Yager et al., "Microfluidic diagnostic technologies for global public health," *Nature*, vol. 442, no. 7101, pp. 412–418, 2006.
- [89] C. H. Mastrangelo, M. A. Burns, and D. T. Burke, "Microfabricated devices for genetic diagnostics," *Proceedings of the IEEE*, vol. 86, no. 8, pp. 1769–1787, 1998.
- [90] R. P. Hertzberg and A. J. Pope, "High-throughput screening: new technology for the 21st century," *Current Opinion in Chemical Biology*, vol. 4, no. 4, pp. 445–451, 2000.
- [91] V. Srinivasan, V. K. Pamula, and R. B. Fair, "An integrated digital microfluidic lab-on-a-chip for clinical diagnostics on human physiological fluids," *Lab on a Chip*, vol. 4, no. 4, pp. 310–315, 2004.
- [92] A. J. Tüdös, G. A. Besselink, and R. B. Schasfoort, "Trends in miniaturized total analysis systems for point-of-care testing in clinical chemistry," *Lab on a Chip*, vol. 1, no. 2, pp. 83–95, 2001.
- [93] H. A. Pohl, *Dielectrophoresis: the behavior of neutral matter in nonuniform electric fields*. Cambridge University Press Cambridge, 1978.
- [94] H. Morgan and N. G. Green, "AC electrokinetics: colloids and nanoparticles," 2003.
- [95] R. Pethig, "Dielectrophoresis: using inhomogeneous AC electrical fields to separate and manipulate cells," *Critical reviews in biotechnology*, vol. 16, no. 4, pp. 331–348, 1996.
- [96] F. F. Becker, X. B. Wang, Y. Huang, R. Pethig, J. Vykoukal, and P. R. Gascoyne, "Separation of human breast cancer cells from blood by differential dielectric affinity," *Proceedings of the National Academy of Sciences of the United States of America*, vol. 92, no. 3, p. 860, 1995.
- [97] J. D. Yantzi, J. T. W. Yeow, and S. S. Abdallah, "Multiphase electrodes for microbead control applications: Integration of DEP and electrokinetics for bio-particle positioning," *Biosensors and Bioelectronics*, vol. 22, no. 11, pp. 2539–2545, 2007.
- [98] S. Golan, D. Elata, and U. Dinnar, "Hybrid dielectrophoresis devices that employ electrically floating electrodes," *Sensors and Actuators A: Physical*, vol. 142, no. 1, pp. 138–146, 2008.
- [99] C. F. Chou and F. Zenhausern, "Electrodeless dielectrophoresis for micro total analysis systems," *IEEE Engineering in medicine and biology magazine*, vol. 22, no. 6, pp. 62–67, 2003.
- [100] E. B. Cummings and A. K. Singh, "Dielectrophoresis in microchips containing arrays of insulating posts: theoretical and experimental results," *Anal. Chem*, vol. 75, no. 18, pp. 4724–4731, 2003.
- [101] S. Ozuna-Chacón, B. H. Lapizco-Encinas, M. Rito-Palomares, S. O. Martínez-Chapa, and C. Reyes-Betanzo, "Performance characterization of an insulator-based dielectrophoretic microdevice," *Electrophoresis*, vol. 29, no. 15, pp. 3115–3122, 2008.
- [102] I. Doh and Y. H. Cho, "A continuous cell separation chip using hydrodynamic

- dielectrophoresis (DEP) process,” *Sensors and Actuators A: Physical*, vol. 121, no. 1, pp. 59–65, 2005.
- [103] M. D. Vahey and J. Voldman, “An equilibrium method for continuous-flow cell sorting using dielectrophoresis,” *Anal. Chem.*, vol. 80, no. 9, pp. 3135–3143, 2008.
- [104] M. Dür, J. Kentsch, T. Müller, T. Schnelle, and M. Stelzle, “Microdevices for manipulation and accumulation of micro-and nanoparticles by dielectrophoresis,” *Electrophoresis*, vol. 24, no. 4, pp. 722–731, 2003.
- [105] J. Park, B. Kim, S. K. Choi, S. Hong, S. H. Lee, and K. I. Lee, “An efficient cell separation system using 3D-asymmetric microelectrodes,” *Lab on a Chip*, vol. 5, no. 11, pp. 1264–1270, 2005.
- [106] L. Wang, L. A. Flanagan, N. L. Jeon, E. Monuki, and A. P. Lee, “Dielectrophoresis switching with vertical sidewall electrodes for microfluidic flow cytometry,” *Lab on a Chip*, vol. 7, no. 9, pp. 1114–1120, 2007.
- [107] Y. Li, C. Dalton, H. J. Crabtree, G. Nilsson, and K. V. Kaler, “Continuous dielectrophoretic cell separation microfluidic device,” *Lab on a Chip*, vol. 7, no. 2, pp. 239–248, 2007.
- [108] N. G. Green, A. Ramos, and H. Morgan, “AC electrokinetics: a survey of sub-micrometre particle dynamics,” *Journal of Physics D: Applied Physics*, vol. 33, p. 632, 2000.
- [109] G. O. Parikesit et al., “Size-dependent trajectories of DNA macromolecules due to insulative dielectrophoresis in submicrometer-deep fluidic channels,” *Biomicrofluidics*, vol. 2, p. 024103, 2008.
- [110] C. H. Kua, Y. C. Lam, I. Rodriguez, C. Yang, and K. Youcef-Toumi, “Dynamic cell fractionation and transportation using moving dielectrophoresis,” *Anal. Chem.*, vol. 79, no. 18, pp. 6975–6987, 2007.
- [111] J. Suehiro and R. Pethig, “The dielectrophoretic movement and positioning of a biological cell using a three-dimensional grid electrode system,” *Journal of Physics D: Applied Physics*, vol. 31, p. 3298, 1998.
- [112] A. B. Fuchs et al., “Electronic sorting and recovery of single live cells from microlitre sized samples,” *Lab on a Chip*, vol. 6, no. 1, pp. 121–126, 2006.
- [113] A. Rosenthal and J. Voldman, “Dielectrophoretic traps for single-particle patterning,” *Biophysical Journal*, vol. 88, no. 3, pp. 2193–2205, 2005.
- [114] N. Manaresi et al., “A CMOS chip for individual cell manipulation and detection,” *IEEE Journal of Solid-State Circuits*, vol. 38, no. 12, p. 2297, 2003.
- [115] J. Voldman, M. Toner, M. L. Gray, and M. A. Schmidt, “Design and analysis of extruded quadrupolar dielectrophoretic traps,” *Journal of electrostatics*, vol. 57, no. 1, pp. 69–90, 2003.
- [116] M. S. Jaeger, K. Uhlig, T. Schnelle, and T. Mueller, “Contact-free single-cell cultivation by negative dielectrophoresis,” *Journal of Physics D: Applied Physics*, vol. 41, p. 175502, 2008.
- [117] Y. Kang and D. Li, “Electrokinetic motion of particles and cells in microchannels,” *Microfluidics and Nanofluidics*, vol. 6, no. 4, pp. 431–460, 2009.
- [118] E. G. Cen, C. Dalton, Y. Li, S. Adamia, L. M. Pilarski, and K. V. Kaler, “A combined dielectrophoresis, traveling wave dielectrophoresis and electrorotation microchip for the manipulation and characterization of human malignant cells,” *Journal of microbiological methods*, vol. 58, no. 3, pp. 387–401, 2004.

- [119] A. Ramos, H. Morgan, N. G. Green, A. Gonzalez, and A. Castellanos, "Pumping of liquids with traveling-wave electroosmosis," *Journal of applied physics*, vol. 97, p. 084906, 2005.
- [120] L. E. Johansson et al., "A magnetic microchip for controlled transport of attomole levels of proteins," *Lab on a Chip*, vol. 10, no. 5, pp. 654–661, 2010.
- [121] A. D. Stroock, S. K. Dertinger, A. Ajdari, I. Mezic, H. A. Stone, and G. M. Whitesides, "Chaotic mixer for microchannels," *Science*, vol. 295, no. 5555, p. 647, 2002.
- [122] H. Suzuki, C. M. Ho, and N. Kasagi, "A chaotic mixer for magnetic bead-based micro cell sorter," *Microelectromechanical Systems, Journal of*, vol. 13, no. 5, pp. 779–790, 2004.
- [123] J. Ugelstad, A. Rembaum, J. T. Kemshead, K. Nustad, S. Funderud, and R. Schmid, "Preparation and biomedical application of mono disperse polymer particles," *Microspheres and Drug Therapy: Pharmaceutical, Immunological and Medical Aspects. Amsterdam, the Netherlands*, pp. 365–382, 1984.
- [124] R. J. Derks, A. Dietzel, R. Wimberger-Friedl, and M. W. Prins, "Magnetic bead manipulation in a sub-microliter fluid volume applicable for biosensing," *Microfluidics and Nanofluidics*, vol. 3, no. 2, pp. 141–149, 2007.
- [125] G. Fonnum, C. Johansson, A. Molteberg, S. Morup, and E. Aksnes, "Characterisation of Dynabeads® by magnetization measurements and Mössbauer spectroscopy," *Journal of Magnetism and Magnetic Materials*, vol. 293, no. 1, pp. 41–47, 2005.
- [126] M. Zborowski, L. Sun, L. R. Moore, P. Stephen Williams, and J. J. Chalmers, "Continuous cell separation using novel magnetic quadrupole flow sorter," *Journal of Magnetism and Magnetic Materials*, vol. 194, no. 1, pp. 224–230, 1999.
- [127] B. Yellen, G. Friedman, and A. Feinerman, "Analysis of interactions for magnetic particles assembling on magnetic templates," *Journal of Applied Physics*, vol. 91, p. 8552, 2002.
- [128] G. Friedman and B. Yellen, "Magnetic separation, manipulation and assembly of solid phase in fluids," *Current Opinion in Colloid & Interface Science*, vol. 10, no. 3, pp. 158–166, 2005.
- [129] A. Castellanos, A. Ramos, A. Gonzalez, N. G. Green, and H. Morgan, "Electrohydrodynamics and dielectrophoresis in microsystems: scaling laws," *Journal of Physics D: Applied Physics*, vol. 36, p. 2584, 2003.
- [130] J. Edminister, *Theory and problems of electromagnetics*. McGraw-Hill, 1979.
- [131] J. W. Judy and N. Myung, "Magnetic materials for MEMS," in *MRS Workshop on MEMS Materials, San Francisco, California, (April 5-6, 2002)*, pp. 23–26.
- [132] B. Löchel and A. Maciossek, "Electrodeposited magnetic alloys for surface micromachining," *Journal of the Electrochemical Society*, vol. 143, p. 3343, 1996.
- [133] Y. Xia and G. M. Whitesides, "Softlithographie," *Angewandte Chemie*, vol. 110, no. 5, pp. 568–594, 1998.
- [134] V. C. Yang and T. T. Ngo, *Biosensors and their Applications*. Kluwer Academic/Plenum Publishers, 2000.
- [135] O. Niwa, Y. Xu, H. B. Halsall, and W. R. Heineman, "Small-volume voltammetric detection of 4-aminophenol with interdigitated array electrodes and its application to electrochemical enzyme immunoassay," *Analytical chemistry*, vol. 65, no. 11,

- pp. 1559–1563, 1993.
- [136] S. S. Iqbal, M. W. Mayo, J. G. Bruno, B. V. Bronk, C. A. Batt, and J. P. Chambers, “A review of molecular recognition technologies for detection of biological threat agents,” *Biosensors and Bioelectronics*, vol. 15, no. 11, pp. 549–578, 2000.
- [137] U. Wollenberger, M. Paeschke, and R. Hintsche, “Interdigitated array microelectrodes for the determination of enzyme activities,” *The Analyst*, vol. 119, no. 6, pp. 1245–1249, 1994.
- [138] O. Niwa, M. Morita, and H. Tabei, “Highly sensitive and selective voltammetric detection of dopamine with vertically separated interdigitated array electrodes,” *Electroanalysis*, vol. 3, no. 3, pp. 163–168, 1991.
- [139] A. J. Bard, J. A. Crayston, G. P. Kittlesen, T. Varco Shea, and M. S. Wrighton, “Digital simulation of the measured electrochemical response of reversible redox couples at microelectrode arrays: consequences arising from closely spaced ultramicroelectrodes,” *Analytical Chemistry*, vol. 58, no. 11, pp. 2321–2331, 1986.
- [140] M. Paeschke, U. Wollenberger, C. Köhler, T. Lisec, U. Schnakenberg, and R. Hintsche, “Properties of interdigital electrode arrays with different geometries,” *Analytica Chimica Acta*, vol. 305, no. 1, pp. 126–136, 1995.
- [141] Y. Degani and A. Heller, “Electrical communication between redox centers of glucose oxidase and electrodes via electrostatically and covalently bound redox polymers,” *Journal of the American Chemical Society*, vol. 111, no. 6, pp. 2357–2358, 1989.
- [142] X. Luo, J. Xu, J. Barford, I. Hsing, and others, “Magnetic particle based electrochemical sensing platform for PCR amplicon detection,” *Electrochemistry Communications*, vol. 12, no. 4, pp. 531–534, 2010.
- [143] E. P. Furlani, *Permanent magnet and electromechanical devices: materials, analysis, and applications*. Academic Press, 2001.
- [144] N. Kaneki, Y. Xu, A. Kumari, H. B. Halsall, W. R. Heineman, and P. T. Kissinger, “Electrochemical enzyme immunoassay using sequential saturation technique in a 20- μ l capillary: digoxin as a model analyte,” *Analytica Chimica Acta*, vol. 287, no. 3, pp. 253–258, Mar. 1994.
- [145] S. K. Kim, P. J. Hesketh, C. Li, J. H. Thomas, H. B. Halsall, and W. R. Heineman, “Fabrication of comb interdigitated electrodes array (IDA) for a microbead-based electrochemical assay system,” *Biosensors and Bioelectronics*, vol. 20, no. 4, pp. 887–894, 2004.
- [146] V. Hessel, H. Löwe, and F. Schönfeld, “Micromixers—a review on passive and active mixing principles,” *Chemical Engineering Science*, vol. 60, no. 8, pp. 2479–2501, 2005.
- [147] F. G. Bessoth, A. J. deMello, and A. Manz, “Microstructure for efficient continuous flow mixing,” *Analytical communications*, vol. 36, no. 6, pp. 213–215, 1999.
- [148] P. Hinsmann, J. Frank, P. Svasek, M. Harasek, and B. Lendl, “Design, simulation and application of a new micromixing device for time resolved infrared spectroscopy of chemical reactions in solution,” *Lab on a Chip*, vol. 1, no. 1, pp. 16–21, 2001.
- [149] T. J. Johnson, D. Ross, and L. E. Locascio, “Rapid microfluidic mixing,” *Anal. Chem*, vol. 74, no. 1, pp. 45–51, 2002.

- [150] N. T. Nguyen and Z. Wu, "Micromixers—a review," *Journal of Micromechanics and Microengineering*, vol. 15, p. R1, 2005.
- [151] R. H. Liu, R. Lenigk, and P. Grodzinski, "Acoustic micromixer for enhancement of DNA biochip systems," *Journal of Microlithography, Microfabrication, and Microsystems*, vol. 2, p. 178, 2003.
- [152] W. K. Tseng, L. Lin Jr, W. C. Sung, S. H. Chen, and G. B. Lee, "Active micromixers using surface acoustic waves on Y-cut 128° LiNbO₃," *Journal of Micromechanics and Microengineering*, vol. 16, p. 539, 2006.
- [153] V. Vivek and E. S. Kim, "Novel acoustic-wave micromixer," in *Micro Electro Mechanical Systems, 2000. MEMS 2000. The Thirteenth Annual International Conference on*, pp. 668–673, 2002.
- [154] Y. K. Lee, J. Deval, P. Tabeling, and C. M. Ho, "Chaotic mixing in electrokinetically and pressure driven micro flows," in *Micro Electro Mechanical Systems, 2001. MEMS 2001. The 14th IEEE International Conference on*, pp. 483–486, 2002.
- [155] J. Deval, P. Tabeling, and C. M. Ho, "A dielectrophoretic chaotic mixer," in *Micro Electro Mechanical Systems, 2002. The Fifteenth IEEE International Conference on*, pp. 36–39, 2002.
- [156] A. J. Goldman, R. G. Cox, and H. Brenner, "Slow viscous motion of a sphere parallel to a plane wall—I Motion through a quiescent fluid* 1," *Chemical Engineering Science*, vol. 22, no. 4, pp. 637–651, 1967.
- [157] M. E. O'Neill and K. Stewartson, "On the slow motion of a sphere parallel to a nearby plane wall," *Journal of Fluid Mechanics*, vol. 27, no. 04, pp. 705–724, 1967.
- [158] M. E. O'Neill, "A slow motion of viscous liquid caused by a slowly moving solid sphere," *Mathematika*, vol. 11, no. 01, pp. 67–74, 1964.
- [159] G. H. Seong and R. M. Crooks, "Efficient mixing and reactions within microfluidic channels using microbead-supported catalysts," *J. Am. Chem. Soc.*, vol. 124, no. 45, pp. 13360–13361, 2002.
- [160] X. J. A. Janssen, A. J. Schellekens, K. Van Ommering, L. J. Van Ijzendoorn, and M. W. J. Prins, "Controlled torque on superparamagnetic beads for functional biosensors," *Biosensors and Bioelectronics*, vol. 24, no. 7, pp. 1937–1941, 2009.
- [161] R. Wirix-Speetjens and J. de Boeck, "On-chip magnetic particle transport by alternating magnetic field gradients," *Magnetics, IEEE Transactions on*, vol. 40, no. 4, pp. 1944–1946, 2004.
- [162] P. S. Doyle, J. Bibette, A. Bancaud, and J. L. Viovy, "Self-assembled magnetic matrices for DNA separation chips," *Science*, vol. 295, no. 5563, p. 2237, 2002.
- [163] A. Blake, *Handbook of mechanics, materials, and structures*. Wiley-Interscience, 1985.
- [164] T. JONES, G. BLISS, and F. C. Colorado State Univ., "Bubble dielectrophoresis," *Journal of Applied Physics*, vol. 48, pp. 1412–1417, 1977.
- [165] C. Derec, C. Wilhelm, J. Servais, and J. C. Bacri, "Local control of magnetic objects in microfluidic channels," *Microfluidics and Nanofluidics*, vol. 8, no. 1, pp. 123–130, 2010.